Western University
Scholarship@Western

2008

On neurovascular regulation of primary visual cortex: neuronal activity and hemodynamics

Zheng Wang
Western University

Follow this and additional works at: https://ir.lib.uwo.ca/digitizedtheses

On neurovascular regulation of primary visual cortex: neuronal activity and hemodynamics

(Spine Title: On neurovascular regulation of primary visual cortex)

(Thesis Format: Integrated Article)

by

Zheng Wang

Graduate Program in Medical Biophysics

Submitted in partial
fulfillment of the requirements
for the degree of Doctor of
Philosophy

School of Graduate and Postdoctoral Studies
The University of Western Ontario
London, Ontario

Abstract

Modern brain functional imaging techniques like functional magnetic resonance imaging (fMRI) mostly infer alterations of neuronal activities by mapping local changes in cerebral blood flow (CBF) or metabolism. The understanding of the relationship between neuronal activity and the hemodynamic responses, the so called neurovascular coupling, is critical for the interpretation of signals like the blood-oxygenation-level-dependent (BOLD) effect. The neurovascular regulation is modeled by a linear transform model in the fMRI experiments, which allows making an inverse inference from BOLD to neuron. Some recent reports suggest that the BOLD response is a nonlinear function in the time domain. Because changes in CBF underlie the BOLD effect, a separate assessment of the CBF response would be useful to gain more insight into this complicated relationship. This thesis concerns aspects of making quantitative CBF measurements in vivo.

Avoiding the profound consequences caused by anesthesia, we addressed the relationship between CBF and neural activity by recording variations of the neural and induced hemodynamic signals in the primary visual cortex (V1) in monkeys. The animals were trained to view a standard stimulus pattern whose duration could be varied. The extracellular field potentials and CBF responses were acquired by a microelectrode and laser Doppler probe through a recording chamber. Through a stable deconvolution analysis, a rapid biphasic and a slower monophasic hemodynamic response functions (HRFs) were identified to associate the transient and sustained components of the power spectral density of the local field potential (LFP) with the CBF responses, respectively.

Beyond the implications for fMRI analysis and BOLD biophysical models, our findings suggest that there exist two distinctly tuned CBF regulatory mechanisms in primate cortex. One appears to support the high energy demands typical of the transient neuronal response and the other the more modest demands of a sustained neuronal response.

The laser Doppler probe measures signals at one position on the cortex. To spatially resolve distinct hemodynamic responses evoked by complex neuronal activation requires an in-vivo flow imaging technique that can directly visualize changes of blood flow with sufficient spatial and temporal resolution. To this end, an optical imaging technique – laser speckle contrast imaging (LSCI) with superior spatiotemporal (at micrometer and millisecond level) was developed to gain in-depth knowledge of spatial regulation of local CBF responses. In order to optimize this method, a number of basic assumptions in LSCI were re-examined by theoretical analysis and an important strategy was proposed for in vivo applications. The detailed distribution of CBF responses to physiological manipulation was imaged with tens of micron spatial resolution in the exposed cortex and quantitatively compared to the laser Doppler measurements. Our results demonstrate that optimization of LSCI can achieve high specificity to assess cerebral microcirculation, and LSCI is a promising, quantitative, minimally invasive method to achieve in vivo high-resolution visualization of blood flow in exposed biological tissue.

Co-Authorship

The following thesis contains material from previously published manuscripts co-authored by Zheng Wang, Sarah Hughes, Sudath Dayasundara and Ravi S. Menon. All the experimental work and the hardware systems presented in this thesis was conducted and developed by Zheng Wang, with the assistance of Sarah Hughes in animal preparation and Sudath Dayasundara at an earlier phase of system setup. The experimental design and data analysis were conceptualized and developed by Zheng Wang and further refined by his supervisor. The original version of the manuscripts that appear in Chapter 2 and Chapter 3, were initially written by Zheng Wang and edited in conjunction with his supervisor. The release of copyrighted material contained in this thesis is presented in Appendix A.

Acknowledgements

Let there be light

Genesis 1:3

Table of Contents

List of Figures

List of Appendices

List of Abbreviations and Symbols

Symbol	Definition
σ^2	variance of the phase process
Δx	spatial location at x axis
Δy	spatial location at y axis
I_T	integrated intensity of speckle
$\bar{I}$	mean intensity of speckle
Γ_1	autocorrelation of the electric field
μ_A	the normalized autocovariance function of speckle
M	a shaping constant
T	time
$\overline{I_T}$	the first moment of speckle
$\sigma^2_{I_T}$	variance of speckle
r_o^2	coherent radius
v	scalar velocity
g	anisotropy factor
θ	deflection angle of scattered photon
$erf(x)$	standard error function
τ_c	correlation time
$P(v)$	Maxwellian velocity distribution
$p(I)$	probability density function of speckle intensity
$\Gamma(M)$	a gamma function
R^2	coefficient of determination
τ	duration of visual stimulus
$g(t)$	gamma-variate function
λ	relative contribution of negative component
$CBF_\tau(t)$	CBF responses to different duration of visual stimuli
$HRF_{TR}(t)$	HRF corresponding to transient neural activity
$HRF_{SR}(t)$	HRF corresponding to sustained neural activity
$HRF_{IR}(t)$	HRF corresponding to initial response of neural activity
$u_{TR\tau}(t)$	transient response of neural activity
$u_{SR\tau}(t)$	sustained response of neural activity
BOLD	blood oxygenation level dependent
C	speckle contrast
CBF	cerebral blood flow
CCD	charge coupled device
CO_2	carbon dioxide
dHb	deoxygenated hemoglobin
DoF	degree of freedom
EFP	extracellular field potential

fMRI	functional magnetic resonance imaging
GLM	general linear model
HbO	oxygenated hemoglobin
HRF	hemodynamic impulse response function
IR	initial response
LASCA	laser speckle contrast analysis
LDF	laser Doppler flowmetry
LFP	local field potential
LGN	lateral geniculate nucleus
LSCI	laser speckle contrast imaging
LMA	Levenberg-Marquardt algorithm
LSF	laser speckle flowmetry
M	magnocellular
MRI	magnetic resonance imaging
MUA	multi-unit activity
NO	nitric oxide
NA	neural activity
O_2	oxygen
OIS	optical imaging of intrinsic signals
P	parvocellular
$PaCO_2$	partial pressures of carbon dioxide
PDF	probability density function
PET	positron-emission tomography
PSD	power spectral density
PSTH	peri-stimulus time histogram
RBC	red blood cell
RF	receptive field
RGC	retinal ganglion cell
ROI	region-of-interest
SR	sustained response
SD	spectral density
SNR	signal to noise ratio
TR	transient response
V1	primary visual cortex

Chapter 1   Introduction

This thesis mainly focuses on the intimate relationship between neural activity and the induced hemodynamic response in the brain, which forms the basis for many modern functional neuroimaging techniques including functional magnetic resonance imaging (fMRI). This chapter will provide the background and rationale for the measurements that have been done in this thesis and fMRI signals like blood oxygen level dependent (BOLD) contrast. The biophysical basis of BOLD fMRI contrast and its underlying physiological contributions are first presented to explain our motivation for doing these studies. Neural activity is discussed in the context of the extracellular recordings. The linear transform model is introduced to model the neurovascular regulation. Then the two kinds of optical techniques that are used in this study to measure cerebral blood flow (CBF) are introduced. In order to generalize the conclusions of this thesis to other brain regions or species, some relevant specifics of the primary visual cortex of primates are presented. Finally this chapter concludes with a brief overview of each chapter of the thesis.

1.1 Functional Magnetic Resonance Imaging

1.1.1 BOLD contrast

The brain consumes 20% of the resting energy produced in the body in spite of being only 2% of the total body mass, making it one of the most metabolically active of all organs in the body [1]. The utilization of oxygen provides the energy required for its intense physiochemical activity. Since the O_2 concentration in brain tissue is extremely low compared with the metabolic demand for O_2, the brain requires continuous replenishment of its O_2 by the circulation [1]. Therefore, an adequate supply of blood flow to the brain is of critical importance for normal brain functioning.

When one or more functional units of brain increase their neural activities, the local blood supply will increase in a temporally and spatially coordinated manner. More than a century ago, Roy and Sherrington postulated that "the brain possesses an intrinsic mechanism by which its vascular supply can be varied locally in correspondence with local variations of functional activity", and they also proposed that "chemical products of cerebral metabolism" produced in the course of neuronal activation could provide the mechanism to couple activity with increased blood flow [2]. This kind of neurovascular/neurometabolic coupling provides the principal basis for functional neuroimaging techniques such as positron emission tomography (PET) and fMRI.

BOLD fMRI is a non-invasive imaging technique that measures changes in the local magnetic field properties caused by the amount of deoxygenated hemoglobin (dHb) in brain tissue [3; 4]. When the neural activity in a region of the brain increases above its 'resting' value, there is an immediate increase in local oxygen consumption. Oxygen in the blood is carried almost exclusively by hemoglobin molecules in the red blood cells

(RBCs). The elevated energy demand for brain function initiates the transition of the oxygenated hemoglobin (HbO) to the paramagnetic dHb in RBCs. The dHb enhances the magnetic field inhomogeneity and influences the intensity of certain types of MR images. It was firstly described by Ogawa and his colleagues in rodent brain studies and subsequently applied to generate functional images in the human brain [5-9]. These pioneering reports triggered an overwhelming flood of fMRI publications that have appeared in scientific journals ever since. During the past sixteen years, this technique has become the predominant method for exploring the function and dysfunction of the human brain due to its non-invasiveness and higher spatiotemporal resolution compared to other techniques used in human research. Its accessibility is linked to the widespread availability of magnetic scanners both in the clinical and research environments.

Apart from its successful adoption within such a short history, there still remain some elusive issues as to the fundamental mechanism that couples evoked neuronal activities with the hemodynamic responses [10-16]. The following diagram (Fig. 1.1) can give some idea of the complexity of the physiological response of this MR signal. One emerging theory of BOLD signal posits that an increase in neuronal activity results in an initial increase in oxygen consumption owing to increased metabolic demand [17-20]; this changes the concentration of HbO and dHb in the nearby vasculature, which is the early phase of the BOLD signal [21]. The increased neuronal activity also triggers a large increase in local blood flow, which overcompensates for the initial oxygen demand and thus increases the local vascular concentration of HbO. This is the second phase of BOLD signals [22-24]. Although BOLD fMRI is primarily sensitive to changes in dHb [25], the competing effects of CBF, cerebral blood volume (CBV), and oxygen consumption after external
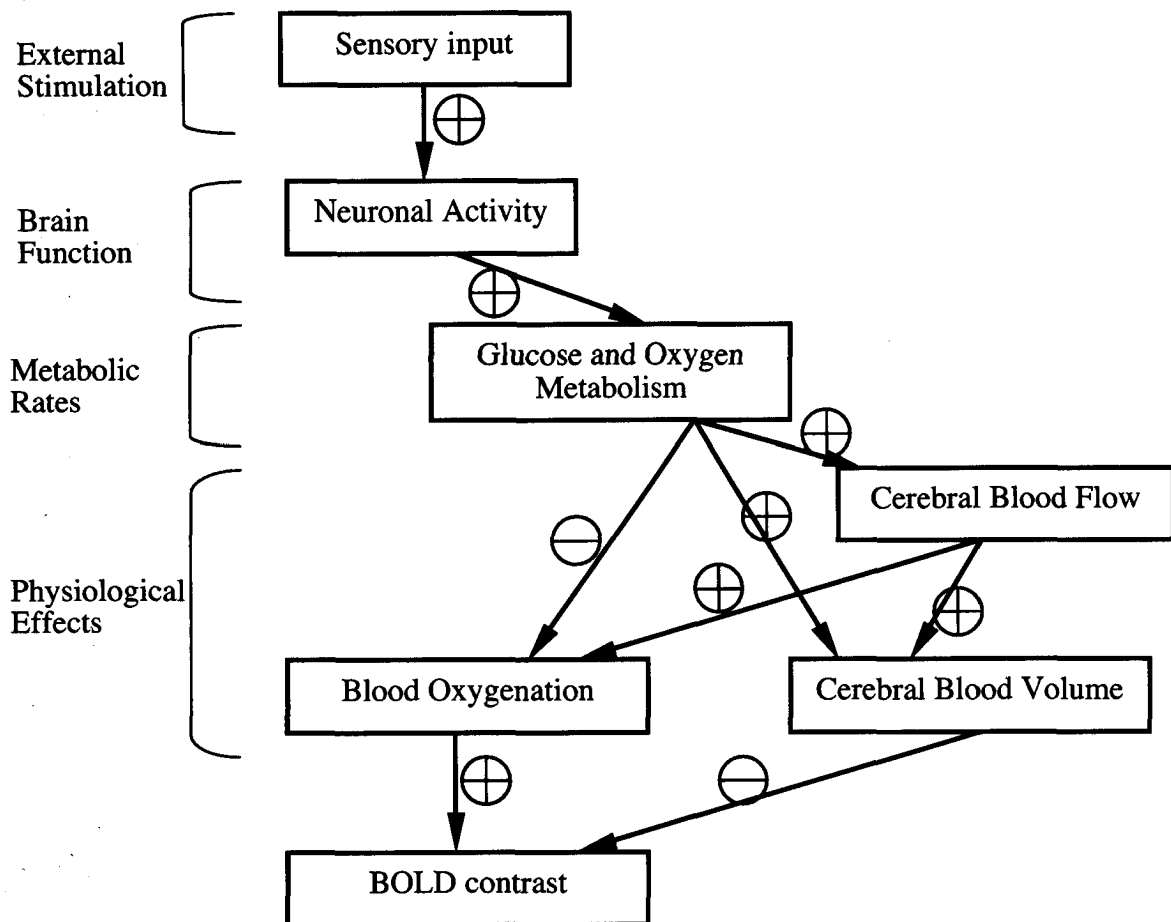
Figure 1.1 Positive/negative signs indicate positive and negative relationships between the parameters.

stimulation involve the dHb changes. Caution should be exercised in the interpretation of fMRI results, particularly when one attempts to use this hemodynamic-based signal as a standard approach to make sophisticated scientific inquiry in the brain. Thus a detailed study of the chain of neurophysiological events in the brain could provide more insight into the underlying mechanisms that convert neural activity to BOLD signals. The thesis focuses on two key aspects of this cascade of events: neuronal activity and corresponding blood flow. The following sections will progress from a discussion of neural activity to neurovascular regulation, CBF measurement, and specifics of our working animal model.

1.1.2 Neural activity

Ever since the development of microelectrodes about 80 years ago, action potentials (also known as a nerve impulse or spike) of well-isolated neurons have been used as a gold standard measurement to understand the neural basis of behavior [26]. A neuronal action potential is initiated when the membrane potential is depolarized sufficiently strongly, i.e., when the voltage of the cell's interior relative to the cell's exterior is raised above a threshold. The utility of the study of single-unit action potential was strengthened by its suitability for studying the first steps of afferent information processing in sensory physiology [15]. But recordings of single unit activity provide information about only a single cell or a small number of cells within a region of nervous tissue, with an inherent bias towards recording from larger cells (e.g., pyramidal cells in cerebral cortex) [27]. The pyramidal neurons provide most of the excitatory output of the neocortex and act as an intracortical excitatory input through their axonal collaterals as well [28]. This kind of recording can not reveal any information about the sub-threshold integrative processes that are essential for producing spikes within these nervous structures.

According to the theoretical estimations of the cortical gray matter energy budget, the major energy-demanding cortical process in primates is attributable to the postsynaptic activity (~74% of the total energy used on signaling) while action potentials are thought to consume only about 10% of the signaling energy [29]. Increases in CBF have been correlated with local energy use during activity [13]. In view of this, a better insight into the intimate interaction between neuronal activity and blood flow could be attained by concurrently recording both sub-threshold membrane potentials and spiking activities [30; 31].

Usually a microelectrode with a relatively large tip (low impedance, i.e., <100 kΩ) is placed in the extracellular space to record the extracellular field potential (EFP) at its tip that reflects current flow in the extracellular medium. The impedance, shape and configuration of the electrode tip will empirically determine what types of signals are measured. For example, spikes from single units will usually not be discriminable if the electrode tip impedance is sufficiently low and its contact point is a bit farther from the spike-generating sources [27]. The range of neural signals that an electrode is sensitive to can be described by the radius of a sphere of tissue around the electrode tip, which is largely determined by the impedance of the exposed tip. If electrodes with a tip impedance 40 ~ 120 kΩ (tip size ~ 100 μm) are used, the largest component of this current typically is that generated by the action potentials from hundreds of nearby neurons (that are assumed to reflect average or summed spiking activities in the vicinity of the electrode tip, 140 ~ 300 μm) [28]. Another signal source is the field potentials that resulted from the synchronous flow of current into a parallel set of dendrites

perpendicular to the pial surface (most likely from within 2000 ~ 3000 μm of the electrode tip) [32; 33].

Thus this EFP voltage can be subdivided into two parts by its frequency features (low pass < 250 Hz for local field potential, LFP, and high-pass 800 ~ 5000 Hz for multiple-unit activity, MUA). The neurons in the primary visual cortex are connected with each other and elaborately branched dendritic trees on one end (which serve as input regions to the cell) and axonal trees on the other (which project the cell output to other neurons), which forms an ideal open-field structure [15]. Thus, the LFP signals will reflect an aggregate measure of local input (intrinsic afferent) activity and local intracortical processing mediated by the sub-threshold signals of interneurons [28; 34]. In contrast, MUA generally reflects many action potentials with widely varying amplitudes carried by the principal (output) neurons of a given brain area [15].

It has been argued that BOLD measurements were more correlated to the LFP other than MUA, and this has given rise to the concept that BOLD signal represents an input more than output signal of a given brain region [32]. This conclusion has motivated an intense research on the distinction between LFP and spiking activities [33-36]. Because MUA and LFP usually are highly correlated, the results from different studies are difficult to interpret, often conflicting with each other as to the relative contributions of one over the other [36-40]. For example, Rees and his colleagues compared human fMRI results with single unit recordings in monkeys and suggested a proportional relationship between BOLD and the average neuronal spiking rate [39], which is further supported by other groups [40]. Another study on human subjects reported that both LFP and MUA could be used to predict BOLD responses within a linear model framework [36]. Some elegant

studies managed to dissociate MUA and LFP with the use of neuromodulator [35] or some specific visual stimulus patterns [33] or microstimulation [34] in order to obtain more results implicating the importance of the LFP. One of the latest report suggests that the above notion is not so straightforward and may oversimplify the real situation [41]. The authors suggested that the coupling between MUA, LFP and BOLD could possibly change over time, and this time-varying relation could depend on not only the stimulus properties but also the spontaneous activity. Understanding LFP, its relationship with the spiking activity and the BOLD signal is still an important topic of research [42].

Nevertheless, it's important to point out that previous attempts to address the issue of CBF coupling to neural activity mostly relied on the central assumption of the linear transform model that relates neuronal activities to BOLD responses [12; 32; 36]. Any uncertainty on this key relationship will further complicate the issue and several studies have shown a nonlinear relationship under certain circumstances [32; 43-48]. Therefore, emphasis of the current study was placed on analysis of linear modeling between neural activity (especially LFP) and hemodynamic responses, which has very important implications on data analysis and interpretation in the functional imaging field. This linear transform model and its physiological justification will be discussed in next section.

1.1.3 Linear transform model

As discussed above, BOLD fMRI signal reflects a complex interplay between changes in blood flow, blood volume and oxygenation that are coupled to the underlying neural activity in response to an input stimulus. The measured BOLD signal by MR scanners usually reflects an averaged physiological response integrated over a spatial

extent of several millimeters (i.e., spatial integration). One has to make an inference from the BOLD measurements to the brain activity, which is the well known hemodynamic inverse problem [49]. The central assumption guiding inference is that the fMRI signal is approximately proportional to a measure of local neural activity. By adopting a linear convolution model for brain responses in fMRI, we are implicitly assuming some underlying dynamic system that converts neuronal responses into observed hemodynamic responses. This has been referred to as the linear transform model of the BOLD fMRI signal, which has been an indispensable component in almost all fMRI studies (also called model-driven study) [12]. There is a mountain of literature based on the model-driven analysis and only two representative reviews are listed here [12; 50]. One major benefit of this linear approximation is that the analysis and interpretation of fMRI data are greatly simplified.

Here is an example given to demonstrate how this linear model works in many routine fMRI studies. One can design a certain cognitive task in an ON/OFF manner such as 20 s task and 20 s rest, also called the block design. Since the BOLD response is small and contaminated with various physiological and physical noises, we have to repeat the same task consecutively to get reliable results. Because the brain function is temporally modulated by the cognitive task, the temporal correlation between the experimental paradigm and the recorded fMRI data can be used to identify the activated spatial locations in the brain. But BOLD signals, unlike the neuronal responses, rise with some delay after the onset of the task due to the sluggish hemodynamic response (seen in Fig. 1.2). Thus, a hemodynamic impulse response function (HRF) with an assumed shape

(e.g., a Gamma function in Fig. 1.2) is inserted to convolve the designed paradigm to account approximately for this lag. The presumed shape of the HRF will predominantly
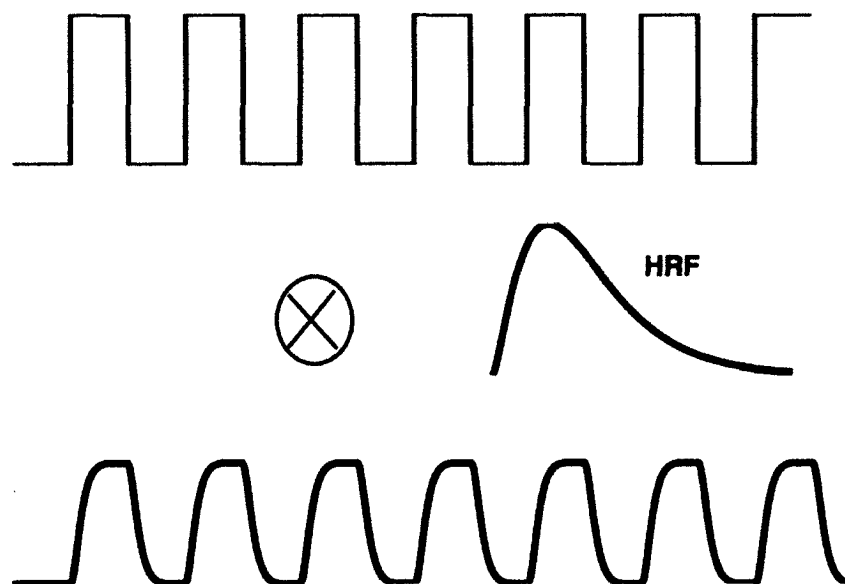
Figure 1.2 The top row represents the OFF/ON task paradigm. The middle row plot a typical HRF function with an assumed Gamma function shape, which convolves with the above box-car design to approximate the temporal response of the anticipated BOLD activation. ⊗ stands for the convolution operation. The resulting curve (the bottom row) is used to seek the temporal correlation between the task and the voxels in the MRI images.

decide which voxels of the images statistically stand out to represent the activated spots in the brain.

One major limitation of this block-design paradigm is that many trials of the same task type have to be presented in immediate succession. In 1996, Buckner and his colleagues successfully adopted a single-trial procedure that was originally used in

studies of event-related potentials (ERPs) into the fMRI experiments [51]. The single-trial (or event-related) design not only allows the paradigms that are mixed with different task types, but also greatly reduces the time period of the data acquisition (e.g., shorten the duration of each trial). Some studies further demonstrated the single trials within in one session could be spaced as little as 2 second apart (decreasing the intertrial time) [52]. Until now, this design strategy has been extensively used in the cognitive neuroscience field. But the fact is that the hemodynamic response to individual trials is temporally extended. If the neighboring trials are designed too close, their hemodynamic responses may overlap and complicate the data analysis. Apparently such overlap can readily be estimated and removed if the hemodyanmic response conforms to the properties of the time-invariant linear model. However, any compromise on this linear assumption would certainly bias the functional mapping of brain structures.

During the past few years, our understanding of the biophysical and physiological mechanisms that underpin the HRF has grown considerably [53-55]. Some reports suggested that the BOLD response is a nonlinear function of the stimulus duration [43; 45-48]. Because changes in CBF are only one component of the BOLD effect, we do not necessarily expect to find the same nonlinearity in the CBF response as in the BOLD response. BOLD nonlinearities might arise in the steps between stimulus and CBF or in the transition from flow response to BOLD response. Thus separate assessment of CBF response would help gain more insights into the complicated relationship with the BOLD effects. So far the linearity of the perfusion (CBF) response has not been as well studied as the BOLD response [56-58].

From a physiological perspective, the HRF is a simplified mathematical description of the link between the neuronal and hemodynamic responses, also called neurovascular coupling [12; 13; 59]. Local increases in blood flow result from the rapid dilation of arterioles and capillaries of a restricted area in response to an episode of increased neuronal activity [59]. This type of coordinated operation arises from the complex interactions between a network of multiple cell types including neurons, astrocytes, oligodendrocytes, microglia, and the microvascular endothelial cells comprising the cerebral vasculature. Such a function unit consisting of the neuron and its associated glia and endothelial cells, has been termed the "neurovascular unit" [13]. The cells in this unit interact with each other through a physical association in the same microenvironment in a positive and negative feedback manner.

Neuronal processes are tightly associated with cerebral blood vessels. The established view is that smooth muscle cells and pericytes convert the chemical signals that originate from endothelial cells, neurons and astrocytes into variations in vascular diameter thus changing the blood flow [31]. For example, the relatively large pial arteries in the cortical vascular system are innervated by nerves from autonomic and sensory ganglia, which can signal the arteries to constrict or dilate [60]. The pial arteries branch into smaller arteries and arterioles that enter the brain tissue, called the penetrating arterioles. These arterioles are almost entirely surrounded by the astrocytic endfeet that contact with the contractile elements of blood vessels like smooth muscle cells in arterioles [61; 62]. The astrocytic endfeet occupy a larger surface area of the microvasculature than the neural processes, which indicates astrocyte plays a significant role in the local control of microcirculation during neuronal activity [29]. The involvement of astrocytes in neurovascular coupling has

an important impact on the traditional view of neuron-vessel interaction and the interpretation of functional imaging signals [63]. The cellular mechanisms of linking regulation of blood flow and energy metabolism is still under investigation.

Based on the results currently available to us, the neurovascular unit in nature is well suited to control the timing and spatial distribution of the increase in blood flow evoked by neural activity. Only this type of closely-coupled mediation can possibly permit us to reliably infer brain function by detecting hemodynamic signals [31]. It actually is the physiological justification of the linear transform model.

1.1.4 Measurement of cerebral blood flow

The development of modern CBF measurement methodologies derived from Kety and Schmidt's seminal work in 1945 [64]. These two pioneers used an ingenious approach, based on the Fick's principle, which involved inhalation of a diffusible inert gas tracer (N_2O) to achieve accurate quantitation of global CBF levels. Since that time, there has been an explosion of techniques to study the cerebral circulation across diversified spatial or temporal scales: heat clearance technique [65], hydrogen clearance [66], angiography [67], ultrasonography [68], non-/diffusible tracer-based measurements of cerebral flow [64], laser Doppler [69], laser speckle [70], near infrared spectroscopy [71], computerized tomography (CT) [72;73], PET [74], MRI [75], and it is certain that newer techniques will be developed in the future.

More recently, much attention has been directed toward studies on the mechanisms of cerebral perfusion regulation at the local, cellular, and molecular levels. Evaluations of "local" factors can involve use of both in vivo and in vitro (brain slices) techniques. Although optical measurements of the blood flow offer superior resolution, the in vivo

applications of these methods are largely bounded by the opacity of the skull. To circumvent this problem, the cranial window technique is applied which was firstly invented in the 19th century to examine the morphology of pial vessels. Basically it opens a transparent window on the brain and maintains an environment for the pial vessels as close to the normal one as possible with regard to intracranial pressure, composition of the surrounding fluid and prevailing gas tensions [76]. This method gives us an excellent platform to directly observe and study the cerebral microcirculation in both acute and chronic experiments. The implantation of a cranial window on a large animal like a primate requires removal of the dura mater for better detection of signal from deeper part of the cortex since the illumination light can penetrate further [76; 77]. The use of a long-term cranial window technique is not trivial, but was key to the measurements performed in Chapter 2.

Exploiting this cranial window technique, two optically based flow-detection techniques – laser Doppler and laser speckle were employed in this study to measure and image variations of blood flow in the upper layers of the exposed cortex.

1.1.5 Laser Doppler flowmetry

The Doppler effect was first discovered by Christian Doppler in 1842. It describes the frequency change a wave as perceived by an observer moving relative to the source of the waves. The red blood cells (RBCs) move at low velocities, on the order of millimeters per second in the microcirculation, giving rise to minute frequency shifts compared to the frequency of the incident light. It is difficult to detect these frequency changes if the incident light itself contains different frequencies. As a consequence, it is critical that the light source is highly monochromatic (or temporally coherent). Since the first

commercially available lasers in 1960, the Doppler technique has found practical applications in many fields.

The earliest use of laser Doppler to measure blood flow was demonstrated in retina and later in the vascularized tissue in the 1970s [69; 78]. Now LDF has become a well-established medical tool of assessing changes in blood flow both in research and clinical fields. In the present study, LDF was used to assess the visually evoked hemodynamic responses in the exposed primary visual cortex of awake macaques. It was also used as a validation standard for the development of the laser speckle contrast imaging (LSCI) technique described in this thesis (Chapter 3). More comprehensive theoretical derivation details of the LDF principles can be found in Bonner and Nossal's classic paper [79].

There are two major practical considerations related to the implementation of this technique on awake preparations. One is to deal with the motion artifacts. Generally a laser doppler perfusion monitor requires two multimode fiber-optic probes, one to deliver the laser light into the perfused tissue and the other to couple the back-scattered photons to a photodetector. One inherent limitation of this configuration is the influence of the movement between the transmitting and receiving probes, which becomes a serious barrier for the application on behaving animal subjects. This problem can be mitigated by using an integrated probe where light delivery and detection are on the same fiber. It is a single-point measurement method, which records the perfusion integrated from a sampling volume with high temporal resolution (<100 ms).

The second consideration is to appropriately estimate the sensitive volume of the in vivo measurement. In the above single-probe setup, the measurement depth and sampling volume mainly depends on the wavelength of the laser beam (830 nm used in our study),

optical properties (scattering and absorption coefficients) of the tissue, and structure and density of blood vessels. It is known that longer wavelength of light provides deeper LDF recordings than a shorter one. An in vitro study suggests that green light (543 nm) has a smaller penetration depth (0.33 mm) into tissue than infrared light (800 nm) which penetrates to 4.3 mm [80]. But it has been recognized that large variations exist the in vivo optical properties of the biological tissue in various parts of the body and in different species [81]. Furthermore, for cortical CBF measurements, dependency on the density of vessels is pronounced since the dura mater and aforementioned large vessels on the cortical surface can dramatically reduce the penetration depth of laser signals. This situation can be improved effectively by removing the dura mater and placing the LDF probe in such a way as to avoid being on the top of those large superficial vessels. Obviously the above estimation depends heavily on the tissue sample and flow patterns. So far only the upper limits of the LDF measurement depth are roughly estimated in many applications since the LDF signal cannot accurately resolved with respect to cortical depth. A large body of evidence from both Monte-Carlo theoretical simulation and in vivo animal experiments indicate that a more reliable value of the sample volume of LDF approximately is 1.0~1.5 mm^3 in the cortical tissue [80-88]. In fact, this measurement depth is comparable to the sensitive volume of the electrical signals measured by the microelectrode in this thesis study.

1.1.6 Laser speckle

Laser speckle is a random interference effect that only came into prominence with the invention of the laser with its high coherence. In fact laser speckle is mathematically equivalent to laser Doppler [89; 90], and the speckle phenomena have analogues in other

fields as well, such as radar detection and ultrasound imaging. When laser light falls on an optical rough surface such as paper or unpolished metal or the wall of the laboratory, one observes a high-contrast, fine-scale salt-and-peppery pattern called "granularity" caused by random phases interferences [91]. This is termed "speckle". Speckle is also observed when laser light is transmitted through stationary diffusers or when light is scattered from particle suspensions (like erythrocytes in the perfused tissue).

Whenever there is any relative movement of the surface and the detector, the speckle pattern appears to scintillate since the speckle intensity is constantly changing due to phase addition or subtraction [92]. Displacement of particles alters the coherence among individual wavelets (scattered light) and will change the speckle pattern over time [93]. Such randomly fluctuating speckle patterns have been studied extensively as "time-varying speckle" or "dynamic speckle" (for a comprehensive review, see [94]). Dynamic speckle is frequently observed when a biological sample is illuminated by a laser light. The temporal and spatial intensity variations of this pattern contain the information about the motion of the scattering particles. The dynamics of blood flow can be obtained by analyzing the spatio-temporal characteristics of the intensity fluctuations. This approach can provide two-dimensional maps of CBF with very high spatial and temporal resolution by imaging the speckle pattern with a CCD camera. This is the main idea behind the LSCI technique, which was first proposed by Briers and his colleague to make non-contact images of the skin blood flow in 1981 [95].

When taking a picture by the CCD detector with a certain exposure time (typically 10 ~ 50 ms), the recorded speckle pattern appears blurred in those areas where there is motion of scatterers. By quantifying the blurring within the speckle images, one can map

the spatial distribution of relative changes in blood flow. Note that laser speckle is a random phenomenon that can only be described statistically [96]. The LSCI method uses the statistics of integrated intensity variations of speckles to quantify it (only their mean and standard deviation). Goodman has coined an extremely important parameter - speckle contrast - as the ratio of the standard deviation to the mean intensity [97]. The speckle contrast is found to have an inverse relationship with the motion of scattering particles. This provides a key link between the measured values in the experiments and the blood flow information we wish to know. More strict derivation and mathematical details of LSCI technique will be presented in Chapter 3 of the thesis.

Although LSCI technique was initially proposed more than 27 years ago [95], it remained virtually unused. Recent work done by a research group in Harvard Medical School [98; 99], has reignited the interest of the researchers to take a second look at this "old" technique. From the rapidly-rising trend shown by the number of published papers relevant to LSCI during the past 5 years, it is certain that more attentions will be drawn to exploit the advantages of this technique [100].

1.2 Primary visual cortex of primates

Although the changes underlying the generation of intracellularly recorded action potentials are well understood now, there is still some uncertainty about the field potentials that can be recorded in the vicinity of active neurons by an extracellular microelectrode, mostly due to the complications related to the geometry or architecture of neuronal structures. Hence a thorough knowledge of the anatomical organization of the structure to be studied is critical for the correct interpretation of the EFPs. Similarly, the

molecular mechanism at the basis of functional hyperemia is highly complex, not well understood, and may not necessarily be the same in all brain regions.

Therefore, it is useful to provide more background information about our working model --- primary visual cortex of macaque monkeys, which has been recognized as an excellent platform to study the neurovascular regulation. With regard to its specialty, the extension of the conclusions drawn from this model remains to be explored in the further study.

1.2.1   Cellular organization of V1

The primary visual cortex of mammals, variously called the striate cortex, area 17 or area V1, probably is the most intensively studied cortical structure in the mammalian brain [101]. Only the facts about V1 that are necessary in the scope of this thesis study are described here, particularly those relevant to the potential neural basis of the modeling analysis in Chapter 2. More information can be found in any textbook on neuroscience [102; 103].

Visual information flows from the retina to the lateral geniculate nucleus (LGN), which relays it on to V1. One conspicuous feature of this straightforward information flow is that the subcortical projections in the early sensory processing areas are topographically organized. For example, retinal ganglion cells (RGCs) project their axons to a variety of brain regions and different types of ganglion cells target distinct locations inside the brain. Receiving the projections from the RGCs, the LGN contains 6 major layers of neurons (1 – 6, ventral to dorsal, evident in sections stained for Nissl substance), which roughly is characterized into two different types: parvocellular (or P) (latin, parvus = small) and magnocellular (or M) (latin, magnus = large) [104]. The primary visual cortex

is widely accepted to organize horizontally into six laminae, and vertically into groups of cells linked synaptically across the horizontal laminae. The left column of Figure 1.3 summarizes the cellular layers information currently available, in which the dominant afferents projecting from the dorsal LGN of the thalamus to V1 terminate in Layers IV. Layer IV can be further subdivided into A, B and C [105]. Layer IVC is generally considered to consist of two sublayers: α and β, each of which receives specific thalamic inputs from distinct layers of the LGN (Magno and Parvo, respectively). In addition, Layer IV has the highest vascular density of V1 as demonstrated in the right side of Figure 1.3 (cortical vascular layers).

1.2.2   Vascular organization of V1

Because there is no local energy reserve in the cortical tissue, the brain requires extremely sensitive and efficient control of blood flow. Evidence for a fine level of vascular control is found in the striate cortex where the vasculature is organized with a distinct vertical organization into 4 vascular layers [106].

Examination of Fig.1.3 shows that microvessel density differs markedly from layer to layer. The first cortical vascular layer is within the molecular layer (Layer I) and has the lowest vascular density. It is important to note the absence of a capillary network at the cortex surface (superficial layers) [106]. Only those pial vessels with relatively large diameter are situated on the cortical surface. The second vascular layer is within the most superficial part of the pyramidal layer (Layer IIIa and b), and it is a network of parallel vessels perpendicular to the surface. The third vascular layer is found in the middle part of the cortex, and includes the innermost part of the pyramidal layer (Layer IIIc), the internal granular layer (IV) and part of the ganglionic layer (Va). Layer IVC receiving the
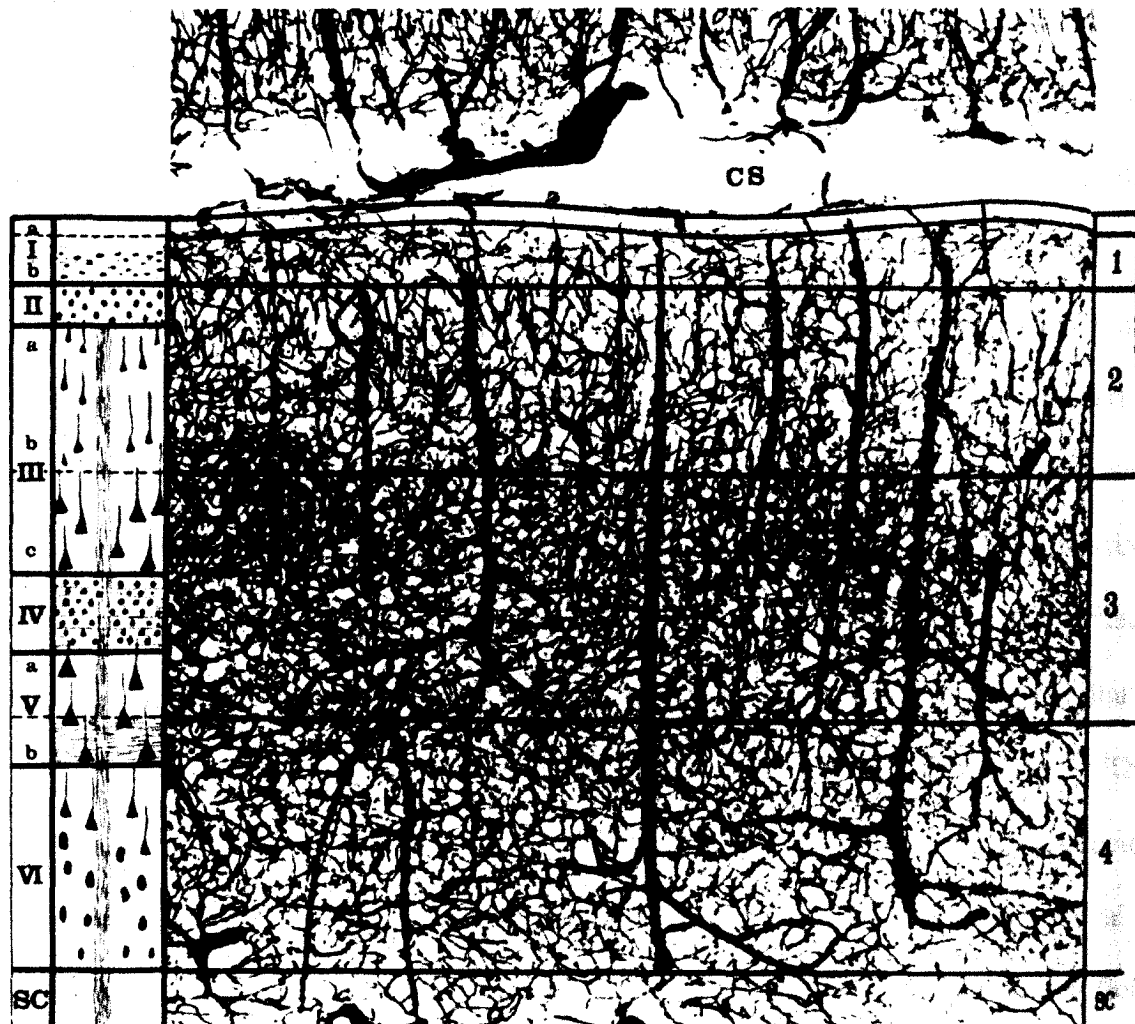
Figure 1.3 The left-hand column indicates the situation of six cortical cellular layers and of the nerve cells and fibers, where layer IV receives most of thalamic inputs from the LGN. The right-hand top panel shows the four cortical vascular layers. Note the vascular layer where the penetrating arteries have highest density of branches corresponds to the cellular layer IV. SC, subcortical white matter; CS, cingulated sulcus. See Section 1.2.1 and 1.2.2 for detailed description. Figure reprinted, with permission, from REF.96 © (1981) Elsevier Limited (Appendix A).

major thalamic inputs has greatest vascular density, which is around 3 times higher than that of Layer I [107]. And the middle cortical layer is known to have the highest cytochrome oxidase activity, metabolic rate, and density of synapses [59]. The fourth vascular layer corresponds to the deep cellular layers of the cortex (Vb and VI). At this level, the vascular network diminishes in intensity until reaching the white matter.

From an anatomic standpoint, there are clear hierarchical connections between the cerebrovasculature and the brain parenchyma (see detailed review [31]). The pial arteries with relatively large diameter on the cortical surface branch into smaller arteries and arterioles that enter the brain tissue, called the penetrating arterioles. These penetrating arterioles with an inter-vessel distance of ~250μm branch into secondary and tertiary arterioles until they reach the smallest vessel supplying the brain tissue, the capillary, which is only wide enough for one red blood cell to pass through it at a time [108]. The capillaries then feed into the venuoles and veins that carry the blood away. The collector veins emerge from the cortex perpendicular to the cortical surface, which is also considered as a major confounding source of the BOLD signal detected in the low field MR scanner.

Such intriguing configuration of microvasculature in the primary visual cortex has been discovered as earlier as in 1831 by Hall, who stated that "the number and distribution of the minute and capillary vessels is accurately proportioned and adapted to the object of the circulation" [109]. The functional significance of this arrangement in nature is still unknown.

It has been unveiled that the cerebral vasculature is endowed with sphincter-like structures that are often strategically placed at arteriolar branch points [61]. It is now widely

accepted that these sphincter-like structures play a vital part of controlling the local distribution of flow within the vascular network by neural projections. More recent work reveals that the blood flow control can be initiated in capillaries where pericytes contain contractile proteins, and not only regulated by precapillary arterioles [62]. It suggests that the pericytes were responsible for constricting and relaxing the capillary itself [110]. Given that capillaries can be found with ~24 μm spacing in primary sensory cortex [111], this finding hints that the brain is physiologically capable of regulating hemodynamics at a very fine spatial scale [62]. A number of optical imaging studies have demonstrated that the columnar structure of V1 could be visualized by using this spatially specific hemodynamic regulation in the horizontal direction [112; 113]. It is consistent with the conclusions from other functional studies that individual capillaries have the power to precisely irrigate a small population of activated neurons and glial cells during external stimulation [110; 114; 115].

This fact has a very important implication for vascular-based functional neuroimaging techniques. Today with hardware performance greatly improved, the physical spatial resolution of the imaging technique *per se* does not necessarily limit the functional spatial resolution [116]. It is most likely determined by the spatial specificity of the coupling between neuronal activity and the associated hemodynamic responses. Therefore, one could take advantage of such refined regulation of microcirculation to boost the functional spatiotemporal resolution and image more subtle functional structures in the brain. That is to say, those distinct layers in V1 can possibly be mapped by the functional imaging techniques. This theory was confirmed by the results from two separate groups by using optical measurements [35; 117], one of which made the statement "We provide direct

evidence in favor of a laminar-specific regulation of CBF in deep cortical layers, independent of dilatation of surface vessels" [35]. The spatial laminar specificity has also been demonstrated in the primary visual cortex of cats and monkeys with with fMRI technique [118; 119].

This overview suggests that a single-point hemodynamic measure (e.g., a LDF probe positioned on the surface of the exposed cortex) may reflect a spatial integration of signals originating from distinct layers, as one recent study has concluded [117]. Depending on the spatial extent of the neuronal activation, the complex spatial integration of the hemodynamic response merits careful consideration when analyzing and interpreting functional imaging data.

1.3 Thesis overview

It has been shown that the hemodynamic response observed at a given location is a spatiotemporal convolution of the neuronal activation [117]. Accurate analysis and interpretation of fMRI data requires in-depth knowledge of the neurovascular regulation, in particular for high resolution imaging applications. The conventional linear transform model is limited by the spatial extent of the activated neuron population. When distinct neuronal processes are involved in a single cognitive task, each of them may initiate distinctive regulatory mechanisms to control circulation supply and meet their individual energy demands. By using a mathematical model analysis of neuronal and CBF data acquired from awake animals, we identified two distinctly tuned hemodynamic responses which indicates the spatial-specific neurovascular regulation in V1. To spatially pinpoint the diversified hemodynamic responses, a high-resolution optical imaging technique was

developed to directly visualize spatial distribution of blood flow at submillimeter level. The thesis was completed as part of my Medical Biophysics PhD program at the University of Western Ontario under the supervision of Dr. Ravi Menon. This section provides an overview of the thesis contents and details my specific contributions.

1.3.1 Neural-hemodynamics modeling

To avoid confounding effects from anesthesia, I managed to implement extracellular recording in V1 of rhesus macaques while they were consciously viewing a standard pattern of stimulus. After implanting an artificial dura inside the recording chamber, the Laser Doppler method was used to provide the point-source CBF measurements on the awake preparations by using the same stimulation paradigms. LFP and MUA were separated from extracellular recordings by bandpass filters. The LFP was further processed in time-frequency domain by short-time Fourier transform with multi-taper method. Based on our neural and hemodynamics data acquired with varying stimulus durations (0.5, 1.0, 2.0, 3.0 s), the traditional linear convolution model was examined in the time domain. Considering the specialized cellular and vascular organization of the striate cortex, a novel two-component linear model was proposed in attempt to more accurately reflect the intrinsic regulation of neurovascular responses in V1. A description of this work including many unpublished details of working on alert macaques is presented in Chapter 2. Part of this work is being submitted to Nature Neuroscience, Wang Z, Menon RS. *Parallel hemodynamic regulation matches phasic-tonic neural responses in the primary visual cortex.*

1.3.2 Imaging CBF

A single-point hemodynamic measure could be a measure of complex spatial integration of electrophysiological activity over a given location [117], which is consistent with the model proposed above. To understand the spatial extent of the physiological integration imposed by neuronal response, one has to rely on some flow imaging techniques with adequate spatial and temporal resolution to map the spatial distribution of local CBF responses. As introduced above, the LSCI method has great potential to accomplish this goal. To this end, I set up the LSCI hardware system and re-examined two overlooked assumptions hidden in the widely cited LSCI paper of Fercher and Briers since 1981. And I made a complete theoretical analysis and developed an efficient strategy to realize submillimeter visualization of cerebral microcirculation. The experimental evidence was acquired from the classic carbon dioxide challenge model on the anesthetized animals to validate our theoretical analysis. This work, presented in Chapter 3, was published in Wang Z, Hughes S, Dayasundara S, Menon RS. *Theoretical and experimental optimization of laser speckle contrast imaging for high specificity to assess brain microcirculation*. J Cereb Blood Flow & Metab, 2007, 27:258-269.

The last chapter of this thesis summarizes the work I have done in the course of my PhD project and also briefly discuss some potential research interests in the future.

1.4 References

1.   Sokoloff L. Circulation in the central nervous system. In Greger R, Windhorst U, editors. Comprehensive human physiology. Springer-Verlag: Berlin, 1996: 561-578.

2.   Roy CS, Sherrington CS. On the Regulation of the Blood-supply of the Brain. J Physiol, 1890; 11: 85-158 117.

3.   Ogawa S, Lee TM, Kay AR, Tank DW. Brain magnetic resonance imaging with contrast dependent on blood oxygenation. Proc Natl Acad Sci U S A, 1990; 87: 9868-9872.

4.   Thulborn KR, Waterton JC, Matthews PM, Radda GK. Oxygenation dependence of the transverse relaxation time of water protons in whole blood at high field. Biochim Biophys Acta, 1982; 714: 265-270.

5.   Bandettini PA, Wong EC, Hinks RS, Tikofsky RS, Hyde JS. Time course EPI of human brain function during task activation. Magn Reson Med, 1992; 25: 390-397.

6.   Belliveau JW, Kennedy DN, Jr., McKinstry RC, Buchbinder BR, Weisskoff RM, Cohen MS, Vevea JM, Brady TJ, Rosen BR. Functional mapping of the human visual cortex by magnetic resonance imaging. Science, 1991; 254: 716-719.

7.   Kwong KK, Belliveau JW, Chesler DA, Goldberg IE, Weisskoff RM, Poncelet BP, Kennedy DN, Hoppel BE, Cohen MS, Turner R, et al. Dynamic magnetic resonance imaging of human brain activity during primary sensory stimulation. Proc Natl Acad Sci U S A, 1992; 89: 5675-5679.

8.   Menon RS, Ogawa S, Kim SG, Ellermann JM, Merkle H, Tank DW, Ugurbil K. Functional brain mapping using magnetic resonance imaging: signal changes accompanying visual stimulation. Invest Radiol, 1992; 27 Suppl 2: S47-53.

9.   Ogawa S, Tank DW, Menon R, Ellermann JM, Kim SG, Merkle H, Ugurbil K. Intrinsic signal changes accompanying sensory stimulation: functional brain mapping with magnetic resonance imaging. Proc Natl Acad Sci U S A, 1992; 89: 5951-5955.

10.   D'Esposito M, Deouell LY, Gazzaley A. Alterations in the BOLD fMRI signal with ageing and disease: a challenge for neuroimaging. Nat Rev Neurosci, 2003; 4: 863-872.

11.   Gusnard DA, Raichle ME. Searching for a baseline: functional imaging and the resting human brain. Nat Rev Neurosci, 2001; 2: 685-694.

12.   Heeger DJ, Ress D. What does fMRI tell us about neuronal activity? Nat Rev Neurosci, 2002; 3: 142-151.

13.   Iadecola C. Neurovascular regulation in the normal brain and in Alzheimer's disease. Nat Rev Neurosci, 2004; 5: 347-360.

14.   Lauritzen M. Reading vascular changes in brain imaging: is dendritic calcium the key? Nat Rev Neurosci, 2005; 6: 77-85.

15.   Logothetis NK, Wandell BA. Interpreting the BOLD signal. Annu Rev Physiol, 2004; 66: 735-769.

16. Menon RS. Imaging function in the working brain with fMRI. Curr Opin Neurobiol, 2001; 11: 630-636.

17. Kasischke KA, Vishwasrao HD, Fisher PJ, Zipfel WR, Webb WW. Neural activity triggers neuronal oxidative metabolism followed by astrocytic glycolysis. Science, 2004; 305: 99-103.

18. Malonek D, Grinvald A. Interactions between electrical activity and cortical microcirculation revealed by imaging spectroscopy: implications for functional brain mapping. Science, 1996; 272: 551-554.

19. Thompson JK, Peterson MR, Freeman RD. Single-neuron activity and tissue oxygenation in the cerebral cortex. Science, 2003; 299: 1070-1072.

20. Vanzetta I, Grinvald A. Increased cortical oxidative metabolism due to sensory stimulation: implications for functional brain imaging. Science, 1999; 286: 1555-1558.

21. Chen-Bee CH, Agoncillo T, Xiong Y, Frostig RD. The triphasic intrinsic signal: implications for functional imaging. J Neurosci, 2007; 27: 4572-4586.

22. Fox PT, Raichle ME. Focal physiological uncoupling of cerebral blood flow and oxidative metabolism during somatosensory stimulation in human subjects. Proc Natl Acad Sci U S A, 1986; 83: 1140-1144.

23. Fox PT, Raichle ME, Mintun MA, Dence C. Nonoxidative glucose consumption during focal physiologic neural activity. Science, 1988; 241: 462-464.

24. Peppiatt C, Attwell D. Neurobiology: feeding the brain. Nature, 2004; 431: 137-138.

25. Ogawa S, Menon RS, Tank DW, Kim SG, Merkle H, Ellermann JM, Ugurbil K. Functional brain mapping by blood oxygenation level-dependent contrast magnetic resonance imaging. A comparison of signal characteristics with a biophysical model. Biophys J, 1993; 64: 803-812.

26. Lemon R. Methods for neuronal recording in conscious animals. John Wiley & Sons: New York, 1984.

27. Legatt AD, Arezzo J, Vaughan HG, Jr. Averaged multiple unit activity as an estimate of phasic changes in local neuronal activity: effects of volume-conducted potentials. J Neurosci Methods, 1980; 2: 203-217.

28. Logothetis NK. The underpinnings of the BOLD functional magnetic resonance imaging signal. J Neurosci, 2003; 23: 3963-3971.

29.   Attwell D, Iadecola C. The neural basis of functional brain imaging signals. Trends Neurosci, 2002; 25: 621-625.

30.   Attwell D, Laughlin SB. An energy budget for signaling in the grey matter of the brain. J Cereb Blood Flow Metab, 2001; 21: 1133-1145.

31.   Drake CT, Iadecola C. The role of neuronal signaling in controlling cerebral blood flow. Brain Lang, 2007; 102: 141-152.

32.   Logothetis NK, Pauls J, Augath M, Trinath T, Oeltermann A. Neurophysiological investigation of the basis of the fMRI signal. Nature, 2001; 412: 150-157.

33.   Viswanathan A, Freeman RD. Neurometabolic coupling in cerebral cortex reflects synaptic more than spiking activity. Nat Neurosci, 2007; 10: 1308-1312.

34.   Niessing J, Ebisch B, Schmidt KE, Niessing M, Singer W, Galuske RA. Hemodynamic signals correlate tightly with synchronized gamma oscillations. Science, 2005; 309: 948-951.

35.   Caesar K, Thomsen K, Lauritzen M. Dissociation of spikes, synaptic activity, and activity-dependent increments in rat cerebellar blood flow by tonic synaptic inhibition. Proc Natl Acad Sci U S A, 2003; 100: 16000-16005.

36.   Mukamel R, Gelbard H, Arieli A, Hasson U, Fried I, Malach R. Coupling between neuronal firing, field potentials, and FMRI in human auditory cortex. Science, 2005; 309: 951-954.

37.   Disbrow EA, Slutsky DA, Roberts TP, Krubitzer LA. Functional MRI at 1.5 tesla: a comparison of the blood oxygenation level-dependent signal and electrophysiology. Proc Natl Acad Sci U S A, 2000; 97: 9718-9723.

38.   Raichle ME, Mintun MA. Brain work and brain imaging. Annu Rev Neurosci, 2006; 29: 449-476.

39.   Rees G, Friston K, Koch C. A direct quantitative relationship between the functional properties of human and macaque V5. Nat Neurosci, 2000; 3: 716-723.

40.   Smith AJ, Blumenfeld H, Behar KL, Rothman DL, Shulman RG, Hyder F. Cerebral energetics and spiking frequency: the neurophysiological basis of fMRI. Proc Natl Acad Sci U S A, 2002; 99: 10765-10770.

41.   Nir Y, Fisch L, Mukamel R, Gelbard-Sagiv H, Arieli A, Fried I, Malach R. Coupling between neuronal firing rate, gamma LFP, and BOLD fMRI is related to interneuronal correlations. Curr Biol, 2007; 17: 1275-1285.

42.   Kreiman G. Brain science: from the very small to the very large. Curr Biol, 2007; 17: R768-770.

43.   Birn RM, Saad ZS, Bandettini PA. Spatial heterogeneity of the nonlinear dynamics in the FMRI BOLD response. Neuroimage, 2001; 14: 817-826.

44.   Boynton GM, Engel SA, Glover GH, Heeger DJ. Linear systems analysis of functional magnetic resonance imaging in human V1. J Neurosci, 1996; 16: 4207-4221.

45.   Friston KJ, Josephs O, Rees G, Turner R. Nonlinear event-related responses in fMRI. Magn Reson Med, 1998; 39: 41-52.

46.   Glover GH. Deconvolution of impulse response in event-related BOLD fMRI. Neuroimage, 1999; 9: 416-429.

47.   Pfeuffer J, McCullough JC, Van de Moortele PF, Ugurbil K, Hu X. Spatial dependence of the nonlinear BOLD response at short stimulus duration. Neuroimage, 2003; 18: 990-1000.

48.   Vazquez AL, Noll DC. Nonlinear aspects of the BOLD response in functional MRI. Neuroimage, 1998; 7: 108-118.

49.   Buckner RL. The hemodynamic inverse problem: making inferences about neural activity from measured MRI signals. Proc Natl Acad Sci U S A, 2003; 100: 2177-2179.

50.   Friston KJ. Models of brain function in neuroimaging. Annu Rev Psychol, 2005; 56: 57-87.

51.   Buckner RL, Bandettini PA, O'Craven KM, Savoy RL, Petersen SE, Raichle ME, Rosen BR. Detection of cortical activation during averaged single trials of a cognitive task using functional magnetic resonance imaging. Proc Natl Acad Sci U S A, 1996; 93: 14878-14883.

52.   Dale AM, Buckner RL. Selective averaging of rapidly presented individual trials using fMRI. Hum Brain Mapp, 1997; 5: 329-340.

53.   Buxton RB, Frank LR. A model for the coupling between cerebral blood flow and oxygen metabolism during neural stimulation. J Cereb Blood Flow Metab, 1997; 17: 64-72.

54.   Buxton RB, Uludag K, Dubowitz DJ, Liu TT. Modeling the hemodynamic response to brain activation. Neuroimage, 2004; 23 Suppl 1: S220-233.

55.   Mandeville JB, Marota JJ, Ayata C, Zaharchuk G, Moskowitz MA, Rosen BR, Weisskoff RM. Evidence of a cerebrovascular postarteriole windkessel with delayed compliance. J Cereb Blood Flow Metab, 1999; 19: 679-689.

56.   Hoffmeyer HW, Enager P, Thomsen KJ, Lauritzen MJ. Nonlinear neurovascular coupling in rat sensory cortex by activation of transcallosal fibers. J Cereb Blood Flow Metab, 2007; 27: 575-587.

57.   Martindale J, Berwick J, Martin C, Kong Y, Zheng Y, Mayhew J. Long duration stimuli and nonlinearities in the neural-haemodynamic coupling. J Cereb Blood Flow Metab, 2005; 25: 651-661.

58.   Miller KL, Luh WM, Liu TT, Martinez A, Obata T, Wong EC, Frank LR, Buxton RB. Nonlinear temporal dynamics of the cerebral blood flow response. Hum Brain Mapp, 2001; 13: 1-12.

59.   Woolsey TA, Rovainen CM, Cox SB, Henegar MH, Liang GE, Liu D, Moskalenko YE, Sui J, Wei L. Neuronal units linked to microvascular modules in cerebral cortex: response elements for imaging the brain. Cereb Cortex, 1996; 6: 647-660.

60.   Edvinsson L, Hamel E. Perivascular nerves in brain vessels. In Edvinsson L, Krause DN, editors. Cerebral blood flow and metabolism. Lippincott, Williams and Wilkins: Philadelphia, 2002.

61.   Harrison RV, Harel N, Panesar J, Mount RJ. Blood capillary distribution correlates with hemodynamic-based functional imaging in cerebral cortex. Cereb Cortex, 2002; 12: 225-233.

62.   Peppiatt CM, Howarth C, Mobbs P, Attwell D. Bidirectional control of CNS capillary diameter by pericytes. Nature, 2006; 443: 700-704.

63.   Haydon PG, Carmignoto G. Astrocyte control of synaptic transmission and neurovascular coupling. Physiol Rev, 2006; 86: 1009-1031.

64.   Kety SS, Schmidt CF. The determination of cerebral blood flow in man by the use of nitrous oxide in low concentrations. Am J Physiol, 1945; 143: 53-67.

65.   Cameron BD. Determination of regional cerebral cortical blood flow using a heat clearance technique. Phys Med Biol, 1970; 15: 715-722.

66.   Martins AN, Kobrine AI, Doyle TF, Ramirez A. Total cerebral blood flow in the monkey measured by hydrogen clearance. Stroke, 1974; 5: 512-517.

67.   Dumoulin CL, Hart HR, Jr. Magnetic resonance angiography. Radiology, 1986; 161: 717-720.

68.   Hoskins PR. Measurement of arterial blood flow by Doppler ultrasound. Clin Phys Physiol Meas, 1990; 11: 1-26.

69.   Stern MD. In vivo evaluation of microcirculation by coherent light scattering. Nature, 1975; 254: 56-58.

70.   Briers JD. Laser Doppler, speckle and related techniques for blood perfusion mapping and imaging. Physiol Meas, 2001; 22: 35-66.

71.   Edwards AD, Wyatt JS, Richardson C, Delpy DT, Cope M, Reynolds EO. Cotside measurement of cerebral blood flow in ill newborn infants by near infrared spectroscopy. Lancet, 1988; 2: 770-771.

72.   Cenic A, Nabavi DG, Craen RA, Gelb AW, Lee TY. Dynamic CT measurement of cerebral blood flow: a validation study. AJNR Am J Neuroradiol, 1999; 20: 63-73.

73.   Meyer JS, Hayman LA, Yamamoto M, Sakai F, Nakajima S. Local cerebral blood flow measured by CT after stable xenon inhalation. AJR Am J Roentgenol, 1980; 135: 239-251.

74.   Ginsberg MD, Lockwood AH, Busto R, Finn RD, Campbell JA, Boothe TE. 11C-Iodoantipyrine for the measurement of regional cerebral blood flow by positron emission tomography. Validation studies. Stroke, 1981; 12: 745-750.

75.   Detre JA, Subramanian VH, Mitchell MD, Smith DS, Kobayashi A, Zaman A, Leigh JS, Jr. Measurement of regional cerebral blood flow in cat brain using intracarotid 2H2O and 2H NMR imaging. Magn Reson Med, 1990; 14: 389-395.

76.   Chen LM, Heider B, Williams GV, Healy FL, Ramsden BM, Roe AW. A chamber and artificial dura method for long-term optical imaging in the monkey. J Neurosci Methods, 2002; 113: 41-49.

77.   Arieli A, Grinvald A, Slovin H. Dural substitute for long-term imaging of cortical activity in behaving monkeys and its clinical implications. J Neurosci Methods, 2002; 114: 119-133.

78.   Tanaka T, Riva C, Ben-Sira B. Blood velocity measurements in human retinal vessels. Science, 1974; 186: 830-831.

79.   Bonner R, Nossal R. Model for laser Doppler measurements of blood flow in tissue. Appl Opt, 1981; 20: 2097-2107.

80.   Rajan V, Varghese B, van Leeuwen TG, Steenbergen W. Review of methodological developments in laser Doppler flowmetry. Lasers Med Sci, 2008.

81.   Wang L, Jacques SL, Zheng L. MCML--Monte Carlo modeling of light transport in multi-layered tissues. Comput Methods Programs Biomed, 1995; 47: 131-146.

82.   Bonner RF, Nossal R, Havlin S, Weiss GH. Model for photon migration in turbid biological media. J Opt Soc Am A, 1987; 4: 423-432.

83.   Carter LP. Surface monitoring of cerebral cortical blood flow. Cerebrovasc Brain Metab Rev, 1991; 3: 246-261.

84.   Dirnagl U, Kaplan B, Jacewicz M, Pulsinelli W. Continuous measurement of cerebral cortical blood flow by laser-Doppler flowmetry in a rat stroke model. J Cereb Blood Flow Metab, 1989; 9: 589-596.

85.   Fabricius M, Akgoren N, Dirnagl U, Lauritzen M. Laminar analysis of cerebral blood flow in cortex of rats by laser-Doppler flowmetry: a pilot study. J Cereb Blood Flow Metab, 1997; 17: 1326-1336.

86.   Florence G, Seylaz J. Rapid autoregulation of cerebral blood flow: a laser-Doppler flowmetry study. J Cereb Blood Flow Metab, 1992; 12: 674-680.

87.   Haberl RL, Heizer ML, Ellis EF. Laser-Doppler assessment of brain microcirculation: effect of local alterations. Am J Physiol, 1989; 256: H1255-1260.

88.   Iadecola C, Reis DJ. Continuous monitoring of cerebrocortical blood flow during stimulation of the cerebellar fastigial nucleus: a study by laser-Doppler flowmetry. J Cereb Blood Flow Metab, 1990; 10: 608-617.

89.   Pusey PN. Photon correlation study of laser speckle produced by a moving rough surface. J Phys, 1976; 9: 1399-1409.

90.   Briers JD. Laser Doppler and time-varying speckle: a reconciliation. J Opt Soc Am, 1996; 13: 345-350.

91.   Rigden JD, Gordon EI. The granularity of scattered optical maser light. Proc IRE, 1962; 50: 2.

92.   Goodman JW. Some effects of target-induced scintillations on optical radar performance. Proc IEEE, 1965; 53: 1688-1700.

93.   Ohtsubo J, Asakura T. Velocity measurement of a diffuse object by using time-varying speckles. Opt Quant Electr, 1976; 8: 523-529.

94.   Goodman JW. Speckle phenomena in optics: theory and applications. Greenwood Village: Roberts & company, 2006.

95.   Fercher AF, Briers JD. Flow visualization by means of single-exposure speckle photography. Opt Commun, 1981; 37: 326-329.

96.   GoldFischer LI. Autocorrelation function and power spectral density of laser-produced speckle patterns. J Opt Soc Am, 1965; 55: 247-253.

97.   Goodman JW. Statistical properties of laser speckle patterns. In Dainty JC, editor. Laser speckle and related topics. Springer-Verlag: Berlin, 1975: 9-75.

98.   Bolay H, Reuter U, Dunn AK, Huang Z, Boas DA, Moskowitz MA. Intrinsic brain activity triggers trigeminal meningeal afferents in a migraine model. Nat Med, 2002; 8: 136-142.

99.   Dunn AK, Bolay H, Moskowitz MA, Boas DA. Dynamic imaging of cerebral blood flow using laser speckle. J Cereb Blood Flow Metab, 2001; 21: 195-201.

100.   Iadecola C, Goldman SS, Harder DR, Heistad DD, Katusic ZS, Moskowitz MA, Simard JM, Sloan MA, Traystman RJ, Velletri PA. Recommendations of the National Heart, Lung, and Blood Institute working group on cerebrovascular biology and disease. Stroke, 2006; 37: 1578-1581.

101.   Callaway EM. Local circuits in primary visual cortex of the macaque monkey. Annu Rev Neurosci, 1998; 21: 47-74.

102.   Kandel ER, Schwartz JH, Jessel TM. Principles of neural science, 4th ed. McGraw-Hill, 2000.

103.   Nicholls JG, Wallace BG, Martin AR, Fuchs PA. From neuron to brain, 4th ed. Sinauer Associates, 2001.

104.   Merigan WH, Maunsell JH. How parallel are the primate visual pathways? Annu Rev Neurosci, 1993; 16: 369-402.

105.   Lund JS. Anatomical organization of macaque monkey striate visual cortex. Annu Rev Neurosci, 1988; 11: 253-288.

106.   Duvernoy HM, Delon S, Vannson JL. Cortical blood vessels of the human brain. Brain Res Bull, 1981; 7: 519-579.

107.   Zheng D, LaMantia AS, Purves D. Specialized vascularization of the primate visual cortex. J Neurosci, 1991; 11: 2622-2629.

108.   McHedlishvili G, Kuridze N. The modular organization of the pial arterial system in phylogeny. J Cereb Blood Flow Metab, 1984; 4: 391-396.

109.   Hall M. A critical and exprimental essay on the circulation of the blood. Seeley and Burnside: London, 1831.

110.   Chaigneau E, Oheim M, Audinat E, Charpak S. Two-photon imaging of capillary blood flow in olfactory bulb glomeruli. Proc Natl Acad Sci U S A, 2003; 100: 13081-13086.

111.   Pawlik G, Rackl A, Bing RJ. Quantitative capillary topography and blood flow in the cerebral cortex of cats: an in vivo microscopic study. Brain Res, 1981; 208: 35-58.

112.   Grinvald A, Frostig RD, Siegel RM, Bartfeld E. High-resolution optical imaging of functional brain architecture in the awake monkey. Proc Natl Acad Sci U S A, 1991; 88: 11559-11563.

113.   Grinvald A, Lieke E, Frostig RD, Gilbert CD, Wiesel TN. Functional architecture of cortex revealed by optical imaging of intrinsic signals. Nature, 1986; 324: 361-364.

114.   Chaigneau E, Tiret P, Lecoq J, Ducros M, Knopfel T, Charpak S. The relationship between blood flow and neuronal activity in the rodent olfactory bulb. J Neurosci, 2007; 27: 6452-6460.

115.   Kleinfeld D, Mitra PP, Helmchen F, Denk W. Fluctuations and stimulus-induced changes in blood flow observed in individual capillaries in layers 2 through 4 of rat neocortex. Proc Natl Acad Sci U S A, 1998; 95: 15741-15746.

116.   Wang Z, Hughes S, Dayasundara S, Menon RS. Theoretical and experimental optimization of laser speckle contrast imaging for high specificity to brain microcirculation. J Cereb Blood Flow Metab, 2007; 27: 258-269.

117.   Devor A, Ulbert I, Dunn AK, Narayanan SN, Jones SR, Andermann ML, Boas DA, Dale AM. Coupling of the cortical hemodynamic response to cortical and thalamic neuronal activity. Proc Natl Acad Sci U S A, 2005; 102: 3822-3827.

118.   Goense JB, Logothetis NK. Laminar specificity in monkey V1 using high-resolution SE-fMRI. Magn Reson Imaging, 2006; 24: 381-392.

119.   Zhao F, Wang P, Hendrich K, Ugurbil K, Kim SG. Cortical layer-dependent BOLD and CBV responses measured by spin-echo and gradient-echo fMRI: insights into hemodynamic regulation. Neuroimage, 2006; 30: 1149-1160.

Chapter 2 Modeling neural-hemodynamics in V1[1]

Characterization of cerebral hemodynamic responses is essential for inferring the activated locations of the brain in functional magnetic resonance imaging technique. Here we present intracortical recordings of neural signals and blood flow responses from the primary visual cortex in two awake macaques. A novel two-component linear convolution model was proposed to describe the parallel characteristic of neurovascular regulation and validated in time domain by manipulating the duration of visual stimulation.

2.1 Introduction

Understanding the relationship between stimulus-induced or task-associated neural activity (NA) and the blood oxygenation level dependent (BOLD) response is of fundamental importance for the accurate modeling and interpretation of functional

---

[1] A modified version of this chapter is being prepared to submit as journal article. Wang Z, Menon RS. *Parallel hemodynamic regulation matches phasic-tonic neural responses in the primary visual cortex.*

magnetic resonance imaging (fMRI) studies[1-3]. It is invariably assumed that the BOLD response in a given brain area can be predicted by the linear convolution of the NA and a single hemodynamic impulse response function (HRF)[4]. Judicious selection of a HRF and assumptions about the nature of the NA are critical first steps in the ubiquitous general linear model (GLM) analyses of fMRI data sets[4; 5]. However, several studies have shown that the BOLD response is a nonlinear function of the stimulus duration[2; 4; 6; 7]. Since the BOLD signal reflects a complex interplay of neuronal, metabolic, hemodynamic and MRI parameters[8], the origin and significance of this nonlinearity is not clear. Recent studies revealed that the nonlinear dependence of the BOLD signal on stimulus duration has been attributed to factors such as anaesthesia, attention, inhibition or nonlinearities in the BOLD-NA signal transduction pathway[8]. The BOLD-NA coupling depends on many physiological and MRI variables[1; 2; 8; 9], but at its root is the fundamental relationship between CBF and NA[10; 11]. Several groups have reported that the shape of the CBF response also depends strongly on the stimulus duration[12; 13], suggesting that the source of the nonlinearity is quite fundamental. Avoiding the profound consequences on CBF and NA that accompany anaesthesia, we address this issue by measuring the temporal dynamics of stimulus induced NA and its evoked hemodynamic responses in the primary visual cortex of awake primates. Here we identify a rapid biphasic HRF and a slower monophasic HRF which, respectively, relate the transient and sustained components of the stimulus-induced spectral density (SD) of the local field potential (LFP) to the cerebral blood flow (CBF) response in the primary visual cortex (V1) of awake animals. The unmasking of two CBF responses was accomplished using a stable deconvolution of the observed CBF and a measure of the NA that relates to neural energy consumption

(integral of the SD of the LFP). Beyond the implications for fMRI analysis and BOLD biophysical models, our findings demonstrate that there exist two distinctly tuned CBF regulatory mechanisms in primate cortex. One appears to support the high energy demands typical of transient NA and the other the more modest demands of sustained NA.

2.2 Theory

As mentioned in Chapter 1 (section 1.1.3), the traditional linear transform model actually makes an assumption that the brain allocates only one neural process (thus leading to a single HRF) to respond that cognitive task. Although this is a good approximation in most of cases, it sometimes produces some mysterious conclusion. For example, the shorter visual stimulus (less than 3 or 4s) has nonlinear response in V1 but longer duration of the same stimulus yields linear results in the same region [3; 4; 15]. Typically, the principle of superposition as a simple way is used to examine the validity of a linear system [14]. If the responses of a system to inputs x1 and x2 are Y(x1) and Y(x2), then a linear system requires Y(x1 + x2) is equal to Y(x1) + Y(x2). This is the property of additivity. In addition, if the response of a system to input a×x, where a is a scalar constant, is Y(ax) then a linear system requires Y(ax) is equal to a×Y(x). This is the property of scaling. It is important to mention that increasing the duration of the stimulus will not cause a scaled increase in the resultant hemodynamic response in a linear system as it would for a change in stimulus intensity. The effect of changing duration can be predicted with a test of additivity, that is, shifting and summing the responses to shorter stimuli, the durations of which add up to the duration of the longer stimulus. For the

purposes of this experiment, only the parameter of duration was tested in examining the linearity of the CBF response.

An alternative way to test the linearity of a system is by estimating the impulse response function due to several different inputs. The impulse response function in a discrete time system can be defined as the response of a system to an input stimulus of unit time, or brief input (0.5 s in the case of typical CBF data). The response to a stimulus of longer duration, CBF_τ, can be found by convolving the stimulus function, $u(t)$, with the impulse response function, $HRF(t)$,

$$CBF_\tau = HRF(t) \otimes u(t) \qquad [2.1]$$

For a linear system, the impulse response function would be the same for any stimulus duration. In a nonlinear system, the impulse response function would not be the same for the inputs with different time durations.

Taking account of the potential fact that there might exist two or more neural processes responsible for one single visual stimulus input, a two-component linear convolution model consisting of transient and sustained response components (TR and SR) in our experiments was proposed to fit each averaged CBF response, CBF_τ, for stimulus duration τ:

$$CBF_\tau = u_{TR} \otimes HRF_{TR}(t) + u_{SR_\tau} \otimes HRF_{SR}(t) \qquad [2.2]$$

where HRF_{TR}, HRF_{SR} is the HRFs corresponding to transient (u_{TR}) and sustained ($u_{SR\tau}$) components of neural responses respectively.

2.3 Materials and Methods

2.3.1 Animal preparation

Two male rhesus macaque monkeys (*Macaca mulatta*) aged 5 (monkey O, 8.2 kg) and aged 6 (monkey S, 9.5 kg) participated in the experiments. All training, surgical, and experimental procedures were performed in compliance with the Canadian Council on Animal Care Policy on the care and use of experimental animals and were approved by the Animal Use Subcommittee of the University of Western Ontario Council on Animal Care (Appendix B). Animals were under the close supervision of the university veterinarians.

Both animals were prepared for chronic experiments by undergoing three aseptic surgical procedures to place chronic implants and replacement of the dura matter. The implant included both a restraining head holder (Crist Instruments, MD, USA) and a low profile Cilux recording chamber (MRI compatible, Crist Instruments). Anesthesia was induced initially with an injection of ketamine (10 mg/kg i.m.) followed by propofol (2.0 ~ 5.0 mg/kg/i.v.) to allow for preparation of the surgical area and the insertion of a tracheal tube. Once intubated, the animals were maintained under isoflurane inhalation anaesthesia (iso 0.5 ~ 2% in O_2 and CO_2) titrated to keep surgical anesthesia. Body temperature was maintained with a heated blanket and continuously monitored. Heart rate, blood pressure, respiratory rate, and O_2 saturation were also monitored closely for the duration of the surgery. The recording chamber for electrical and optical recording *was placed on the posterior part of the skull over the primary visual cortex, specifically over the lunate sulcus*. Before surgery, the animals were scanned in the 9.4T horizontal MRI scanner (Varian, CA, USA) of our lab to obtain high-resolution structural MRI

images that allowed precisely localizing the recording chamber within V1 region. A circular craniotomy and durotomy was made by trephination inside the implanted chamber to expose the primary visual cortex. A hat-shape artificial dura (Tecoflex; Thermedics Polymer Products, Wilmington, MA, USA) was then placed to replace the native dura mater. A more detailed description of the dura replacement is available elsewhere [16]. After the surgery the exposed cortex in the cranial window was available for optical measurements through the transparent artificial dura mater. The chamber was meticulously cleaned with sterile saline at least three times a week, and carefully maintained for protection from infection. The fluid contents of the chamber were tested intermittently for bacterial sensitivity, and antibiotics were applied if necessary.

2.3.2 Visual stimulation

The present study did not seek to determine the tuning of individual neurons through the use of stimuli to which they are optimally sensitive, but rather, to examine the visual responses of neural populations. Thus, a full-field black-white radial checkerboard pattern was used with 8.0 Hz reversal flickering rate and 100% contrast, which was well known to evoke a robust increase in local blood flow in the striate cortex [17]. The checkerboard we used for data collection contained 18 radial spokes, 5 concentric bands and subtended to ~32° × 32° of visual angle on the LCD screen 58 cm in front of the subjects running at 60 Hz frame refresh rate. The remainder of the screen was gray, matched to the mean luminance of the stimulus. Monkeys usually performed 30~50 trials of the task in one recording session and each trial lasted for 8 seconds. Within each trial the durations of stimuli were varied for 0.5, 1.0, 2.0 and 3.0 s followed by the first second blank baseline. The onset of the checkerboard for each trial was chosen at random inter-

stimulus intervals from 10 to 20s and controlled by Powerlab (ADInstruments). Various short animated movie clips were played between recording sessions.

2.3.3 Electrophysiological recording

MUA and LFP activity were recorded inside the chamber simultaneously from a single Epoxylite-coated tungsten microelectrode (~1MΩ impedance measured at 1kHz, FHC Inst., Bowdoinham, ME, USA). Electrodes were advanced in the exposed cortex using an oil-hydraulic microdrive (Narishige, Japan) at a very slow rate (< 1.5 mm/s) to minimize suppression artifacts (dimpling). A Delrin grid (MRI-compatible) with 1 mm spacing between adjacent locations was fitted into the implanted chamber. The grid system was used here to work with microelectrodes, LDF probe and guide tubes, which allowed precise positioning and reproducible tracking.

The saline solution (0.9%) inside the chamber was found efficiently to suppress noises since a clear and dramatic reduction in the line-frequency noise could be seen once the reference electrode made contact with saline. However, our shallow chamber (which is prerequisite to high resolution optical imaging) posed problems when it was placed at posterior locations on the head (above the primary visual cortex). At such locations, the steep angle of the chamber to the vertical plane would not allow it to contain sufficient saline solution above the artificial dura. It might be one of the main reasons that the power line noise sneaked into the recorded LFP signal. The neural signal passed through a headstage and was further amplified with PBX2 wide-band preamplifier (Plexon, Dallas, TX, USA). Then the signal fed into Powerlab system (ADInstruments) was digitized at a sampling rate of 20kHz with 16bit resolution and converted to MATLAB compatible format for further analysis.

2.3.4 Electrical signal analysis

Two measures of neuronal activity were extracted from the recorded broadband signals: LFP and MUA. To estimate the temporal structure in the LFP, we applied classic time-frequency analysis after lowpassed and resampled the recorded signals at 250 Hz, i.e., the short-time Fourier transform, by repeatedly calculating a sliding-windowed fast Fourier transforms across the duration of the trial. The Thomson multitaper method was performed on a single-trial basis that allowed averaging in a more principled way than other nonparametric methods. The details of this method have been described extensively elsewhere [22] and its advantages on power estimation have been proven effectively on awake animals [23]. LFP spectrograms were computed with multi-taper spectral estimation by using Slepian tapers on a 250 ms windows and a 25 ms step size. Power line noise was removed with a notch filter in MATLAB. Computed spectrograms were normalized by the baseline mean frequency by frequency to better visualize the spectral structure and averaged across trials within one recording session. Again the grand mean spectrograms were obtained by renormalizing these normalized spectrograms from different sites based on their peak responses and scaled to the arbitrary range. The energy at all frequencies in each grand mean spectrogram was simply summed together at each time point and used in the following deconvolution process.

Multi-unit spiking activity was isolated from the amplified and filtered (800~5000 Hz) broadband signal and digitized at 20 kHz with 16 bit resolution. An arbitrary threshold was manually set (around 3 standard deviations above noise level) to collect the time stamps of spikes [24]. Each trial within one recording session was binned in 125 ms window and averaged to obtain the mean peristimulus-time histograms (PSTHs). In order

to pool MUAs over different recording sites, the averaged spike rates under each stimulus condition were normalized by their peak responses and scaled to the arbitrary range.

2.3.5 Laser Doppler recording

Through the transparent cranial window the Laser-doppler technique was capable of reliably detecting neural activity-induced blood flow responses. A clear image was taken by a CCD camera (Princeton Instruments, Trenton, NJ, USA) to present the distribution of blood vessels underneath the artificial dura. Thus visible large vessels were carefully avoided when the LDF probe (450 μm diameter, Oxford Optronix, UK) was positioned above the artificial dura through the guide tube. After stable readings were obtained, the probe was left at that position for the duration of the experiment. Sometimes a transparent silicon wafer (RTV615, GE Silicones, Wilton, CT, USA) was put inside the chamber to minimize pulsations. Laser Doppler signals from the exposed primary visual cortex recorded in blood perfusion units were fed into the multi-channel Powerlab system (ADInstruments) and digitized at 50 Hz. Since the increased blood flow decayed to the level of pre-stimulus slowly, we extended the trial duration from 8 to 10 seconds for longer stimulus (like 2.0, 3.0 s) in some recording sessions to observe that CBF responses returned to the baseline. In the awake animals greater variations of cardiac cycle were expected on a beat-to-beat basis, which introduced higher trial-to-trial variability in blood flow [18-20]. Therefore, cardiac cycle was recorded by a pulse oximeter (Benson Medical Industries Inc., Canada) and sampled by the Powerlab concurrently with the LDF signals. The CBF response during stimulation was defined as the percentage increase from the baseline mean preceding the stimulus in each individual trial and averaged across the trials [21]. If necessary, a window-based (Kaiser) finite impulse response filter was

designed to remove the cardiac fluctuations in CBF responses based on the frequency characteristics of recorded cardiac cycles. Some trials obviously contaminated with body movements from the animal were discarded.

2.3.6 Deconvolution with nonlinear curve fitting

In order to solve the HRFs in the above equations with a physiologically plausible shape, we limited our options by choosing the HRF with gamma function basis. Mathematically the HRF was represented by a composition of two gamma-variate functions that had tremendous flexibility of modeling some known properties of hemodynamics like biphasic [7]:

$$g(t) = \frac{1}{g_{max}} t^a \exp(-\frac{t}{b}), \qquad t \geq 0, a \geq 0, b > 0 \qquad [2.3]$$

$$h_{TC/SC}(t) = g_p(t) - \lambda g_n(t), \qquad \lambda \geq 0 \qquad [2.4]$$

where g_{max} is the maximum of $g(t)$ at $t = ab$. Subscripts p and n denote the positive and negative components, respectively, and λ denotes the relative contribution of the negative component. The deconvolution process was done by estimating the free parameters of the model through the use of a Levenberg-Marquardt algorithm (LMA) for nonlinear least-squares minimization (Matlab optimization function 'lsqnonlin'). Detailed description of the LMA and its usage can be found in the Help of MATLAB routine or the classic book [25]. This algorithm is very popular and more robust than others like Gauss-Newton algorithm. Referring back to the equations in Section 2.2.2, if directly substituting Eq. 2.3 and 2.4 into Eq. 2.2, it would give the follow equations:

$$CBF_{0.5} = u_{TR} \otimes HRF_{TR}(t) + u_{SR_{0.5}} \otimes HRF_{SR}(t) \qquad [2.5]$$

$$CBF_{1.0} = u_{TR} \otimes HRF_{TR}(t) + u_{SC_{1.0}} \otimes HRF_{SR}(t) \qquad [2.6]$$

$$CBF_{2.0} = u_{TR} \otimes HRF_{TR}(t) + u_{SR_{2.0}} \otimes HRF_{SR}(t) \qquad [2.7]$$

$$CBF_{3.0} = u_{TR} \otimes HRF_{TR}(t) + u_{SR_{3.0}} \otimes HRF_{SR}(t) \qquad [2.8]$$

We first solved HRF$_{SR}$ by using the differences of neural activities and CBF responses between either two of different stimulus durations (e.g., 1s and 3s stimuli, that is, subtracting Eq. 2.8 to Eq. 2.6). A group of HRF$_{SR}$ was calculated for six combinations of LFPs and CBFs and then to obtain one mean HRF$_{SR}$. Once HRF$_{SR}$ was determined, HRF$_{TR}$ could be estimated from the above four equations Eq. 2.5 to Eq. 2.8.

2.3.7   Model validation

The traditional linearity of the CBF responses was examined by the additivity test, which was commonly used in many previous studies. For example, the CBF 0.5 s response was shifted by 0.5s and added the replica to predict the CBF response to the 1s stimulus. Over-predictions were apparent in most cases, especially seen peak amplitude differences. Besides, we deconvolved each pair of CBF and LFP curves by using a single HRF model for all stimulus paradigms and obtained four different HRFs shown in the figure. The F-test statistic was calculated to assess the significance in the reduction of the sum of squares (SoS) of residuals between the modeled and measured CBFs after adding one component to the traditional one component model, where:

$$F(DoF1 - DoF2, DoF2) = \frac{(SoS1 - SoS2)/SoS2}{(DoF1 - DoF2)/DoF2} \qquad [2.9]$$

The degrees of freedom (DoF) for each model were calculated as the number of time points minus the number of free parameters in the model.

2.4 Results

We first calculated the time-varying SD of the LFP (spectrogram) acquired for different stimulus durations on the single-trial basis and averaged across trials within one recording session. The spectrograms were normalized to the baseline such that the scale indicates the relative increase (or decrease) in power during stimulation. Variations in the LFP recordings from the awake preparations could be seen from the spectrograms from twelve recording sites on one monkey, as shown in Fig. 2.1. For each stimulus condition, a grand mean spectrogram was calculated for all the recordings in one monkey. In Fig. 2.2, all the spectrograms of four different durations of stimuli exhibited a markedly stronger response (~ 2 fold in power) in the frequency range 20 - 125 Hz immediately after the onset of the visual stimulus, consistent with previous LFP measurements [3; 26]. Additionally, a significant stimulus-locked decrease at lower frequencies (5 to 20Hz) was observed in our normalized spectrograms, previously demonstrated on conscious humans as well [26].
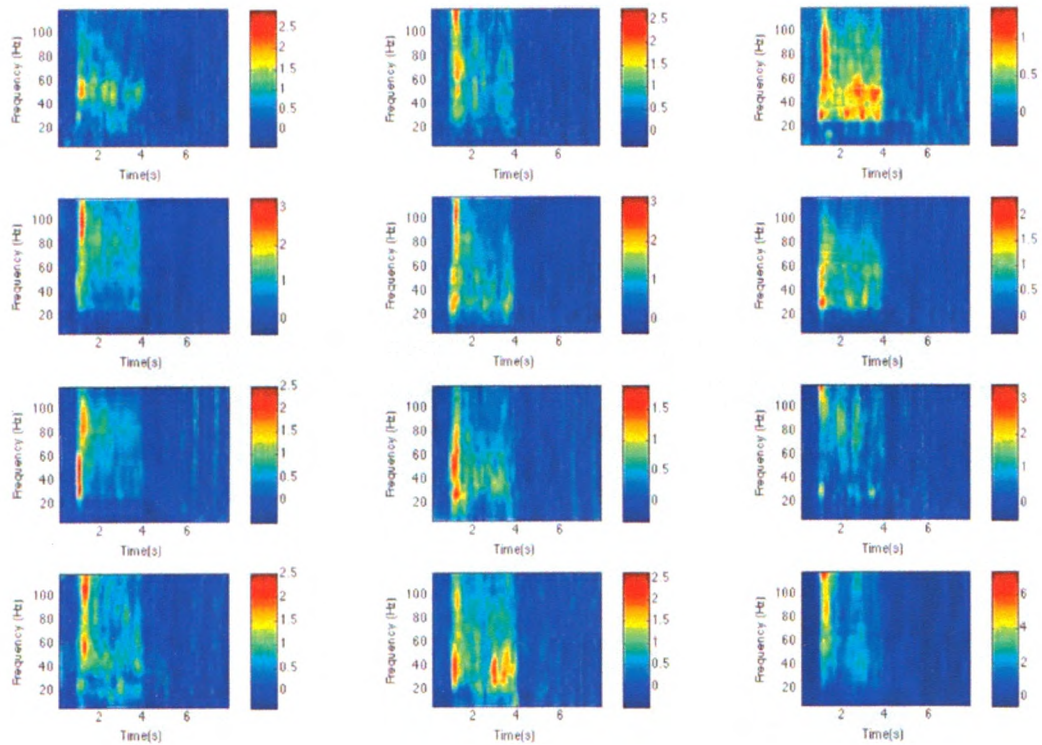
Figure 2.1 The LFP spectrograms were obtained from twelve recording sites on the same animal. The stimulus started after the first second baseline and lasted for 3.0 s. Each LFP spectrogram from one recording site was normalized to its baseline and averaged across trials. Color bar represents relative changes in the LFP power compared to the baseline period.
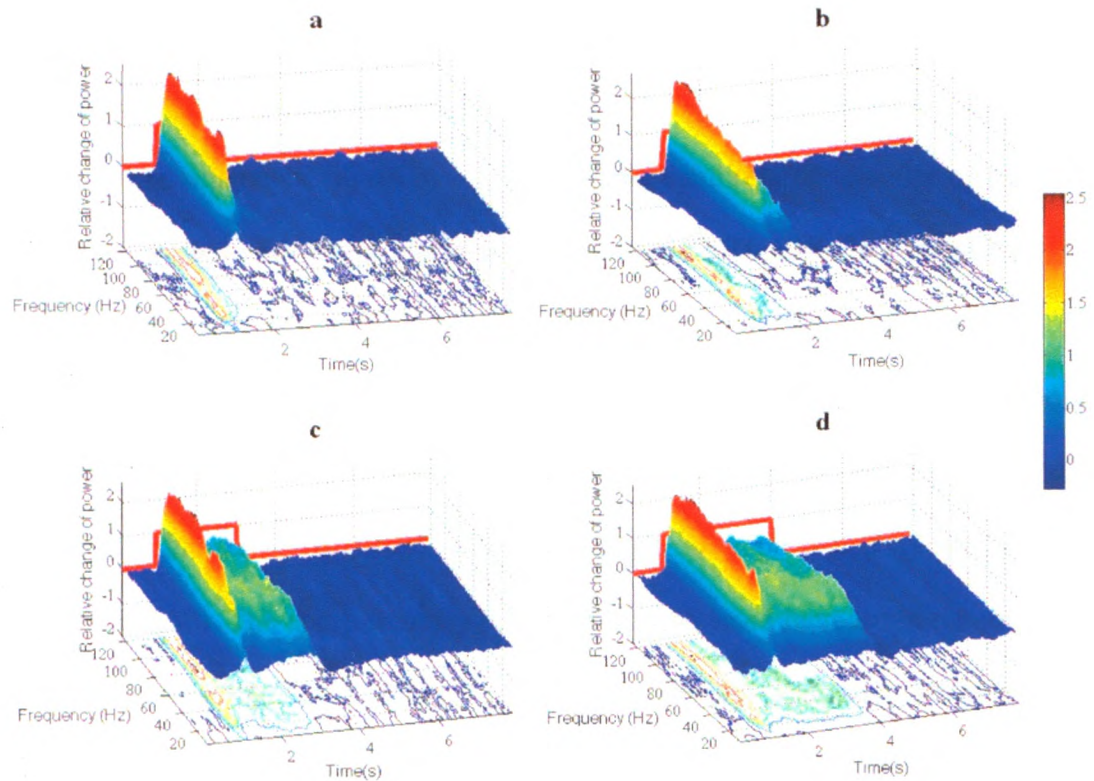
Figure 2.2 Example LFP spectrograms for data collected over 0.5, 1.0, 2.0, 3.0 s stimulus presentations (**a-d**). In each three-dimensional plot, the vertical panel along the time axis shows the time course of the visual stimulus. The bottom panel presents the contour map of the spectrogram.

The LFP power as a function of time was obtained by summing the energy at all frequencies at each time point in the normalized spectrogram (Fig. 2.3a). For the purposes of discussion, we separated the LFP into an initial response (IR) component

(i.e., phasic response) and a sustained response (SR) component (i.e., tonic response) (Fig. 2.3a). This separation was made on the basis that the LFP response to a 0.5 s or shorter stimulus (LFP_{IR} as exemplified by $LFP_{0.5}$) did not exhibit the reduced plateau of sustained gamma band activity that longer stimulus durations evoked (Fig. 2.2). While there is a slight bias in the IR towards higher frequencies, Fig. 2.2 also clearly demonstrates that the highest power in the SR is in the 20 - 70Hz band, which has been attributed to the superficial layers of V1[27]. A gamma band related vascular response has also been associated with these interneuron rich layers[24]. This lower gamma band bias during the steady state is consistent with a recent report in anesthetized monkeys[28]. The IR power is nearly two times the SR power ($P < 0.01$, Mann-Whitney U test) and the ratio of the peak power of IR to the SR is the same regardless of subsequent stimulus duration. Simultaneously recorded MUA responses also presented typical biphasic patterns (Fig. 2.3b). The approximately four fold IR associated increase in the number of spikes per second in the MUA (range 16-32/s during baseline and range 64-128/s during stimulation) and its long duration decay is similar to what has been observed previously [2; 3; 24]. Roughly speaking, all these techniques report averages over approximately 1 mm^3 of cortex for each recorded position that we know to be within the retinotopic boundaries of the stimulus. In primates, this volume contains of the order of 40,000 neurons and 7 x 10^8 synapses, although only a small fraction of these will be recruited for this task [29-31].
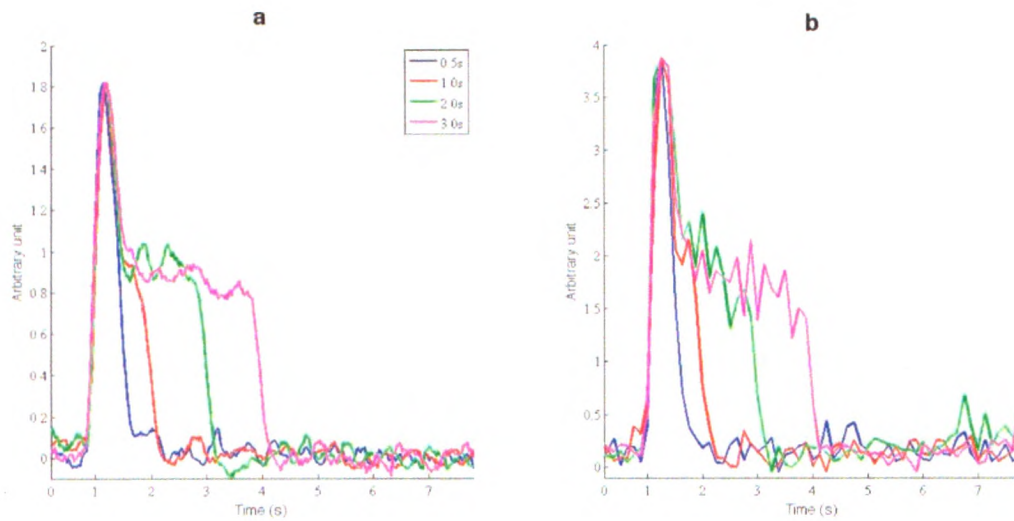
Figure 2.3 **a**, The relative LFP responses are quantified by summing modulated power over all the frequency of Fig.2.2. **b**, Peri-stimulus time histograms calculated from the normalized spike rates were averaged over 10 recording sites. The stimulus condition is represented by color.
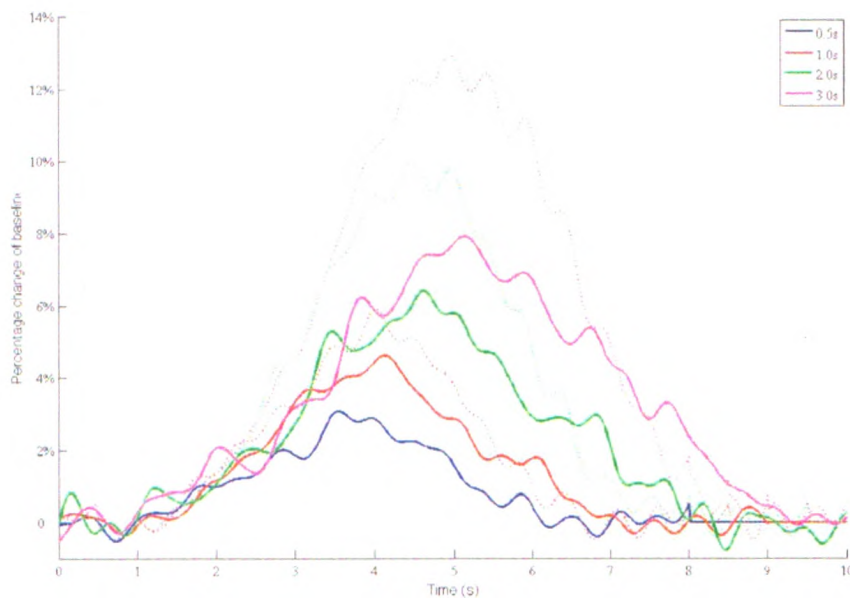
Figure 2.4 The blood flow responses to all stimulus conditions are represented as percentage change of baseline activity. The dotted curves represent the predicted CBF changes by using the shifted and summed replicas of the 0.5 s CBF response.

Relative changes in CBF were also recorded with using the same stimulus paradigm (Fig. 2.4). Shifted and summed replicas of the CBF response to a short stimulus would normally be used to predict the CBF response to a longer stimulus. However, the use of $CBF_{0.5}$ produced significant over-estimations of blood flow for all other stimulus durations (R^2 (1 s) = 0.82; R^2 (2 s) = 0.28; R^2 (3 s) = 0.01, shown in Fig. 2.4), which is in accord with prior findings for CBF measurements [13;32] as well as fMRI data [4;6;7]. This is not surprising, since implicit in this approach is the fact that the NA is the same at all time points, which it clearly is not (Fig. 2.3).

A more rigorous approach is to remove the influence of the time varying NA by deconvolution of the CBF data using the measured LFP in order to extract a HRF. The amplitude and temporal mismatch between the predicted CBF and measured CBF were not revealed without resorting to deconvolution, and this provides the first evidence that HRF_{IR} contains a faster responding flow component than the flow mechanism that supports the SR. Firstly we deconvolved each pair of neural and associated hemodynamic responses to obtain four HRFs. And we found that any single HRF in Fig. 2.5 could not produce satisfactory results of predicting CBF responses under other three conditions. For example, a HRF_{IR} was obtained by deconvolving the IR data ($CBF_{0.5}$, $LFP_{0.5}$). By using this HRF_{IR}, the overestimate of the predicted to measured CBF_1, CBF_2 and CBF_3 using HRF_{IR} was 13.8%, 30.1% and 31.2% respectively (Fig. 2.6a). Thus, even accounting for the shape of the LFP, the CBF-NA coupling appears to be nonlinear with stimulus duration. In addition to overestimating the height of the CBF response, the predicted CBF curves all rise before the measured CBF curves and tend to fall before the actual blood flow does.
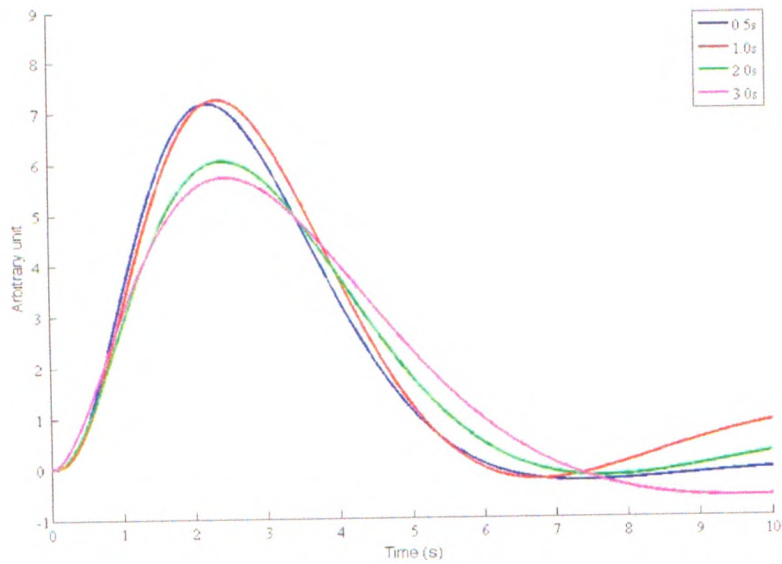
Figure 2.5 The HRFs of each stimulus condition were estimated by the conventional linear transform model. It hints the existence of two components.
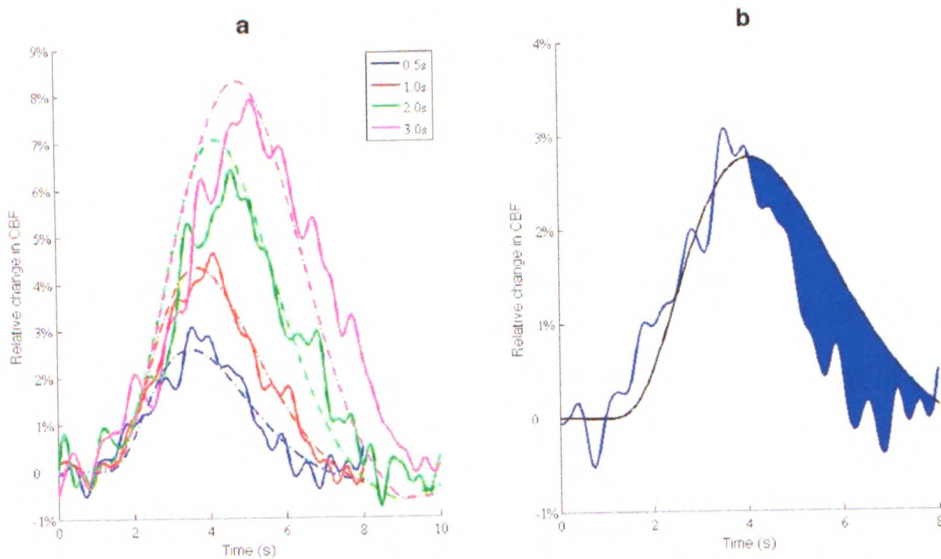
Figure 2.6 **a**, CBF responses to longer stimuli (1.0, 2.0, 3.0s) were estimated by their LFPs and HRF_{IR} (dash curves). **b**, Comparison between the measured 0.5s flow response and predicted from HRF_{SR}. The shaded area demonstrates their mismatch.

Given this time-invariant linear relationship between CBF and NA in the steady state, as well as good predictive power in fMRI at longer stimulus durations (e.g. a 3 s stimulus will predict a 6, 12 or 24 s stimulus [4]), it seemed imprudent to reject linear coupling during the IR in the absence of biological mechanisms to the contrary. Perhaps HRF_{IR} and HRF_{SR} differ by just the strength of the neurovascular coupling? To examine this possibility, we convolved HRF_{SR} (the HRF of the SR component in LFP, the computation procedure described as below) with $LFP_{0.5}$. Comparing the CBF predicted in this manner to the measured $CBF_{0.5}$ (Fig. 2.6b) demonstrates a dramatic overestimation of the duration of the response. This prediction error results in a 29.2 % overestimate of the area of the predicted to the measured $CBF_{0.5}$. This mismatch cannot be accounted for by a difference in the strength of the neurovascular coupling (scale factor) as the curves do not align. We are left with two contradictory findings. HRF_{SR} convolved with $LFP_{0.5}$ overestimates the measured $CBF_{0.5}$ and HRF_{IR} convolved with $LFP_{1,2,3}$ overestimates the measured $CBF_{1,2,3}$ (Fig. 2.6a-b). These apparently paradoxical observations can be rationalized if one invokes a second neurovascular coupling mechanism.

We then characterized these two distinct flow mechanisms one by one. We first verified that the CBF response was predictable for any point along the SR of the LFP, in so far as this represents a steady state for both quantities. By subtracting any two pairs of LFP and CBF responses, we could eliminate the IR due to its constancy. This allowed calculation of the HRF of the SR (HRF_{SR}). Using the deconvolution of the resulting CBF and LFP curves we determined HRF_{SR} for all 6 possible pair-wise subtractions for each animal (Fig. 2.7). Our data show that a single HRF (i.e., HRF_{SR}) can accurately predict
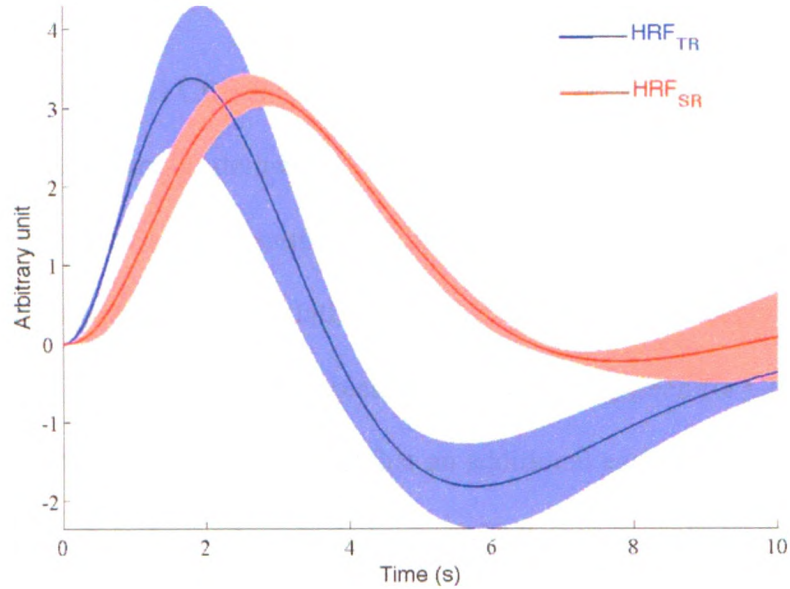
Figure 2.7 Two distinctive HRFs (HRF$_{TR}$, HRF$_{SR}$) are shown respectively for TR and SR of neural responses in our stimulus paradigms. Shaded regions indicate ± s.d.
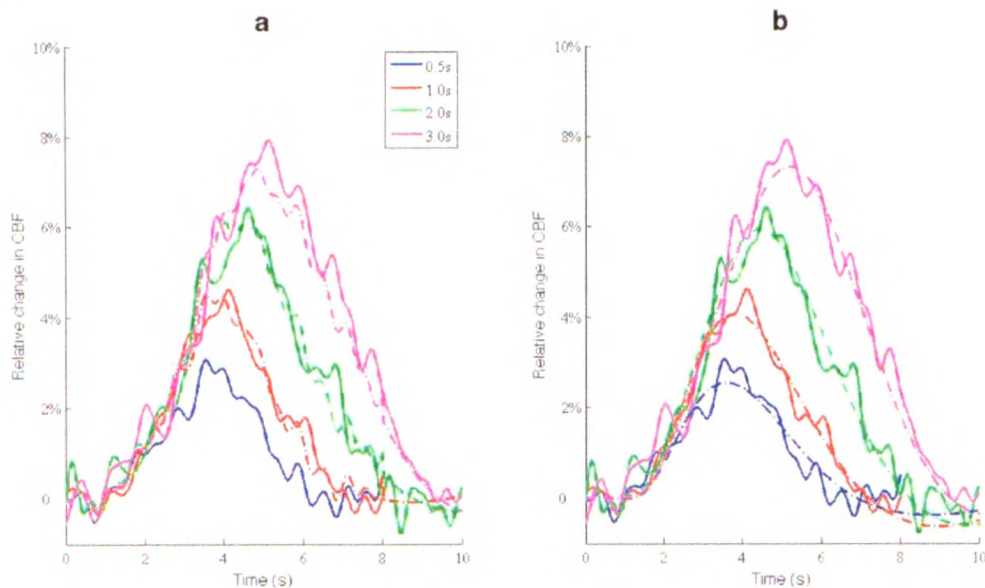
Figure 2.8 **a**, the measured CBF responses to 1.0, 2.0, 3.0 s stimuli (solid) were compared to the predicted CBF responses from the actual CBF$_{0.5}$ and HRF$_{SR}$ (dash). **b**, the comparison was made to the two-component convolution model. The stimulus condition is represented by color.

the CBF response to the SR of the LFP at any point from 0.5 s to 3 s ($R^2 > 0.96$) (Fig. 2.8a).

Evidence for a second CBF regulation mechanism under optimized stimulation (and consequently high metabolic demand) does exist both in somatosensory cortex and V1. For example, Fig. 5 of Ref. 3 demonstrates that as the stimulus contrast increases, the IR of the LFP increases dramatically relative to the SR, and commensurately the time rate of change of the BOLD signal almost doubles. A similar effect is seen for CBF and MUA [24]. Both of these observations in V1 suggest that an additional early flow mechanism comes into play for large NA demands, which are invariably transient. In both the visual and somatosensory systems, when the stimulus is not optimized for driving an area of cortex, the TR of the LFP (and MUA and spikes) decreases or disappears, and the SR (also lowered) dominates [3]. Therefore, we explore a model in which the IR is separable, with the metabolic needs of the SR supported by HRF_{SR} and the transient demands that sit on top of the SR supported by an additional hemodynamic response, HRF_{TR}. By extrapolating the SR of the LFP to time zero and convolving it with HRF_{SR}, we were able to predict the CBF associated with the SR. The residual between the measured CBF and the predicted SR component of the CBF was used in conjunction with the TR of the LFP to deconvolve the impulse response for the TR and obtain HRF_{TR} (Fig. 2.7). Convolving these HRFs with the appropriate TR and SR components of the LFPs produced the predicted curves in Fig. 2.8b (R^2 (0.5 s) = 0.91; R^2 (1 s) = 0.96; R^2 (2 s) = 0.95; R^2 (3 s) = 0.95). In all cases, the two-component model we proposed produced highly significant reduction in the unexplained variance when compared to the traditional linear model

$$(\quad F_{0.5s} = 105.01, p \ll 10^{-16} \quad ; \quad F_{1.0s} = 50.03, p \ll 10^{-16} \quad ; \quad F_{2.0s} = 76.88, p \ll 10^{-16} \quad ;$$

$$F_{3.0s} = 134.07, p \ll 10^{-16}).$$

2.5 Discussion

We proposed a two-component linear model to describe the temporal dynamics of the neurovascular relationship as manifested by our experimental data in the primary visual cortex of awake macaques. The present model may offer a straightforward explanation to the mystery that the shorter visual stimulation (less than 3 or 4s) has nonlinear response but longer stimulation behaves more linearly [3; 4; 15]. With longer duration of the stimulus, an increase in blood flow caused by the SR would take a larger proportion in the total changes of CBF so that a conventional linear transform model could explain more variances during modeling procedures (Fig. 2.3a and 2.3b). Recent studies suggested that hemodynamic response is a spatiotemporal convolution of the neuronal activation in rat barrel columns and some inconsistent results of the neurovascular relationship could be caused by the spatial extent of neuronal activation [33]. Our results further supported their findings in view of time domain and suggested that the nonlinearity of the system might be introduced by the complex spatial integration of the hemodynamic responses in individual sufficiently-refined brain structures. Recall the TR and SR of neural response to one single visual stimulus, it was evident that the resulting hemodyamic responses to one single external sensory input to the brain possibly have different contribution sources in time and spatial domains (Fig. 2.4-2.6). The spatial integration process in our model is consistent with the characteristics of functional architectures well established in V1 and

indicates that the distinct underlying mechanisms are more likely involved to regulate localized microcirculation in order to accomplish the specialized function purposes.

What could the physiological origin of HRF_{TR} and HRF_{SR} be? Primate V1 has long been recognized as a structure with six functionally distinct input, output and processing layers that are superimposed upon a vascular bed that also has multiple layers [34]. The functional significance of this intriguing configuration of microvasculature in striate cortex is unknown, but is likely related to recent findings that blood flow can be regulated at the level of the cortical laminae [35], single capillaries [36], astrocytes modulating arterioles [37;38] and vascular endothelial cells [11]. Many of these regulatory mechanisms allow dilation or constriction of vessels [39]. We propose that HRF_{SR} is the normal CBF response mode in V1, capable of supporting the sustained energy demands that even a doubling of LFP power requires in cortex. In regions where the larger, invariably transient metabolic increases in NA occur, HRF_{TR} can provide faster additional flow capacity for brief periods and take it away just as quickly when the demand is removed. Given that energy consumption likely constrains neural processing [31;40;41], it may not be surprising that the brain has evolved vascular mechanisms to deal with the metabolic demands of both high levels of transient neural activity and lower levels of sustained neural activity. Our findings have significant implications in the analysis of event related fMRI paradigms, particularly for sensorimotor systems. They also suggest that the onset time for CBF and BOLD signals depends on the metabolic demand of the active neurons and this needs to be considered in rapid event related designs and chronometric studies.

2.6 Conclusion

In summary, the present model not only integrated existing views of modeling the complex relationship between neural activity and blood flow responses, but also indicated the brain is capable of regulating the blood traffic in a parallel way to ensure adequate energy available for different functional operations. These metabolic underpinnings of brain function have great implications for relating hemodynamic-based like BOLD fMRI results as established answers to more sophisticated neuroscientific inquiry.

2.7 Reference

1.   Buxton RB, Uludag K, Dubowitz DJ, Liu TT. Modeling the hemodynamic response to brain activation. Neuroimage, 2004; 23 Suppl 1: S220-233.

2.   Logothetis NK. The underpinnings of the BOLD functional magnetic resonance imaging signal. J Neurosci, 2003; 23: 3963-3971.

3.   Logothetis NK, Pauls J, Augath M, Trinath T, Oeltermann A. Neurophysiological investigation of the basis of the fMRI signal. Nature, 2001; 412: 150-157.

4.   Boynton GM, Engel SA, Glover GH, Heeger DJ. Linear systems analysis of functional magnetic resonance imaging in human V1. J Neurosci, 1996; 16: 4207-4221.

5.   Friston KJ, Frith CD, Turner R, Frackowiak RS. Characterizing evoked hemodynamics with fMRI. Neuroimage, 1995; 2: 157-165.

6.   Friston KJ, Josephs O, Rees G, Turner R. Nonlinear event-related responses in fMRI. Magn Reson Med, 1998; 39: 41-52.

7.   Glover GH. Deconvolution of impulse response in event-related BOLD fMRI. Neuroimage, 1999; 9: 416-429.

8.   Heeger DJ, Ress D. What does fMRI tell us about neuronal activity? Nat Rev Neurosci, 2002; 3: 142-151.

9.   Ogawa S, Menon RS, Tank DW, Kim SG, Merkle H, Ellermann JM, Ugurbil K. Functional brain mapping by blood oxygenation level-dependent contrast magnetic resonance imaging. A comparison of signal characteristics with a biophysical model. Biophys J, 1993; 64: 803-812.

10.   Roy CS, Sherrington CS. On the regulation of the blood-supply of the brain. J Physiol, 1890; 11: 85-158 117.

11.   Iadecola C. Neurovascular regulation in the normal brain and in Alzheimer's disease. Nat Rev Neurosci, 2004; 5: 347-360.

12.   Hewson-Stoate N, Jones M, Martindale J, Berwick J, Mayhew J. Further nonlinearities in neurovascular coupling in rodent barrel cortex. Neuroimage, 2005; 24: 565-574.

13.   Miller KL, Luh WM, Liu TT, Martinez A, Obata T, Wong EC, Frank LR, Buxton RB. Nonlinear temporal dynamics of the cerebral blood flow response. Hum Brain Mapp, 2001; 13: 1-12.

14.   Oppenheim AV, Willsky AS, Nawab SH. Signals and systems, 2nd ed. Prentice Hall, 1996.

15.   Vazquez AL, Noll DC. Nonlinear aspects of the BOLD response in functional MRI. Neuroimage, 1998; 7: 108-118.

16.   Chen LM, Heider B, Williams GV, Healy FL, Ramsden BM, Roe AW. A chamber and artificial dura method for long-term optical imaging in the monkey. J Neurosci Methods, 2002; 113: 41-49.

17.   Fox PT, Raichle ME. Stimulus rate determines regional brain blood flow in striate cortex. Ann Neurol, 1985; 17: 303-305.

18.   Chen LM, Friedman RM, Roe AW. Optical imaging of SI topography in anesthetized and awake squirrel monkeys. J Neurosci, 2005; 25: 7648-7659.

19.   Grinvald A, Frostig RD, Siegel RM, Bartfeld E. High-resolution optical imaging of functional brain architecture in the awake monkey. Proc Natl Acad Sci U S A, 1991; 88: 11559-11563.

20.   Vnek N, Ramsden BM, Hung CP, Goldman-Rakic PS, Roe AW. Optical imaging of functional domains in the cortex of the awake and behaving monkey. Proc Natl Acad Sci U S A, 1999; 96: 4057-4060.

21.   Detre JA, Ances BM, Takahashi K, Greenberg JH. Signal averaged laser Doppler measurements of activation-flow coupling in the rat forepaw somatosensory cortex. Brain Res, 1998; 796: 91-98.

22.   Mitra PP, Pesaran B. Analysis of dynamic brain imaging data. Biophys J, 1999; 76: 691-708.

23.   Pesaran B, Pezaris JS, Sahani M, Mitra PP, Andersen RA. Temporal structure in neuronal activity during working memory in macaque parietal cortex. Nat Neurosci, 2002; 5: 805-811.

24.   Niessing J, Ebisch B, Schmidt KE, Niessing M, Singer W, Galuske RA. Hemodynamic signals correlate tightly with synchronized gamma oscillations. Science, 2005; 309: 948-951.

25.   Press WH, Teukolsky SA, Vetterling WT, Flannery BP. Numerical recipes in C: the art of scientific computing, 2nd ed. Cambridge University Press: Cambridge, 1993.

26.   Mukamel R, Gelbard H, Arieli A, Hasson U, Fried I, Malach R. Coupling between neuronal firing, field potentials, and FMRI in human auditory cortex. Science, 2005; 309: 951-954.

27.   Gray CM, McCormick DA. Chattering cells: superficial pyramidal neurons contributing to the generation of synchronous oscillations in the visual cortex. Science, 1996; 274: 109-113.

28.   Henrie JA, Shapley R. LFP power spectra in V1 cortex: the graded effect of stimulus contrast. J Neurophysiol, 2005; 94: 479-490.

29.   Juergens E, Guettler A, Eckhorn R. Visual stimulation elicits locked and induced gamma oscillations in monkey intracortical- and EEG-potentials, but not in human EEG. Exp Brain Res, 1999; 129: 247-259.

30.   Jakobsson A, Nilsson GE. Prediction of sampling depth and photon pathlength in laser Doppler flowmetry. Med Biol Eng Comput, 1993; 31: 301-307.

31.   Lennie P. The cost of cortical computation. Curr Biol, 2003; 13: 493-497.

32.   Martindale J, Berwick J, Martin C, Kong Y, Zheng Y, Mayhew J. Long duration stimuli and nonlinearities in the neural-haemodynamic coupling. J Cereb Blood Flow Metab, 2005; 25: 651-661.

33.   Devor A, Ulbert I, Dunn AK, Narayanan SN, Jones SR, Andermann ML, Boas DA, Dale AM. Coupling of the cortical hemodynamic response to cortical and thalamic neuronal activity. Proc Natl Acad Sci U S A, 2005; 102: 3822-3827.

34.   Zheng D, LaMantia AS, Purves D. Specialized vascularization of the primate visual cortex. J Neurosci, 1991; 11: 2622-2629.

35.   Caesar K, Thomsen K, Lauritzen M. Dissociation of spikes, synaptic activity, and activity-dependent increments in rat cerebellar blood flow by tonic synaptic inhibition. Proc Natl Acad Sci U S A, 2003; 100: 16000-16005.

36.   Peppiatt CM, Howarth C, Mobbs P, Attwell D. Bidirectional control of CNS capillary diameter by pericytes. Nature, 2006; 443: 700-704.

37.   Mulligan SJ, MacVicar BA. Calcium transients in astrocyte endfeet cause cerebrovascular constrictions. Nature, 2004; 431: 195-199.

38.   Zonta M, Angulo MC, Gobbo S, Rosengarten B, Hossmann KA, Pozzan T, Carmignoto G. Neuron-to-astrocyte signaling is central to the dynamic control of brain microcirculation. Nat Neurosci, 2003; 6: 43-50.

39.   Metea MR, Newman EA. Glial cells dilate and constrict blood vessels: a mechanism of neurovascular coupling. J Neurosci, 2006; 26: 2862-2870.

40.   Laughlin SB, Sejnowski TJ. Communication in neuronal networks. Science, 2003; 301: 1870-1874.

41.   Ureshi M, Matsuura T, Kanno I. Stimulus frequency dependence of the linear relationship between local cerebral blood flow and field potential evoked by activation of rat somatosensory cortex. Neurosci Res, 2004; 48: 147-153.

Chapter 3   Imaging cerebral blood flow with laser speckle[2]

As suggested in one recent study [1], a single-point hemodynamic measure could be a measure of complex spatial integration of electrophysiological activity over a given location. By performing the mathematical analysis of linear convolution model in Chapter 2, we demonstrate that two phases of neuronal responses is involved in single kind of visual stimulus and each of them imposes their own physiological influence on the cerebral microcirculation. To spatially pinpoint distinct hemodynamic responses evoked by different neuronal activities, one has to rely on an in vivo imaging technique that can directly visualize variations of blood flow with sufficient spatial and temporal resolution.

The work of this chapter was designed to map changes in cerebral blood flow (CBF) at a submillimeter spatial scale by using Laser Speckle Contrast Imaging (LSCI)

---

[2] A modified version of this chapter was previously published. Wang Z, Hughes S, Dayasundara S, Menon RS. *Theoretical and experimental optimization of laser speckle contrast imaging for high specificity to assess brain microcirculation.* J Cereb Blood Flow & Metab, 2007, 27:258-269. Copyright © (2007 Nature Publishing Group). Reprinted by permission of Nature Publishing Group

technique. Recently this "old" method has attracted an increasing interest in studies of brain activities under normal and pathophysiologic conditions. But some paramount assumptions behind this imaging technique have been kept ignored in this field since 1981 firstly proposed by Fercher and Briers. Most recently, these assumptions were claimed as serious mistakes that made LSCI fail to reproducibly and correctly measure blood flow speed. In this study these issues were re-examined on a theoretical basis. Since imaging the blood flow with resolution at submillimeter level was expected, it was technical challenging to perform such high-resolution imaging on the awake, behaving animals, such as strict control of head and body movement. We then switched to the isoflurane-anaesthetized animals to experimentally validate our theoretical analysis. Further, we resorted to the classic carbon dioxide challenge model so as to demonstrate how the parameters of LSCI can be optimized to measure flow dynamics in capillaries. In our experiments, the detailed distribution of CBF responses to the stimulation induced by different levels of carbon dioxide pressure was obtained with tens of micron spatial resolution. The relative CBF images over the exposed cortical area acquired by LSCI were also compared with laser-doppler measurements. Our results confirmed that these assumptions would not produce any significant errors on investigating changes of blood flow and optimization of LSCI could achieve high specificity to assess cerebral microcirculation, as would facilitate its broad application in functional imaging field.

3.1 Introduction

It has long been recognized that local changes in cerebral blood flow (CBF) reflect the spatial and temporal dynamics of neural activity in an intimate but complicated way [2].

This so-called functional hyperemia (increased blood flow due to neural activity) is the physiological response underlying many modern hemodynamic based neuroimaging techniques including positron-emission tomography (PET)[3], functional MRI (fMRI)[4], optical imaging of intrinsic signals (OIS) [5] and LSCI [6]. With the last three methods, the physical spatial resolution of the detection system per se does not necessarily limit the functional spatial resolution. It is the spatial specificity of the coupling between the neuronal activity and the hemodynamic response that determines whether, for example, columnar or layer specific activity can be imaged in vivo [7; 8]. Even if the vascular response is highly localized, the actual sensitivity and specificity achieved by a particular functional imaging technique depends on the interaction between the physics of the data acquisition and the physiology being probed. Functional spatial resolution limits for fMRI and OIS have been extensively studied both experimentally and theoretically, and depend on the exact methods being used to acquire the images[9]. However, no formal work has been done to explore the determinants of high functional spatial resolution for LSCI.

LSCI has recently been demonstrated as a promising approach to investigate CBF responses in the brain under normal functional [10-12] and pathophysiologic conditions [6; 13-15]. Since it does not require laser scanning, it can offer far better spatiotemporal resolution than most techniques currently used in blood flow measurements [6]. For example, flow-sensitive MRI techniques detect changes in CBF with a temporal resolution of the order of the lifetime of the labeled water (1-2 s depending on magnetic fields) [16]. The temporal resolution of conventional confocal and two-photon imaging is slowed by the scanning of multiple points to build up an image with excellent spatial resolution[17]. The LSCI

approach exploits the intrinsic flow information mainly from red blood cells that is encoded into the reflected speckle pattern and thus avoids the potential fluorescence-induced damage or photobleaching effects that the laser scanning methods can have. Finally, it is also worth mentioning that a LSCI system is considerably easier and cheaper to construct compared to a confocal or two-photon imaging system.

Although the theory of LSCI (also called Laser Speckle Contrast Analysis, LASCA or Laser Speckle Flowmetry, LSF) was proposed firstly by Fercher and Briers in 1981, the theoretical details of this imaging technique have rarely been discussed systematically and consequently some important assumptions related to vascular specificity and quantification have been ignored for two decades [18-22]. In particular, Bandyopadhyay and his colleagues [23] have claimed that two of the implicit assumptions made over the past quarter century cast doubt on the interpretation of results obtained by LSCI using the 1981 theory. This includes virtually all biologically relevant LSCI measurements. Consequently they introduced a new framework for LSCI interpretation.

In our current work, we show both by theoretical analysis based on the original speckle theory of Goodman [24], and our own experimental evidence, that the framework of Fercher and Briers is in fact valid for the conditions of LSCI in biological systems with current hardware. With the insight that we gain from the theory, an appropriate strategy is also proposed to gain high specificity to brain microcirculation. Sensitivity to microcirculation is a necessary condition for high functional spatial resolution studies of brain activity. Images of changes in tissue and pial vessel blood flow under the effect of changes in $PaCO_2$ were acquired at tens of microns per pixel in isoflurane-anesthetized rats through a cranial window. Since CO_2 challenge experiments have been well

established as a classic model for investigating CBF [25; 26], the results from LSCI allow us to show spatially-resolved CBF responses that agree with point source Laser Doppler Flowmetry (LDF) measurements made at the same points in the images.

3.2 Theory

3.2.1 Definition of speckle contrast

The basics of speckle theory have been thoroughly described by Goodman [24; 27-29] and only relevant vital parameters and concepts are included here. We start from the speckle contrast defined by the ratio of the standard deviation to the mean of a speckle pattern, $C = \sigma_I / \bar{I}$. From Goodman's results on mean and variance of integrated intensity (1985), the first moment $\bar{I_T}$ and variance $\sigma_{I_T}^2$ of the integrated intensity I_T measured within a finite-time integral interval, T, are given by:

$$\bar{I_T} = \int_{-T/2}^{-T/2} \bar{I} d\xi = \bar{I} \cdot T \qquad [3.1]$$

$$\sigma_{I_T}^2 = T \int \int_{-\infty}^{\infty} (1 - \frac{|\tau|}{T}) \Gamma_I(\tau) d\tau - (\bar{I_T})^2 \qquad [3.2]$$

where $\bar{I}$ is the mean intensity of the speckle pattern, the function $(1 - \frac{|\tau|}{T})$ is the deterministic autocorrelation function of the integration window, and the function Γ_I is the statistical autocorrelation function of the instantaneous intensity. Within a speckle pattern, many independent scattered wavefields contribute to the random walk that generates speckle such that the summed intensity varies from intensely bright to completely dark when constructive or destructive inference dominates the sum [27]. Since

the measured speckle data (recorded by the detector) is in terms of intensity, Siegert's relation [30] can be applied for fully developed speckle if a circular complex Gaussian random process is used as an underlying model. This relation conveniently relates the autocorrelation of the electric field to the autocovariance function of the speckle intensity pattern as follows [27; 30]:

$$\Gamma_I(\tau) = (\bar{I})^2 [1 + |\mu_A(\tau)|^2] \qquad [3.3]$$

where $\mu_A(\tau)$ is the normalized spatial autocovariance of the temporal fluctuations in the intensity of a *single* speckle. According to Goodman's theory (1975), the intensity statistics for coherent light illuminating a rough surface is predicted by the gamma probability density function $p(I)$:

$$p(I) = \frac{(\frac{M}{\bar{I}})^M I^{M-1} \exp(-M\frac{I}{\bar{I}})}{\Gamma(M)} \qquad \text{for } I \geq 0 \qquad [3.4]$$

where M is a shaping constant, $\Gamma(M)$ is the gamma function. For the special case of $M = 1.0$, $p(I)$ reduces to a negative exponential, a characteristic signature of fully developed (or far-field) speckle. Therefore, $p(I)$ obtained from our experimental data was examined to assess the validity of the fully developed speckle assumption normally used to quantitate LSCI.

Substituting Eq. 3.3 into Eq. 3.2, the definition of speckle contrast can be written as:

$$C = \frac{\sigma_{I_T}(T)}{\bar{I}(T)} = \sqrt{\frac{2}{T} \int_0^T (1 - \frac{\tau}{T}) |\mu_A(\tau)|^2 d\tau} \qquad [3.5]$$

With a small change of the functional form, we can compare with the more traditional expression of the speckle contrast used by Fercher and Briers (see Equation 8 in there):

$$C = \sqrt{\frac{1}{T} \int_0^T |\mu_A(\tau)|^2 \, d\tau} \qquad [3.6]$$

It's readily apparent that the difference between Eq. 3.5 and Eq. 3.6 lies in the integral interval (resulting in a factor of 2 discrepancy) and the function $(1 - \frac{\tau}{T})$. Generally, researchers have made a tacit assumption that $1 - \frac{\tau}{T} \approx 1$ when T grows sufficiently large. While the effective exposure time T was slow enough for this to be valid two decades ago, much faster CCD cameras are now available that could make this assumption seriously inappropriate. We also explore the validity of this approximation in our experiments.

3.2.2   Autocovariance function of speckle

Since the fine, high-contrast speckle image is modulated by the movement of scatterers when a rough surface is illuminated with laser light, $\mu_A(\tau)$ is of fundamental importance in relating the statistics of the detected intensity to the velocity of moving cells in tissue. On account of the complexity of biological systems, some reasonable approximations can be initially considered. Based on a simple physical model for in-plane, straight-line and uniform-speed movement, Goodman managed to derive an expression for $\mu_A(\tau)$ as follows:

$$\mu_A(\tau) = \frac{\int\int_{-\infty}^{\infty} [\exp(\sigma^2 e^{-\frac{\Delta x^2 + \Delta y^2}{r_o^2}}) - 1][\exp(\sigma^2 e^{-\frac{(\Delta x - v\tau)^2 + \Delta y^2}{r_o^2}}) - 1] \, d\Delta x \, d\Delta y}{\int\int_{-\infty}^{\infty} [\exp(\sigma^2 e^{-\frac{\Delta x^2 + \Delta y^2}{r_o^2}}) - 1]^2 \, d\Delta x \, d\Delta y} \qquad [3.7]$$

where σ^2 is the variance of the phase process; r_o^2 is the coherent radius; v is the speed of the moving object; and $\Delta x, \Delta y$ are spatial locations [29]. It has been demonstrated by Monte

Carlo simulation that there is a family of phase functions such as the Henyey-Greenstein functions that are well suited to describe single-scattering events in turbid media like tissue [31]. The expression for Henyey and Greenstein scattering phase functions was proposed as follows:

$$f(\theta) = \frac{1}{4\pi} \frac{1 - g^2}{(1 + g^2 - 2g\cos\theta)^{3/2}}$$ [3.8]

Here the anisotropy factor g was set at a value of 0.94 for grey matter in the brain. If the deflection angle θ were assumed to be distributed randomly within the range 0 to π, then we can estimate that the value of σ^2 is $(34\pi)^2$ in grey matter.

Thus a numerical integration of Eq. 3.7 can be performed to get an approximate expression for $\mu_A(\tau)$, as plotted in Fig. 3.1. The negative exponential and Gaussian distributions are both used to fit $\mu_A(\tau)$ and their correlation coefficients are calculated ($R^2 = 0.93, R^2 = 0.99$, respectively). When the variance of phase process increases, $\mu_A(\tau)$ will abruptly converge so that the differences among any specific profile will diminish. Moreover, when the velocity v increases while other parameters remain fixed, the value of $\mu_A(\tau)$ will decrease such that the speckle contrast C reduces too. This inverse relationship between the velocity and speckle contrast is in agreement with the conclusion from Briers [20].

3.2.3 Relationship between speckle contrast and velocity

Having derived an expression for $\mu_A(\tau)$ and hence C by substitution into Eq. 3.5 (an ergodic random process is assumed for the resultant speckle pattern), we can now compare it with simpler forms that have been previously used in the literature. These

simple forms include negative exponential and Gaussian functions that can be substituted

for $\mu_A(\tau)$ in Eq. 3.5, giving rise to

$$C = \frac{\sigma_s}{\langle I \rangle} = [\frac{2}{T}\int_0^T (1-\frac{\tau}{T})\exp(-2\tau/\tau_c)d\tau]^{1/2}$$

$$= [\frac{\tau_c}{T}(1-\exp(-2T/\tau_c)) + \frac{2}{T}(\frac{\tau_c}{4}\frac{(2T\exp(-2T/\tau_c)+\tau_c\exp(-2T/\tau_c)-\tau_c)}{T})]^{1/2} \qquad [3.9a]$$

$$= \left\{\frac{\tau_c}{T}+\frac{1}{2}(\frac{\tau_c}{T})^2[\exp(-2T/\tau_c)-1]\right\}^{1/2}$$

$$C = \frac{\sigma_s}{\langle I \rangle} = \left\{\frac{\tau_c}{T}erf(\sqrt{\pi}\frac{T}{\tau_c}) - \frac{1}{\pi}(\frac{\tau_c}{T})^2[1-e^{-\pi(T/\tau_c)^2}]\right\}^{1/2} \qquad [3.9b]$$

where $erf(x)$ is a standard error function. Plots of Eq. 3.9a and 3.9b, with and without

assumption that $(1-\frac{\tau}{T}) \approx 1$, can be found in Fig. 3.2. In the Discussion, we compare these

simpler forms with the numerically solved expression using Eq. 3.9a and 3.9b.

From Bonner and Nossal's theory [32], this correlation time is inversely related to the

mean translational speed of the moving blood cells. Practically, the integral time T can

be arbitrarily related to the correlation time τ_c. The decay time of photon autocorrelation

functions measured for capillary flow typically are of the order of 0.1~1 ms [32]. As

demonstrated in Fig. 3.2, a small change in the measured values of the speckle contrast in

the experiments actually corresponds to a larger relative-change in blood flow. It implies

that previous studies using LSCI technique could underestimate the relative changes of

blood flow if the assumption $1-\frac{\tau}{T} \approx 1$ is not met. This underestimation has been reported

recently [15] but the authors excluded this as a possibility that could explain the major

discrepancy of the results obtained with LDF and LSCI.

One tends not to think of flow and particle velocities in terms of correlation times τ. Taking advantage of this simple inverse relationship between the correlation time and the mean translational speed of moving particles (mainly erythrocytes) ($\tau_c \propto 1/v$), the mean velocity of the scatterers can be obtained from the numerical solution of τ_c in the above equations. This mean velocity is an absolute number allowing quantitative flow measurements to be made, in principle. The exact relationship between the correlation time and the velocity will depend on the velocity distribution of the scatterers because it also contributes to determine the *shape* of the autocorrelation function. In practice, particles (mainly erythrocytes) move in the blood vessels with a variety of velocities, which depends on the vascular size, geometrical distribution, and is spatially regulated by many kinds of chemical and/or neurogenic factors [33]. Some kind of velocity distribution function is usually used to statistically describe these velocity attributes, such as the Maxwellian velocity distribution proposed by Bonner and Nossal [32]. In term of scalar velocity v, the Maxwellian distribution becomes:

$$P(v) = \left(\frac{2}{\pi}\right)^{1/2} \left(\frac{1}{\langle v^2 \rangle}\right)^{3/2} v^2 \exp(-v^2/2\langle v^2 \rangle)$$
[3.10]

where $\langle v^2 \rangle$ is the second moment of the distribution. In LSCI, the raw speckle image recorded by the CCD camera is converted into the speckle contrast image using a definition of speckle contrast, in which the flow information has been embodied [6]. Therefore, the probability density histogram of the speckle contrast image should reflect the spatial distribution of the velocities within the imaged area. In our study we also examine this velocity distribution based on our data obtained by manipulating CO_2 to change blood flow in the rat brain.

3.3 Materials and Methods

3.3.1 Animal preparation

Both LDF and LSCI were used to monitor blood flow in the exposed cortex of isoflurane-anesthetized rats. This study was approved by the University of Western Ontario's Institutional Animal Care and Use Committee (Appendix B). Male Sprague-Dawley rats (body weight from 275 to 300 g, n = 6) were housed in a 12 hour dark and 12 hour light cycle and fed ad lib. Rats were firstly anesthetized with isoflurane (4% induction, 1-1.5% maintenance) in an induction chamber with ventilated medical grade room air. A tracheotomy tube was inserted and volume ventilation in air/O_2 performed to normocapnia ($PaCO_2$ = 32 ± 1 mmHg). End-expiratory $PaCO_2$ and respiration rate was monitored during the experiments (Nellcor Puritan Bennett Inc., CA, USA). When performing the carbon dioxide challenge ($PaCO_2$ range: 22 to 51 mmHg), the $PaCO_2$ was lowered by hyperventilation and raised by hypoventilation using a dual-mode pressure controlled ventilator (Kent Scientific Corp., CT, USA) [26]. At least 15 minutes was allowed for the establishment of a steady state at hypocarbic and hypercarbic phases. Under anesthesia, femoral arterial and venous catheters were placed for drug administration, continuous recording of mean arterial blood pressure (MABP), and determination of arterial blood gases, pH and blood glucose levels (SpaceLabs Medical Inc., WA, USA). Arterial oxygen saturation was non-invasively monitored by a pulse oximeter (Benson Medical Industries Inc., Canada). During the experiments, body temperature was maintained between 37.0 and 37.5°C by a rectal probe and servo-controlled heat pad (Gaymar Industries Inc., NY, USA). The cranial window was created using small modifications of our previously described method [34]. The anesthetized rats

were then immobilized in a stereotaxic frame. The animal head was shaved and scalp excised in order to expose the skull. The skull on one side (~3 × 3 mm) 1.5 mm anterior to and 1 mm lateral to the bregma was bored with great care to translucency under saline cooling. The thinned skull preparation had the advantage over a full craniotomy since it kept the dura mater intact and allowed a long-term investigation into the changes in the exposed area of cortex within a single animal while preserving the integrity of the brain surface environment. Despite this, bone translucency during prolonged experiments would change. Therefore, several drops of mineral oil were applied to form a thin film on it to prevent drying and improve the image quality. With our system design we carried out sequential LSCI-LDF measurements on different trials. A fine needle laser-doppler probe (450μm diameter, Oxford Optronix, UK) held by a micromanipulator was positioned over the selected small imaging region-of-interest (ROI) in an area devoid of large vessels in the exposed cortex. Microvascular blood perfusion in the rat brain tissue was monitored with an OxyLab Laser Doppler Microvascular Perfusion Monitor (Oxford Optronix) and the data was recorded by PowerLab system (ADInstruments Inc., Toronto, Canada) and stored on a computer for offline analysis. Throughout the entire study animals always remained intubated and ventilated, and were sacrificed with an overdose of sodium pentobarbital upon completion. High quality anatomical images of each subject were collected as reference when the exposed cortex was evenly illuminated using green light ($\lambda = 540 \pm 10nm$) via two fiber-optic light guides attached with two collimating lenses (Oriel instruments, Newport, CT, USA).

3.3.2 LSCI system

The LSCI instrument described here is similar to that developed by other groups [6], with additional modifications for higher performance. The laser beam from a laser diode (Hitachi, 785nm, 50mW, Thorlabs, Newton, NJ, USA) was coupled by two collimating lenses into a 600-μm diameter optical fiber (2 m length). The output beam from the fiber was collimated by the third collimating lens (f = 8 mm), and adjusted to provide uniform illumination on the surface of the exposed brain tissue (~ 8 mm diameter). Although a long multimode optical fiber could potentially suppress the speckle signal, it has been demonstrated recently that intermodal dispersion was not a critical factor in signal generation by interference under conditions like ours [35]. During the experiments, the temperature of the laser diode was maintained at 25°C (temperature stability: <0.002°C) by a precise controller (TED200, Thorlabs). Images were captured by a 16-bit, thermoelectrically-cooled CCD camera (PIXIS, Princeton Instruments, NJ, USA) and transferred to a computer by imaging software (WinView/32, Princeton Instruments). A tandem macroscope (Redshirtimaging LLC, CT, USA), which could provide variable numerical aperture (NA, 0.06~0.4) for low magnification (0.75~5 X) and long working distance (1.0~4.0 cm) and large field-of-view (FOV), was coupled with the CCD camera to focus the images and adjust the speckle size. One vital factor in LSCI is the determination of speckle size, which could affect the final spatial resolution of LSCI. In imaging speckle geometry, the speckle size in the imaging plane should match the size of detector elements (13×13 μm here) to avoid the spatial averaging that would suppress the speckle pattern and destroy the speckle contrast. Like previous studies, the size of the speckle observed in the image plane was approximately calculated by $d = 2.44\lambda Mf$. Here λ is the illumination wavelength, M is the magnification of the macroscope system, and f

is the f-number of the camera lens. In this study, f is approximately 9.4 at a wavelength of 785 nm. The CCD camera with the macroscope lenses was mounted on our custom-designed platform and positioned vertically to obtain the whole view of the animal head. Extreme care was taken to isolate the camera and the laser path from stray light noise contributions to the speckle image.

3.3.3 Data acquisition and analysis

Since LSCI exploits the spatial statistics properties of laser speckle to obtain the two-dimensional velocity distribution by analyzing the spatial blurring of the raw speckle images, any other blurring effects due to spatial and/or temporal averaging could reduce the speckle and cause errors in estimating the relative changes of blood flow in the experiments. Moreover, the sensitivity to in-plane motion of LSCI is also determined by the speckle size [20]. As we mentioned above, the temporal averaging also imposes the same effect on the speckle, such that a long exposure time compared to the correlation time of the moving scatterer could average out the speckle. A small ROI ($\sim$250 $\times$ 400 pixels) subset of the full FOV (1024 $\times$ 1024 pixels) was selected to record the raw speckle images. At each $PaCO_2$ steady state, 200 speckle images were acquired at 2Hz. Six to seven trials were repeated on an animal in alternating order of hypercapnia and hypocapnia. When changing $PaCO_2$ to a new steady state, the laser beam was blocked by a shutter to avoid unnecessary irradiation to the exposed brain tissue. The first raw speckle image at each level of $PaCO_2$ was used as a baseline to normalize the image set and discarded from later analysis. Each of the remaining 199 images of the normalized image set were used to produce the distribution function of measured speckles and the averaged distribution, which were then compared to the $p(I)$ distribution from Equation 2.

In order to convert the variations of speckle contrast to the intensity variations, a small area on the raw speckle image was chosen in which a sufficient number of speckles were expected. For our settings (25ms exposure time plus 475 ms delay time), it is reasonable to believe that speckles in sequential images are not correlated (as there is significant movement of the scatters in that time) and hence a 3×3 template was used so that spatial resolution was not compromised [36]. The numerical integrations and other data processing in this study were done using MATLAB (The MathWorks, Natick, MA). No digital filters were applied to remove image noise and the final effective spatial resolution was 18 μm/pixel. Only the speckle contrast images within one CO_2 steady state were averaged, which has been proven effective in minimizing drift effects of systemic physiological factors (heart-beat, respiration, blood pressure and spontaneous oscillations of pulsatile blood) [37]. The histogram of the speckle contrast image made by averaging one image dataset was fit with a Maxwellian distribution. Numerically solving τ_c from Eq. 3.9, the relative velocity maps of CBF were calculated in arbitrary units simply by inverting τ_c. In order to compare the velocity changes sequentially measured by both LSCI and LDF measurement in the same area, the CO_2 reactivity index was defined by the following expression in units of %/mmHg:

$$CO_2 \ reactivity \ index \ = \frac{(CBF_{changing \ CO_2} - CBF_{base \ CO_2})/CBF_{base \ CO_2}}{PaCO_{2changing \ CO_2} - PaCO_{2base \ CO_2}} \times 100 \quad [3.11]$$

where $CBF_{changing \ CO_2}$ is the flow or velocity obtained by LDF or LSCI during $PaCO_2$ was changed to a new level; $CBF_{base \ CO_2}$ is the flow or velocity during the baseline level.

3.4 Results

3.4.1 Theoretical results

We first consider the numerical integration of Eq. 3.7, giving $\mu_A(\tau)$ as presented in Fig. 3.1. If the variance of the phase process that gives rise to the speckle pattern increases, $\mu_A(\tau)$ will be narrower. This is usually the case in biological tissues, where the coherent light source can penetrate the tissue and interact with the vasculature below the surface, giving rise to speckle contrast values that are generally quite small ($C < 0.2$). Moreover, when the velocity v increases while other parameters remain fixed ($v\tau$ being distance moved in Eq. 3.7), the value of $\mu_A(\tau)$ will decrease such that the speckle contrast C reduces too. This is why fast flowing vessels appear darkest in LSCI and why even tissue areas perfused with capillaries gets darker with increases in blood flow such as in our hypercapnia experiment (Fig. 3.4). Due to the complicated nature of more realistic forms of $\mu_A(\tau)$ such as we have chosen in Eq. 3.7, the negative exponential function is commonly used to fit its shape and indeed it provides a good approximation to $\mu_A(\tau)$ within the range ($R^2 = 0.93$, shown in Fig. 3.1). However, a Gaussian function is found to almost perfectly match with the calculated $\mu_A(\tau)$ ($R^2 = 0.99$). Particularly at the centre of the autocorrelation function, it is a much better fit to $\mu_A(\tau)$ compared with the negative exponential function. The implications of using both Gaussian and negative exponential functions to replace $\mu_A(\tau)$ in Eq. 3.5 were explored in this study.

As we have discussed in the introduction, previous studies typically assume that $1 - \frac{\tau}{T} \approx 1$, i.e. that $\frac{\tau}{T}$ is small. Therefore the integral window $1 - \frac{\tau}{T}$ in Eq. 3.5 is replaced by a square function that is unity. Fig. 3.2A shows the solution to Eq. 3.9a and 3.9b as a function of the inverse of the velocity of the scatterers. For the case of a negative

exponential function (Eq. 3.9a), we have plotted the speckle contrast C both assuming

$1 - \frac{\tau}{T} \approx 1$ and using the full form $1 - \frac{\tau}{T}$. For a measured speckle value C, it is clear that

different velocities can be inferred from the different curves. Under the conditions that

the full integral window is used $(1 - \frac{\tau}{T})$, there is no difference in the velocity inferred

from using the Gaussian form of $\mu_A(\tau)$ and the negative exponential form of $\mu_A(\tau)$ for

imaging parameters used in most studies. However, if the assumption $1 - \frac{\tau}{T} \approx 1$ is used,

then the negative exponential form of $\mu_A(\tau)$ leads to a significantly different inferred

velocity. Fig. 3.2B shows the percent errors that can arise in the speckle contrast, as a

function of $\frac{\tau_c}{T}$. For the biologically relevant situations currently used for LSCI, the figure

shows that a significant error in C (up to ~41.8%) could be caused when making the

assumption $1 - \frac{\tau}{T} \approx 1$ on the integral window. Similarly, a 10.5% difference could be

introduced by applying different functions to model $\mu_A(\tau)$ even though the same subject

was imaged.
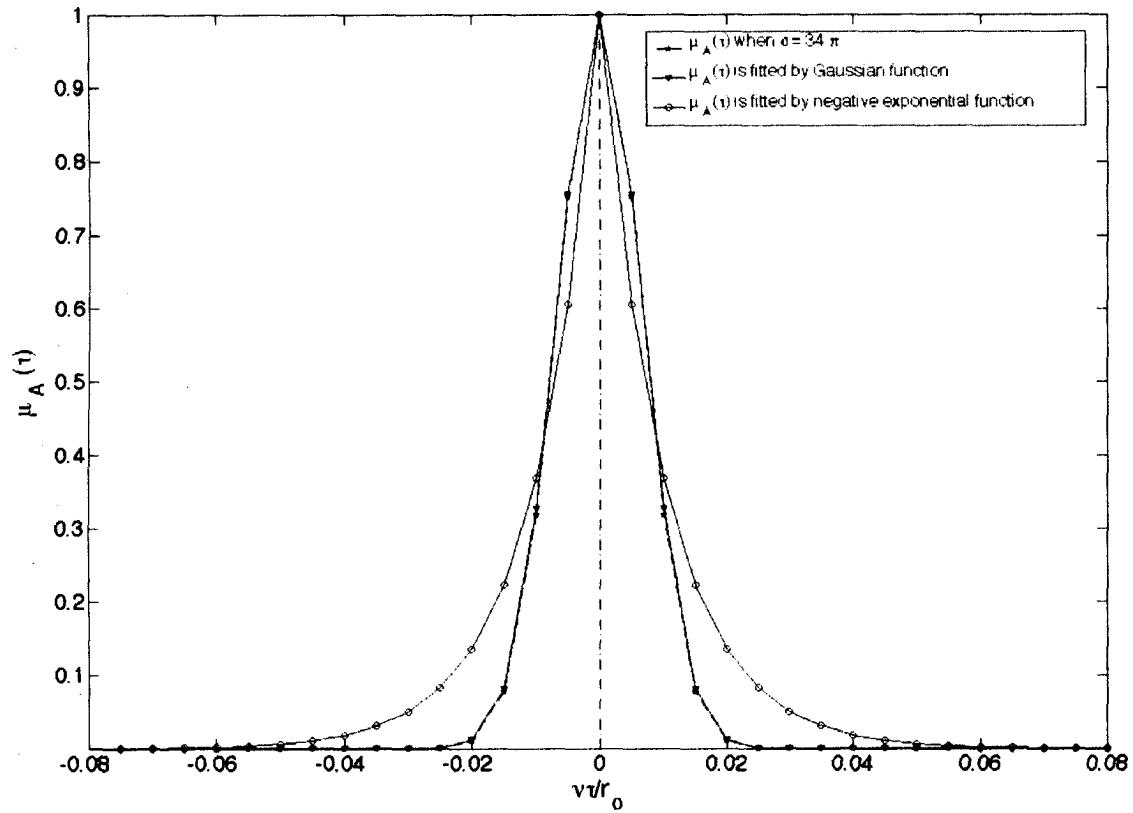
Figure 3.1 Plot of $\mu_A(\tau)$ against $v\tau/r_o$ for Goodman's theoretical model, as well as $\mu_A(\tau)$ fitted by a negative exponential function ($R^2 = 0.93$) and a Gaussian function ($R^2 = 0.99$). Here the value of σ was estimated by Henyey and Greenstein scattering phase function ($\sigma = 34\pi$).
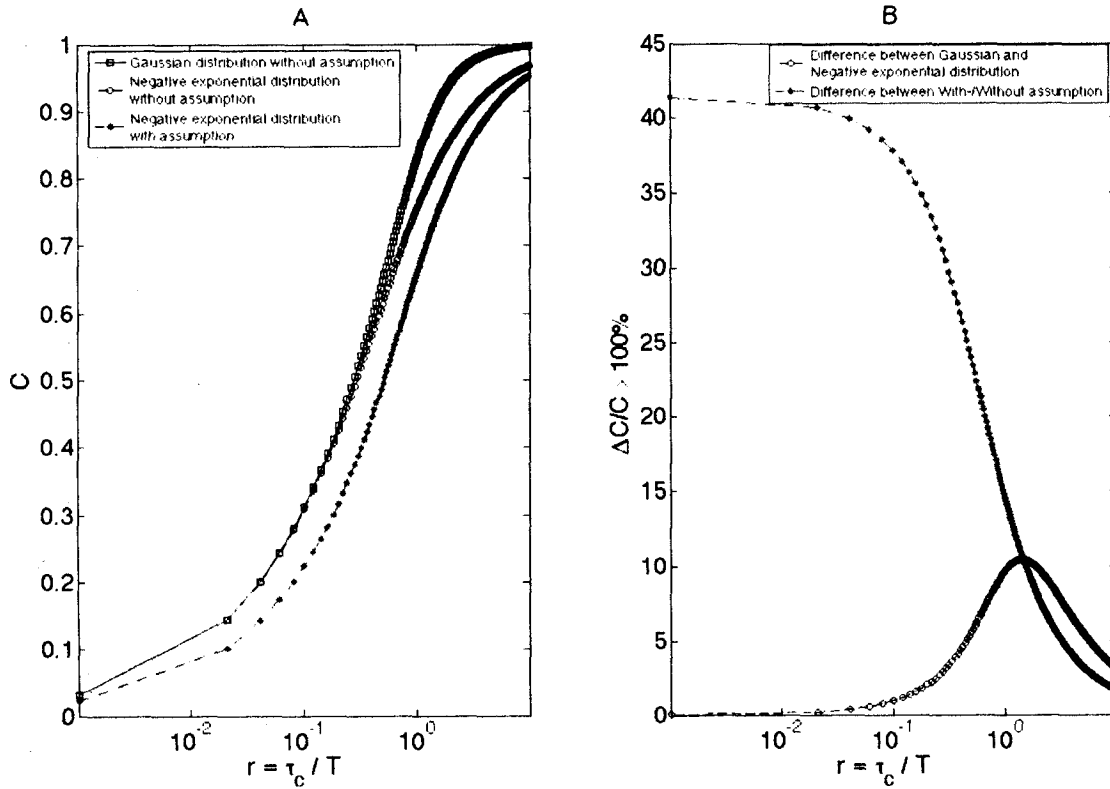
Figure 3.2 The relationship between the speckle contrast and the ratio *r* plotted on a semilogarithmic scale. (A) The theoretical curves of the speckle contrast against *r* were plotted with and without the assumption $T >> \tau_c$ for the negative exponential function, and without the assumption $T >> \tau_c$ for a Gaussian function. (B) The % error in speckle contrast with our without the assumption for a negative exponential and for a comparison of the Gaussian versus negative exponential plotted as a function of *r*.
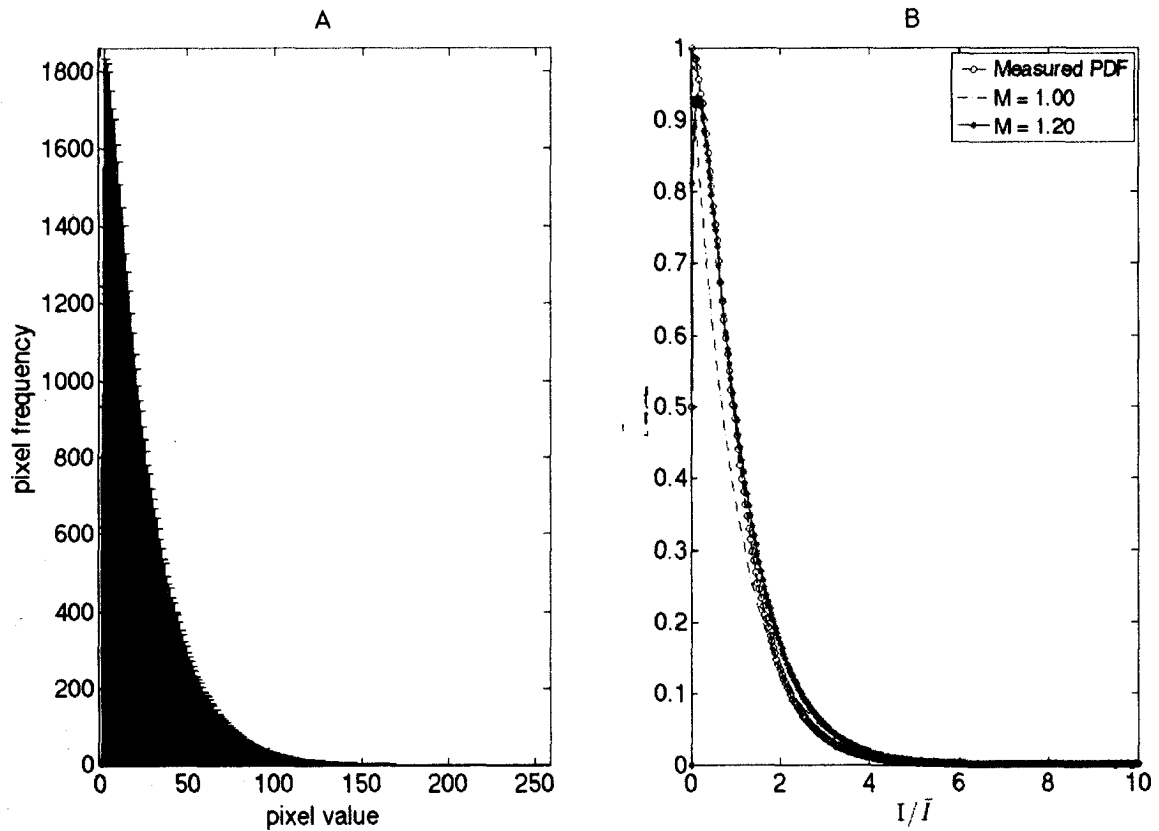
Figure 3.3 (A) Histogram depicting the probability density function of the measured speckle pattern under 32mmHg $PaCO_2$. The error bars associated with this histogram were calculated from one image dataset (the first speckle image was discarded). (B) An illustration of the theoretical Gamma distributions ($M = 1.0$, and $M = 1.2$) and normalized PDF from the left histogram. They both presented a strong correlation with the PDF measured from our experiments, respectively ($R^2 = 0.96, R^2 = 0.98$).

3.4.2 Experimental results

The intensity histogram of the pixel frequency against the intensity values of the raw

speckle images in one data set at 32 mmHg $PaCO_2$ was plotted in Fig. 3.3A. The error

bars were calculated from the 199 images of one trial (the first image was discarded). The

normalized PDF from the measured speckles was computed from this averaged histogram

and was displayed as a semilogarithmic plot in Fig. 3.3B along with $\bar{I}p(I)$ as a function

of $\dfrac{I}{\bar{I}}$ for M = 1.0 and 1.2.

Fig. 3.4 showed one set of speckle contrast images (220×326 pixels) and their

corresponding histograms, in which (A), (B), and (C) are the images made at different

levels of $PaCO_2$: 27, 32, and 50 mmHg, respectively. Noticeable darkening in the tissue

areas occurs as the flow increases between normocapnia and hypercapnia. Additionally, a

clear increase in the diameters of pial blood vessels in hypercapnia occurs (Fig. 3.4C).

The histograms of speckle contrast images corresponding to the three levels of $PaCO_2$ in

the same animal were calculated and fitted with Maxwellian PDFs. On comparison with

these three distributions, a small shoulder that can be clearly observed at 27 mmHg

disappeared as the carbon dioxide pressure increased to 50 mmHg. The pixels that

formed this small plateau originated from the microvascular bed (no large visible vessels).

Additionally, the histogram at high CO_2 level (50 mmHg) was better fit to a Maxwellian

PDF with a smaller value of $\langle v^2 \rangle$, which meant the distribution of the CBF during higher

$PaCO_2$ was more homogeneous than normocapnia. This finding was consistent with

previous conclusions [12; 38; 39].
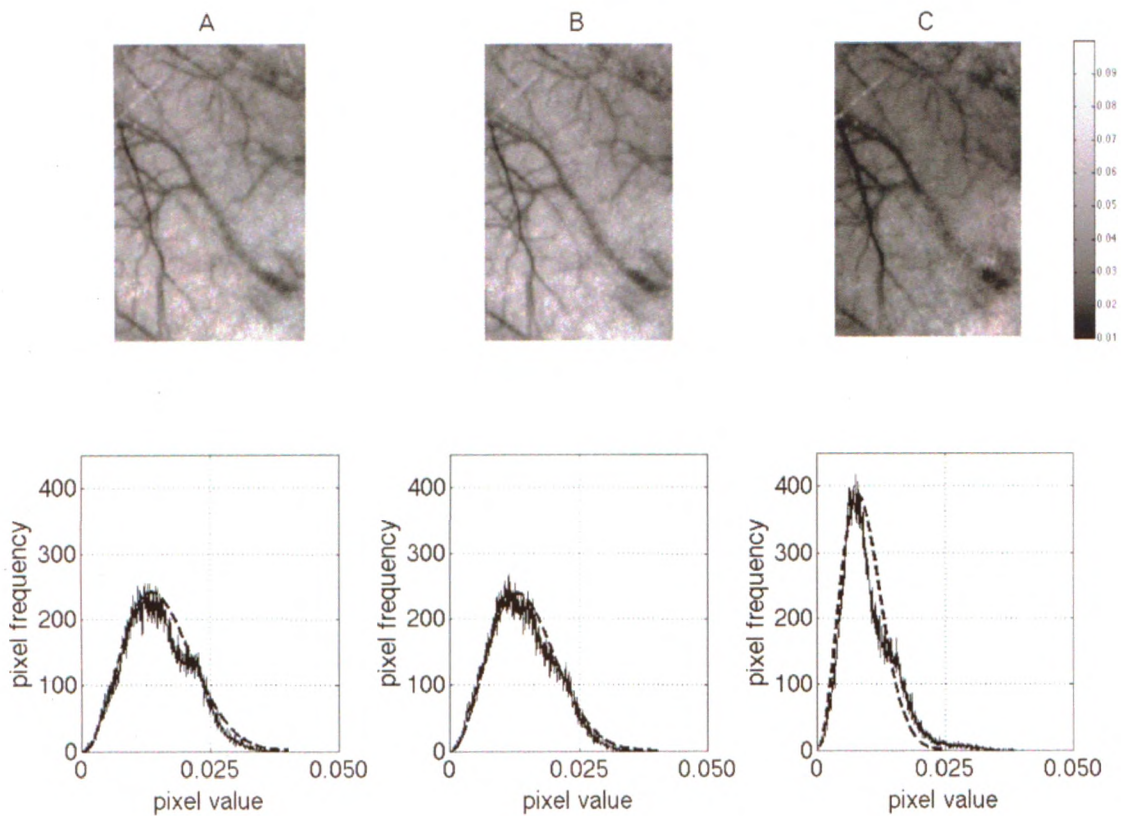
Figure 3.4 Top panel (A-C): example images of CBF responses under different levels of $PaCO_2$ (from left to right, 27, 32, 50mmHg) Bottom panel (A-C): the Maxwellian PDF was scaled to fit the histograms of speckle contrast images at each condition of $PaCO_2$, where the values of $\langle v^2 \rangle$ were 84, 154, 164 respectively from low to high $PaCO_2$. The R^2 values of each fit were 0.97, 0.97, 0.95.
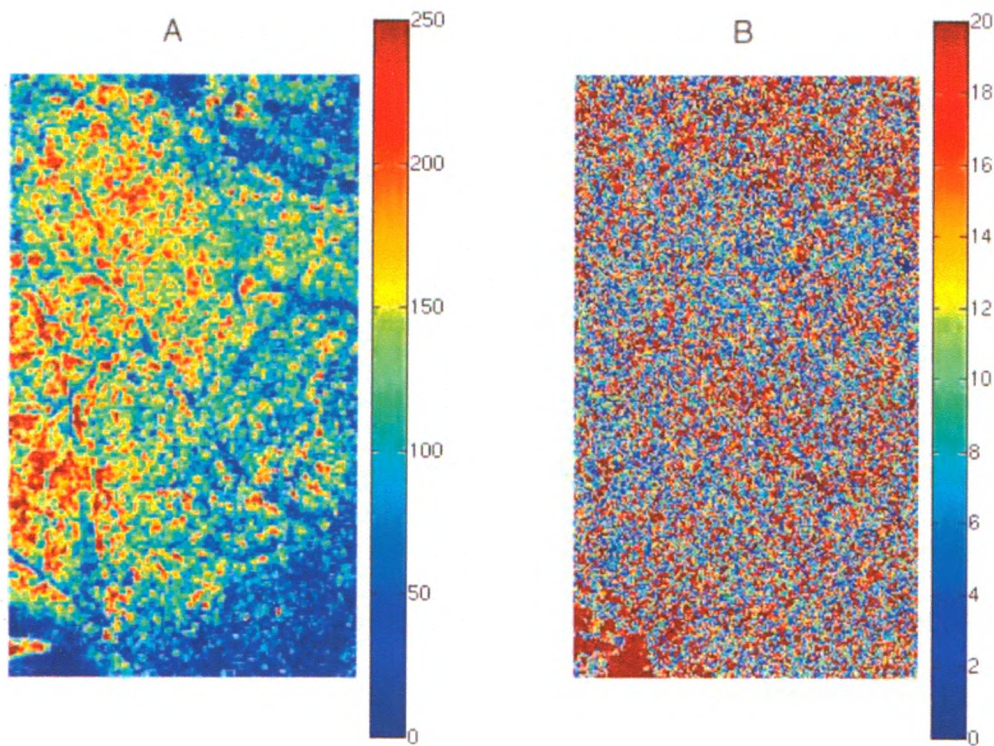
Figure 3.5 Relative velocity maps calculated from the above speckle contrast images were shown as percentage change against baseline (32 mmHg) and displayed as pseudocolor images. (A) Relative velocity increase between 50 mmHg and 32 mmHg. (B) Relative velocity decrease between 27 mmHg and 32 mmHg.

Based on the speckle contrast images, the velocity maps were calculated from Eq. 3.5 in arbitrary units, using the negative exponential form. The ratio of the velocity map at $PaCO_2$ of 50 mm to that at $PaCO_2$ of 32 mm was calculated (Fig. 3.5A). The ratio of the velocity map at $PaCO_2$ of 32 mm to that at $PaCO_2$ of 27 mm was also calculated (Fig. 3.5B). This latter map showed very little change in blood flow. Correcting for an additional factor of 2 that was missing in the form of Eq. 3.6 used by others in the literature [22], our absolute value maps of the velocity are almost twice that of those previously reported in the literature. However the relative changes of blood flow maps between the two $PaCO_2$ levels showed no significant difference to literature values, since a 25 ms exposure time gives a value of the integral window autocorrelation function that approaches 1 in this case (see Eq. 3.5).

The relationship of the CO_2 reactivity index obtained by LSCI and LDF from all the trials was demonstrated as the plot in Fig. 3.6. The results from LDF measurements showed a high correlation (R^2 = 0.92) with LSCI measurements in the same area under the conditions that the $PaCO_2$ was lowered or raised. Under our experimental conditions, the use of either Eq. 3.9a or Eq. 3.9b did not make any difference (<0.1%) to the calculation of the relative velocity, Thus the results from Eq. 3.9a (negative exponential function) were used to compare with that of LDF and are comparable to previous studies [6; 12; 15].
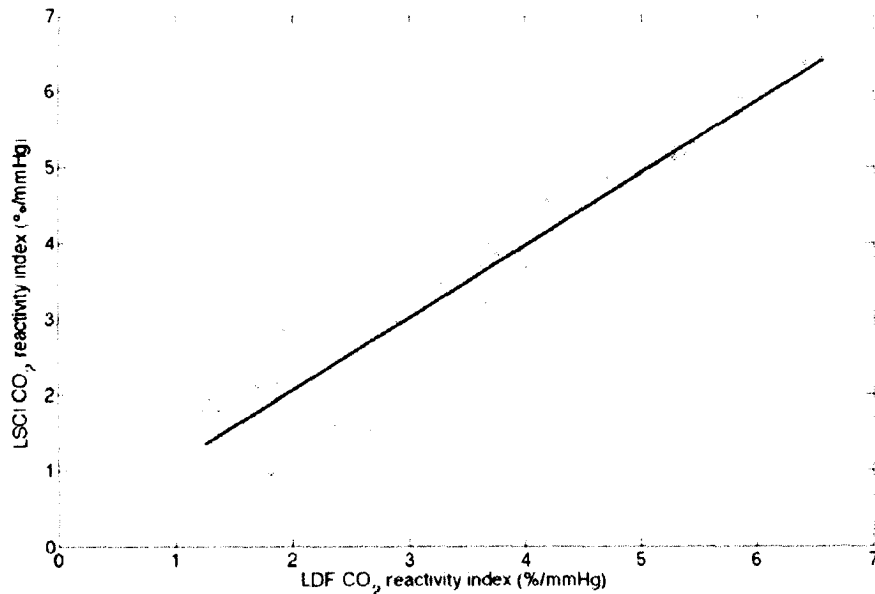
Figure 3.6 The relative changes in blood flow during the stimulation induced by carbon dioxide change measured by LSCI demonstrated strong correlation with the results on LDF on the same area ($R^2 = 0.92$).

3.5 Discussion and Conclusions

Our theoretical analysis and preliminary results from animal experiments demonstrate that the "mistakes" pointed by Bandyopadhyay and his co-workers in the LSCI theory of Fercher and Briers did not produce any significant errors under our experimental conditions using relative flow changes, though these errors are in fact real. However, the original LSCI theory of Goodman contains the correct formulations of the problem that were lost over the years.

It is important to distinguish between the optical spatial resolution of LSCI and the functional spatial resolution for LSCI. It is well known that regional CBF exhibits a significant degree of spatial heterogeneity, not only at the microscopic, but even at the gross anatomical level [33]. Results recently reported by Yuan et al (2005, see Figure 4 in

there) show a higher sensitivity to microvascular blood flow changes at a 20 ms exposure time compared to 5 ms. They attribute this to the sensitivity of the CCD camera, but our analysis shows that shorter exposure times are intrinsically not as sensitive to the microvascular blood velocities because of the underlying physics. Our analysis shows that the choice of exposure time determines the sensitivity to microvascular velocities, and hence the functional spatial resolution. Longer T values give enhanced sensitivity to the microvasculature, which in turn allows mapping of a signal that is more co-localized with neuronal changes in applications such as mapping of cortical function. The velocity of the eythrocyes in the microvasculature corresponds to a τ_c value that is higher than in the pial vessels. To optimize C from the microvasculature, T must therefore be chosen longer than it might be for larger vessels. Thus this tradeoff should be made as appropriate for the experiment being considered. In our experiments, pial vessels were robustly detected. We found that no blood vessel became visible during hypercapnia (>96% trials in this study) that was not visible under normocapnia with the 18 μm spatial resolution used. The contrast between the tissue with its unresolved capillaries and the pial vessels was highest in the 27 mm Hg $PaCO_2$ condition. The tissue significantly darkened at 50 mm Hg $PaCO_2$, but the same pial vessels were still visible. The tissue darkening we observe is more striking than in previous studies, as the 25 ms exposure time increases the sensitivity to the flow in the microcirculation. Thus exposure times of this order would be needed to study the microcirculation signal that is presumably most tightly coupled to the neural activity.

There is no doubt that LSCI is a promising, quantitative, minimally invasive method to achieve *in vivo* high-resolution (submillimeter) visualization of blood flow in exposed

biological tissue. However, there is still considerable room for optimizing this imaging technique. Several issues need to be addressed in the future work.

Firstly, the non-linear relationship between τ_c, T and C based on the simplified model is heuristic here, making it empirically hard to characterize. It depends in a very complicated manner on the experimental object and physiological conditions including the thickness of the thinned skull, all of which would particularly affect the practical range of τ_c that can be observed due to sensitivity, scatter etc.[12]. In future studies, it would be of great interest to define the specific profile of $\mu_A(\tau)$ with respect to the cell speed distribution from *in vivo* experiments so that a more accurate association between the velocity and speckle contrast could be formulated. In principle, it is possible to recover the cell speed distribution from the measured contrast of the speckle pattern if the specific profile of $\mu_A(\tau)$ is known [40]. Thus the velocity of blood flow measured by this technique might be made more quantitative.

Secondly, close inspection of the histograms as shown in Fig. 3.3B reflects some departure of the measured PDF from the ideal negative exponential curve (M = 1) for fully developed speckle. We find that a shape factor of M = 1.2 fits the measured PDF very well ($R^2 = 0.98$). It is possible that fully developed speckle is not a perfect model of coherent light interacting with a brain. Also, various measurement noise sources could contribute to this non-unity value, such as the dark current of camera detector, amplifier noise, background radiation, and depolarization effects. Similar findings have been reported by other researchers [21; 41]. In our setup, the hardware noise from the CCD has been carefully controlled. The system read noise was typically 9 e⁻ r.m.s. and the dark current was less than 0.003 e⁻/p/s when the camera was operated at -70°C. Thus no dark

current correction was applied in our study. The wide dynamic range of CCD camera, averaging strategy and the experiment paradigm applied here helped us to effectively accommodate the contamination from various noise sources. It remains to be seen whether the difference between $M = 1$ and 1.2 is due to the instrumentation or the photon processes in the biological system.

Thirdly, although our results demonstrate for the first time an experimental verification of the Maxwellian distribution used by Bonner and Nossal in their theoretical formulations, this problem deserves more attention. The model we used in this study has been extensively studied since Kety and Schmidt in 1948 where an increased homogeneity of the velocity distribution during hypercapnia was expected [39]. This behavior of CBF responses was indeed embodied exactly as the results from our fitting with Maxwellian distribution (Fig. 3.4). The Maxwellian is broadly considered the best form to describe a stable velocity distribution at an equilibrium state such as the physiological conditions of our animal model. And all the images obtained and shown throughout this study actually characterize the behavior of CBF during the steady state. If the system has a strong anisotropic flow, a Maxwellian distribution may be not appropriate anymore. We have presented a way to experimentally measure the distribution if necessary.

One caution in any animal experimental procedure should be noted here. Stable anesthesia over long durations (many hours) generally requires mechanical ventilation and invasive blood gas sampling, which is relatively difficult to perform with the use of α-chloralose as an anesthetic [16]. Our group recently demonstrated that the rats under isoflurane anesthesia are stable over prolonged and repeated fMRI measurements [34; 42].

But isoflurane does cause a significant reduction in the systemic vascular resistance compared to α-chloralose, with a marked increase in basal CBF [12; 43]. Thus other physiological vital signs have to be continuously monitored throughout this type of experiment. Furthermore, isoflurane depresses cerebrovascular reactivity to CO_2 relative to awake conditions [44] which might explain why the CBF change between 27 and 32 mm Hg was less pronounced (Fig. 3.5B).

LSCI has become an increasingly popular technique to visualize blood flow response to external functional stimulation since Dunn and his colleagues' first application on the rat's brain (2001). It can be anticipated as a complementary method to intrinsic optical imaging techniques that depend on the change in concentrations of intrinsic chromophores due to oxygen metabolism during functional activation [5].

3.6 Reference

1.   Devor A, Ulbert I, Dunn AK, Narayanan SN, Jones SR, Andermann ML, Boas DA, Dale AM. Coupling of the cortical hemodynamic response to cortical and thalamic neuronal activity. Proc Natl Acad Sci U S A, 2005; 102: 3822-3827.

2.   Raichle ME. Behind the scenes of functional brain imaging: a historical and physiological perspective. Proc Natl Acad Sci U S A, 1998; 95: 765-772.

3.   Fox PT, Raichle ME. Focal physiological uncoupling of cerebral blood flow and oxidative metabolism during somatosensory stimulation in human subjects. Proc Natl Acad Sci U S A, 1986; 83: 1140-1144.

4.   Ogawa S, Tank DW, Menon R, Ellermann JM, Kim SG, Merkle H, Ugurbil K. Intrinsic signal changes accompanying sensory stimulation: functional brain mapping with magnetic resonance imaging. Proc Natl Acad Sci U S A, 1992; 89: 5951-5955.

5.   Grinvald A, Lieke E, Frostig RD, Gilbert CD, Wiesel TN. Functional architecture of cortex revealed by optical imaging of intrinsic signals. Nature, 1986; 324: 361-364.

6.   Dunn AK, Bolay H, Moskowitz MA, Boas DA. Dynamic imaging of cerebral blood flow using laser speckle. J Cereb Blood Flow Metab, 2001; 21: 195-201.

7.   Menon RS. Imaging function in the working brain with fMRI. Curr Opin Neurobiol, 2001; 11: 630-636.

8.   Iadecola C. Neurovascular regulation in the normal brain and in Alzheimer's disease. Nat Rev Neurosci, 2004; 5: 347-360.

9.   Kim SG, Ugurbil K. High-resolution functional magnetic resonance imaging of the animal brain. Methods, 2003; 30: 28-41.

10.   Weber B, Burger C, Wyss MT, von Schulthess GK, Scheffold F, Buck A. Optical imaging of the spatiotemporal dynamics of cerebral blood flow and oxidative metabolism in the rat barrel cortex. Eur J Neurosci, 2004; 20: 2664-2670.

11.   Durduran T, Burnett MG, Yu G, Zhou C, Furuya D, Yodh AG, Detre JA, Greenberg JH. Spatiotemporal quantification of cerebral blood flow during functional activation in rat somatosensory cortex using laser-speckle flowmetry. J Cereb Blood Flow Metab, 2004; 24: 518-525.

12.   Ayata C, Dunn AK, Gursoy OY, Huang Z, Boas DA, Moskowitz MA. Laser speckle flowmetry for the study of cerebrovascular physiology in normal and ischemic mouse cortex. J Cereb Blood Flow Metab, 2004; 24: 744-755.

13.   Bolay H, Reuter U, Dunn AK, Huang Z, Boas DA, Moskowitz MA. Intrinsic brain activity triggers trigeminal meningeal afferents in a migraine model. Nat Med, 2002; 8: 136-142.

14.   Choi B, Kang NM, Nelson JS. Laser speckle imaging for monitoring blood flow dynamics in the in vivo rodent dorsal skin fold model. Microvasc Res, 2004; 68: 143-146.

15.   Kharlamov A, Brown BR, Easley KA, Jones SC. Heterogeneous response of cerebral blood flow to hypotension demonstrated by laser speckle imaging flowmetry in rats. Neurosci Lett, 2004; 368: 151-156.

16.   Duong TQ, Kim DS, Ugurbil K, Kim SG. Localized cerebral blood flow response at submillimeter columnar resolution. Proc Natl Acad Sci U S A, 2001; 98: 10904-10909.

17.   Villringer A, Them A, Lindauer U, Einhaupl K, Dirnagl U. Capillary perfusion of the rat brain cortex. An in vivo confocal microscopy study. Circ Res, 1994; 75: 55-62.

18.   Briers JD. Laser Doppler, speckle and related techniques for blood perfusion mapping and imaging. Physiol Meas, 2001; 22: R35-66.

19.   Yuan S, Devor A, Boas DA, Dunn AK. Determination of optimal exposure time for imaging of blood flow changes with laser speckle contrast imaging. Appl Opt, 2005; 44: 1823-1830.

20.   Briers JD. Laser Doppler and time-varying speckle: a reconciliation. J Opt Soc Am, 1996; 13: 345-350.

21.   Briers JD, Richards G, He XW. Capillary blood flow monitoring using laser speckle contrast analysis (LASCA). J Biomed Opt, 1999; 4: 164-175.

22.   Fercher AF, Briers JD. Flow visualization by means of single-exposure speckle photography. Opt Commun, 1981; 37: 326-329.

23.   Bandyopadhyay R, Gitting AS, Suh SS, Dixon PK, Durian DJ. Speckle-visibility spectroscopy: a tool to study time-varying dynamics. Rev Sci Instrum, 2005; 76: 1-11.

24.   Goodman JW. Some effects of target-induced scintillations on optical radar performance. Proc IEEE, 1965; 53: 1688-1700.

25.   Kety SS, Schmidt CF. The Effects of Altered Arterial Tensions of Carbon Dioxide and Oxygen on Cerebral Blood Flow and Cerebral Oxygen Consumption of Normal Young Men. J Clin Invest, 1948; 27: 484-492.

26.   Grubb RL, Jr., Raichle ME, Eichling JO, Ter-Pogossian MM. The effects of changes in $PaCO_2$ on cerebral blood volume, blood flow, and vascular mean transit time. Stroke, 1974; 5: 630-639.

27.   Goodman JW. Statistical properties of laser speckle patterns. In Dainty JC, editor. Laser speckle and related topics. Springer-Verlag: Berlin, 1975: 9-75.

28.   Goodman JW. Statistical optics. Wiley: New York, 1985.

29.   Goodman JW. Speckle phenomena in optics: theory and applications. Greenwood Village: Roberts & company, 2006.

30.   Jakeman E. Photon corrleation. In Cummings HZ, Pike ER, editors. Photon correlation and light beating spectroscopy. Plenum Press: London, 1973: 75-149.

31.   Wang L, Jacques SL, Zheng L. MCML--Monte Carlo modeling of light transport in multi-layered tissues. Comput Methods Programs Biomed, 1995; 47: 131-146.

32.   Bonner R, Nossal R. Model for laser Doppler measurements of blood flow in tissue. Appl Opt, 1981; 20: 2097-2107.

33.   Sokoloff L. Circulation in the central nervous system. In Greger R, Windhorst U, editors. Comprehensive human physiology. Springer-Verlag: Berlin, 1996: 561-578.

34.   Mirsattari SM, Bihari F, Leung LS, Menon RS, Wang Z, Ives JR, Bartha R. Physiological monitoring of small animals during magnetic resonance imaging. J Neurosci Methods, 2005; 144: 207-213.

35.   Petoukhova AL, Cleven E, de Mul FF, Steenbergen W. Suppression of dynamic laser speckle signals in multimode fibers of various lengths. Appl Opt, 2004; 43: 2059-2065.

36.   Volker AC, Zakharov P, Weber B, Buck F, Scheffold F. Laser speckle imaging with active noise reduction scheme. Opt Exp, 2005; 13: 9782-9787.

37.   Detre JA, Ances BM, Takahashi K, Greenberg JH. Signal averaged laser Doppler measurements of activation-flow coupling in the rat forepaw somatosensory cortex. Brain Res, 1998; 796: 91-98.

38.   Vogel J, Abounader R, Schrock H, Zeller K, Duelli R, Kuschinsky W. Parallel changes of blood flow and heterogeneity of capillary plasma perfusion in rat brains during hypocapnia. Am J Physiol, 1996; 270: H1441-1445.

39.   Hudetz AG, Biswal BB, Feher G, Kampine JP. Effects of hypoxia and hypercapnia on capillary flow velocity in the rat cerebral cortex. Microvasc Res, 1997; 54: 35-42.

40.   Stern MD. In vivo evaluation of microcirculation by coherent light scattering. Nature, 1975; 254: 56-58.

41.   Webster MA, Webb KJ, Weiner AM, Xu J, Cao H. Temporal response of a random medium from speckle intensity frequency correlations. J Opt Soc Am A Opt Image Sci Vis, 2003; 20: 2057-2070.

42.   Mirsattari SM, Wang Z, Ives JR, Bihari F, Leung LS, Bartha R, Menon RS. Linear aspects of transformation from interictal epileptic discharges to BOLD fMRI signals in an animal model of occipital epilepsy. Neuroimage, 2006; 30: 1133-1148.

43.   Matta BF, Heath KJ, Tipping K, Summors AC. Direct cerebral vasodilatory effects of sevoflurane and isoflurane. Anesthesiology, 1999; 91: 677-680.

44.   Sicard K, Shen Q, Brevard ME, Sullivan R, Ferris CF, King JA, Duong TQ. Regional cerebral blood flow and BOLD responses in conscious and anesthetized rats under basal and hypercapnic conditions: implications for functional MRI studies. J Cereb Blood Flow Metab, 2003; 23: 472-481.

Chapter 4   Conclusion

With the systems designed and developed in this thesis, we now have significant potential to explore more sophisticated questions in visual neuroscience and neurophysiology. This chapter provides a brief summary of the thesis and potential benefits of the present study. Possible interesting directions for exploiting these tools and techniques are also mentioned.

4.1 Thesis Summary

Functional maps in neuroimaging rely on identifying areas that respond selectively to various aspects of cognitive and sensorimotor processing. Underlying the colourful images, the most prevalent model for deriving activation maps in imaging neuroscience is the general linear model although some recent studies point to a nonlinear direction [1]. But one has to keep in mind that the ultimate interest of the modeling analysis is situated in the context of probing the intrinsic nature of the biological system we observed, other than simply for the system identification. Regardless of where the modeling will eventually lead, this modeling analysis has to be rooted in a biologically plausible basis.

Therefore, the hemodynamic response function in this context is expected to accurately reflect functional and/or physiological integration of its closely coupled neuronal processes, more than a coarse approximation of sluggish temporal latency from neuron to vessels commonly assumed in fMRI studies. This is the key point what I endeavored to highlight in Chapter 2.

Exploring the temporal characteristics of hemodynamic responses was carried out in the striate cortex of primates by varying the duration of stimulus presentation. Building up a working model in alert behaving macaques would allow us a bridge to get closer to those fMRI studies mostly done on human subjects. Hence the neural and hemodynamics data were acquired on our awake monkeys when they visually perceived a simple radial checkerboard with different durations (0.5, 1.0, 2.0, 3.0s). A novel two-component (transient-sustained) linear convolution model was proposed to fit the neural and hemodynamics data in time domain. A rapid biphasic HRF and a slower monophasic HRF were identified to associate the transient and sustained components of the power spectral density of the LFP with the CBF response, respectively. The unmasking of two CBF responses was accomplished using a stable deconvolution of the observed CBF and a measure of the neuronal activities that relates to neural energy consumption (integral of the power of LFPs). Beyond the implications for fMRI analysis and BOLD biophysical models, our findings suggest that there exist two distinctly tuned CBF regulatory mechanisms in primate cortex. One appears to support the high energy demands typical of transient neuronal response and the other the more modest demands of sustained neuronal response. The results from our analysis strongly imply that different neural ensembles may concurrently involve in responses to one single visual stimulus, each of

which might impose distinct physiological influences on the cerebrovascualture network. Further experimental evidence by directly visualizing spatial-specific hemodynamic regulation with the aid of more advanced flow imaging technologies is needed to support this finding.

To disentangle the complex spatial integration of hemodynamic responses over a given location, I adopted and improved an "old" optical imaging technique – LSCI that holds a distinct promise because of its high spatial (~ 20 μm) and temporal resolution (~ 25 ms). Through a complete theoretical analysis, an important strategy was set for LSCI technique so as to assess the brain microcirculation with higher specificity to the capillary blood flow. Meanwhile, two overlooked assumptions in the widely cited LSCI paper of Fercher and Briers were re-examined in my theoretical analysis and supported by our own experimental evidence. Our primary results from anaesthetized animals suggest that LSCI is a promising, quantitative, minimally invasive method to achieve *in-vivo* high-resolution visualization of blood flow in the exposed biological tissue. And this system can be conveniently integrated with other optical imaging techniques such as intrinsic optical imaging [2] and in-vivo fluorescence imaging [3].

4.2 Future Work

Without a doubt the fMRI technique will remain as an important tool to map the working mechanisms of the brain in both healthy and diseased states. With the exponential growth in fMRI research, an important challenge is to bridge the gap between noninvasive human studies examining changes in BOLD contrast and the extensive body of research obtained through electrophysiological recordings in animals, typically

examining the spiking activity of individual neurons [4; 5]. It is interesting to measure the BOLD signals by using the same paradigm in the thesis and compare with the current results. Several groups have demonstrated the feasibility of applying fMRI in alert monkeys in 1.5 T scanner [6-8], but a number of technical impediments for high-field (usually a smaller bore available) application have to be tackled off before we set about pursuing exciting neuroscience questions [9]. The following discussion of future work is based on the electrophysiological system and optical imaging system of awake monkeys that have been established in the course of this project.

4.2.1 Neurophysiology

There are several veins of study we can envisage in light of the work done in Chapter 2. The first emerging question is to measure the hemodynamic responses that could correspond to the transient or sustained components (TR-SR) recorded in our experiments and in many other studies [10; 11]. It will help us to understand the underlying neural basis of our two-component model. First, this would provide more insight into the cellular mechanism of the transient-sustained neural response pattern. It is not clear yet if the TR-SR pattern in our experiments is due to rapid neural adaptation (i.e. the same neurons simply modulating their response, or different spatial or other classes of neurons) [12; 13]. Neural adaptation is well known in the early stage of visual system [11; 14; 15], even though its neural basis still is an area of active research [16-18]. Second it would be interesting to see the interaction between this pattern and hemodynamic regulation since the blood supply is supposed to proportionally fuel the neural processes. One major functional benefit of such adaptation behavior proposed by previous theoretical analysis proposed is to save the energy cost [15; 19; 20]. Furthermore, it has an important implication

for the rapid event-related design fMRI experiments [13; 21]. It has been revealed that repetition of an identical stimulus produces an immediate decrease in the neuronal response and associated fMRI signal, so called fMRI adaptation [13]. This paradigm hypothesizes that two neuron population participate in two levels of modulation driven by the same stimulus feature and results in different hemodynamic responses before and after adaptation [18]. This is coherent with our observation from behaving monkeys that initial hemodynamic response in V1 (non-adapted level) is different from the one at sustained level (adapted level). Noticeably, a growing number of recent fMRI studies using rapid event-related design have taken advantage of this hemodynamic difference to study neuronal selectivity or perceived shape or face representation in the higher-level visual areas [22-24]. The second question is the relationship between spiking activity of individual neurons, high frequency LFP (particularly gamma LFP) and blood flow or BOLD signals. One recent study on auditory cortex of human epilepsy patients suggested the interneuronal correlation could be a better measure of neuronal ensemble activity which is responsible for BOLD signals [25]. If this is the case, the degree of coupling between these three measures may be dependent on the specific architecture of the brain circuitry. Thus it would be interesting to see what happens in the primary visual cortex where oscillatory activity is more pronounced and easily recorded [26-29]. The third question is to differentiate bottom-up and top-down modulation in V1. Higher visual areas might send feedback signals to confirm the reliability of the information they receive from V1, or to modulate V1 activity on the basis of top-down knowledge [30]. In view of the existing time delay and amplitudes of two components, this explanation seems to fit well into our data analysis too. To safely incorporate or exclude this possibility, it certainly demands

more careful experimental design and intensive training on the monkeys to perform top-down modulation explicitly-involved cognitive tasks.

4.2.2 Optical imaging of awake monkeys

Further experiments are also feasible by using optical methods to monitor the physiological parameters during external stimulation. The most obvious is to perform LSCI experiments on awake monkeys. Using CBF-based MRI technique, Duong and his coworkers suggested that pure CBF change at tissue level without large-vessel contribution could be localized enough to resolve the columnar structure in striate cortex of cats [31]. Until now, there are no other reports yet to confirm their finding because high spatial and temporal resolution of CBF measurement is required to detect this event [32]. At this point, LSCI technique seems a good candidate to practise this task. Combined with intrinsic optical imaging technique, the relationship between CBF and CBV can be dynamically investigated during visual stimulation as well [33]. It could be helpful to settle the recently rising debates as to whether CBV is localized at the columnar level or not [34-37].

With regard to the topography of the striate cortex, it is of obvious interest to pinpoint CBF behaviors down to capillary network level in three dimensional space. It could shed insightful light on the underlying mechanism of neurovascular regulation in the columned and layered brain structures. With the awake monkey platform already initiated, it will not be terribly challenging to apply in-vivo fibered confocal technique (we already have the hardware system in the lab). If possible, the multi-photon imaging technique is also an option to address this issue on the awake monkey model [3;38;39]. Ultimately, the goal of

the development of these powerful technologies is to understand the hierarchy of CBF control by different elements that can alter vascular dilation and constriction [40-42]. We will then know which levels are fundamentally important in inducing the changes in flow that underlie BOLD contrast.

4.3 References

1.   Friston KJ. Imaging neuroscience: principles or maps? Proc Natl Acad Sci U S A, 1998; 95: 796-802.

2.   Grinvald A, Lieke E, Frostig RD, Gilbert CD, Wiesel TN. Functional architecture of cortex revealed by optical imaging of intrinsic signals. Nature, 1986; 324: 361-364.

3.   Misgeld T, Kerschensteiner M. In vivo imaging of the diseased nervous system. Nat Rev Neurosci, 2006; 7: 449-463.

4.   Logothetis NK. MR imaging in the non-human primate: studies of function and of dynamic connectivity. Curr Opin Neurobiol, 2003; 13: 630-642.

5.   Orban GA. Functional MRI in the awake monkey: the missing link. J Cogn Neurosci, 2002; 14: 965-969.

6.   Dubowitz DJ, Chen DY, Atkinson DJ, Grieve KL, Gillikin B, Bradley WG, Jr., Andersen RA. Functional magnetic resonance imaging in macaque cortex. Neuroreport, 1998; 9: 2213-2218.

7.   Stefanacci L, Reber P, Costanza J, Wong E, Buxton R, Zola S, Squire L, Albright T. fMRI of monkey visual cortex. Neuron, 1998; 20: 1051-1057.

8.   Vanduffel W, Fize D, Mandeville JB, Nelissen K, Van Hecke P, Rosen BR, Tootell RB, Orban GA. Visual motion processing investigated using contrast agent-enhanced fMRI in awake behaving monkeys. Neuron, 2001; 32: 565-577.

9.   Keliris GA, Shmuel A, Ku SP, Pfeuffer J, Oeltermann A, Steudel T, Logothetis NK. Robust controlled functional MRI in alert monkeys at high magnetic field: effects of jaw and body movements. Neuroimage, 2007; 36: 550-570.

10.   Niessing J, Ebisch B, Schmidt KE, Niessing M, Singer W, Galuske RA. Hemodynamic signals correlate tightly with synchronized gamma oscillations. Science, 2005; 309: 948-951.

11.   Logothetis NK, Pauls J, Augath M, Trinath T, Oeltermann A. Neurophysiological investigation of the basis of the fMRI signal. Nature, 2001; 412: 150-157.

12.   Muller JR, Metha AB, Krauskopf J, Lennie P. Rapid adaptation in visual cortex to the structure of images. Science, 1999; 285: 1405-1408.

13.   Dale AM, Buckner RL. Selective averaging of rapidly presented indvidual trials using fMRI. Hum Brain Mapp, 1997; 5: 329-340.

14.   Logothetis NK. The neural basis of the blood-oxygen-level-dependent functional magnetic resonance imaging signal. Philos Trans R Soc Lond B Biol Sci, 2002; 357: 1003-1037.

15.   Kohn A. Visual adaptation: physiology, mechanisms, and functional benefits. J Neurophysiol, 2007; 97: 3155-3164.

16.   Sawamura H, Orban GA, Vogels R. Selectivity of neuronal adaptation does not match response selectivity: a single-cell study of the FMRI adaptation paradigm. Neuron, 2006; 49: 307-318.

17.   Solomon SG, Peirce JW, Dhruv NT, Lennie P. Profound contrast adaptation early in the visual pathway. Neuron, 2004; 42: 155-162.

18.   Grill-Spector K, Henson R, Martin A. Repetition and the brain: neural models of stimulus-specific effects. Trends Cogn Sci, 2006; 10: 14-23.

19.   Laughlin SB, Sejnowski TJ. Communication in neuronal networks. Science, 2003; 301: 1870-1874.

20.   Lennie P. The cost of cortical computation. Curr Biol, 2003; 13: 493-497.

21.   Rosen BR, Buckner RL, Dale AM. Event-related functional MRI: past, present, and future. Proc Natl Acad Sci U S A, 1998; 95: 773-780.

22.   Grill-Spector K, Kushnir T, Edelman S, Avidan G, Itzchak Y, Malach R. Differential processing of objects under various viewing conditions in the human lateral occipital complex. Neuron, 1999; 24: 187-203.

23.   Kourtzi Z, Kanwisher N. Representation of perceived object shape by the human lateral occipital complex. Science, 2001; 293: 1506-1509.

24.   Xu Y, Turk-Browne NB, Chun MM. Dissociating task performance from fMRI repetition attenuation in ventral visual cortex. J Neurosci, 2007; 27: 5981-5985.

25.   Nir Y, Fisch L, Mukamel R, Gelbard-Sagiv H, Arieli A, Fried I, Malach R. Coupling between neuronal firing rate, gamma LFP, and BOLD fMRI is related to interneuronal correlations. Curr Biol, 2007; 17: 1275-1285.

26.   Bartos M, Vida I, Jonas P. Synaptic mechanisms of synchronized gamma oscillations in inhibitory interneuron networks. Nat Rev Neurosci, 2007; 8: 45-56.

27.   Gray CM, Singer W. Stimulus-specific neuronal oscillations in orientation columns of cat visual cortex. Proc Natl Acad Sci U S A, 1989; 86: 1698-1702.

28.   Engel AK, Fries P, Singer W. Dynamic predictions: oscillations and synchrony in top-down processing. Nat Rev Neurosci, 2001; 2: 704-716.

29.   Engel AK, Moll CK, Fried I, Ojemann GA. Invasive recordings from the human brain: clinical insights and beyond. Nat Rev Neurosci, 2005; 6: 35-47.

30.   Tong F. Primary visual cortex and visual awareness. Nat Rev Neurosci, 2003; 4: 219-229.

31.   Duong TQ, Kim DS, Ugurbil K, Kim SG. Localized cerebral blood flow response at submillimeter columnar resolution. Proc Natl Acad Sci U S A, 2001; 98: 10904-10909.

32.   Pfeuffer J, Merkle H, Beyerlein M, Steudel T, Logothetis NK. Anatomical and functional MR imaging in the macaque monkey using a vertical large-bore 7 Tesla setup. Magn Reson Imaging, 2004; 22: 1343-1359.

33.   Kong Y, Zheng Y, Johnston D, Martindale J, Jones M, Billings S, Mayhew J. A model of the dynamic relationship between blood flow and volume changes during brain activation. J Cereb Blood Flow Metab, 2004; 24: 1382-1392.

34.   Sheth SA, Nemoto M, Guiou M, Walker M, Pouratian N, Hageman N, Toga AW. Columnar specificity of microvascular oxygenation and volume responses: implications for functional brain mapping. J Neurosci, 2004; 24: 634-641.

35.   Vanzetta I, Slovin H, Omer DB, Grinvald A. Columnar resolution of blood volume and oximetry functional maps in the behaving monkey; implications for FMRI. Neuron, 2004; 42: 843-854.

36.   Fukuda M, Moon CH, Wang P, Kim SG. Mapping iso-orientation columns by contrast agent-enhanced functional magnetic resonance imaging: reproducibility, specificity, and evaluation by optical imaging of intrinsic signal. J Neurosci, 2006; 26: 11821-11832.

37.   Smirnakis SM, Schmid MC, Weber B, Tolias AS, Augath M, Logothetis NK. Spatial specificity of BOLD versus cerebral blood volume fMRI for mapping cortical organization. J Cereb Blood Flow Metab, 2008; in press.

38.   Chaigneau E, Tiret P, Lecoq J, Ducros M, Knopfel T, Charpak S. The relationship between blood flow and neuronal activity in the rodent olfactory bulb. J Neurosci, 2007; 27: 6452-6460.

39.   Schaffer CB, Friedman B, Nishimura N, Schroeder LF, Tsai PS, Ebner FF, Lyden PD, Kleinfeld D. Two-photon imaging of cortical surface microvessels reveals a robust redistribution in blood flow after vascular occlusion. PLoS Biol, 2006; 4: e22.

40.   Metea MR, Newman EA. Glial cells dilate and constrict blood vessels: a mechanism of neurovascular coupling. J Neurosci, 2006; 26: 2862-2870.

41.   Mulligan SJ, MacVicar BA. Calcium transients in astrocyte endfeet cause cerebrovascular constrictions. Nature, 2004; 431: 195-199.

42.   Zonta M, Angulo MC, Gobbo S, Rosengarten B, Hossmann KA, Pozzan T, Carmignoto G. Neuron-to-astrocyte signaling is central to the dynamic control of brain microcirculation. Nat Neurosci, 2003; 6: 43-50.

Appendix A   Copyright Releases

(A.1) Copyright Waiver for Material Contained Within Chapter 1

**ELSEVIER LIMITED LICENSE
TERMS AND CONDITIONS**

May 23, 2008

This is a License Agreement between Zheng Wang ("You") and Elsevier Limited ("Elsevier Limited"). The license consists of your order details, the terms and conditions provided by Elsevier Limited, and the payment terms and conditions.

Supplier	Elsevier Limited
	The Boulevard,Langford Lane
	Kidlington,Oxford,OX5 1GB,UK
Registered Company Number	1982084
Customer name	Zheng Wang
Customer address	Center for Functional and Metabolic Mapping
	London, ON N6A5K8
License Number	1954830026266
License date	May 23, 2008
Licensed content publisher	Elsevier Limited
Licensed content publication	Brain Research Bulletin
Licensed content title	Cortical blood vessels of the human brain
Licensed content author	H. M. Duvernoy, S. Delon and J. L. Vannson
Licensed content date	November 1981
Volume number	7
Issue number	5
Pages	61
Type of Use	Thesis / Dissertation
Portion	Figures/table/illustration/abstracts
Portion Quantity	2
Format	Electronic
You are an author of the Elsevier article	No
Are you translating?	No
Purchase order number	
Expected publication date	Aug 2008
Elsevier VAT number	GB 494 6272 12
Permissions price	0.00 USD

(A.2) Copyright Waiver for Material Contained Within Chapter 3

NATURE PUBLISHING GROUP LICENSE
TERMS AND CONDITIONS

Feb 18, 2008

This is a License Agreement between Zheng Wang ("You") and Nature Publishing Group ("Nature Publishing Group"). The license consists of your order details, the terms and conditions provided by Nature Publishing Group, and the payment terms and conditions.

License Number	1892080616305
License date	Feb 18, 2008
Licensed content publisher	Nature Publishing Group
Licensed content publication	Journal of Cerebral Blood Flow
Licensed content title	Theoretical and experimental optimization of laser speckle contrast imaging for high specificity to brain microcirculation
Licensed content author	Zheng Wang, Sarah Hughes, Sudath Dayasundara, Ravi S Menon
Volume number	27
Issue number	2
Pages	258-269
Year of publication	2007
Portion used	Full paper
Requestor type	Student
Type of Use	Thesis / Dissertation
PO Number	
Total	0.00 USD
Terms and Conditions	

Terms and Conditions for Permissions

Nature Publishing Group hereby grants you a non-exclusive license to reproduce this material for this purpose, and for no other use, subject to the conditions below:

1. NPG warrants that it has, to the best of its knowledge, the rights to license reuse of this material. However, you should ensure that the material you are requesting is original to Nature Publishing Group and does not carry the copyright of another entity (as credited in the published version). If the credit line on any part of the material you have requested indicates that it was reprinted or adapted by NPG with permission from another source, then you should also seek permission from that source to reuse the material.

2. Permission granted free of charge for material in print is also usually granted

for any electronic version of that work, provided that the material is incidental to the work as a whole and that the electronic version is essentially equivalent to, or substitutes for, the print version. Where print permission has been granted for a fee, separate permission must be obtained for any additional, electronic re-use (unless, as in the case of a full paper, this has already been accounted for during your initial request in the calculation of a print run). NB: In all cases, web-based use of full-text articles must be authorized separately through the 'Use on a Web Site' option when requesting permission.

3. Permission granted for a first edition does not apply to second and subsequent editions and for editions in other languages (except for signatories to the STM Permissions Guidelines, or where the first edition permission was granted for free).

4. Nature Publishing Group's permission must be acknowledged next to the figure, table or abstract in print. In electronic form, this acknowledgement must be visible at the same time as the figure/table/abstract, and must be hyperlinked to the journal's homepage.

5. The credit line should read:

Reprinted by permission from Macmillan Publishers Ltd: [JOURNAL NAME] (reference citation), copyright (year of publication)

For AOP papers, the credit line should read:

Reprinted by permission from Macmillan Publishers Ltd: [JOURNAL NAME], advance online publication, day month year (doi: 10.1038/sj.[JOURNAL ACRONYM].XXXXX)

6. Adaptations of single figures do not require NPG approval. However, the adaptation should be credited as follows:

Adapted by permission from Macmillan Publishers Ltd: [JOURNAL NAME] (reference citation), copyright (year of publication)

7. Translations of 401 words up to a whole article require NPG approval. Please visit http://www.macmillanmedicalcommunications.com for more information. Translations of up to a 400 words do not require NPG approval. The translation should be credited as follows:

Translated by permission from Macmillan Publishers Ltd: [JOURNAL NAME] (reference citation), copyright (year of publication).

We are certain that all parties will benefit from this agreement and wish you the best in the use of this material. Thank you.

v1.1

Appendix B   Ethics Approval

(B.1) Ethnic Approval for Experiments Conducted Within Chapter 2

Western

This is the Original Approval of this protocol
A full protocol submission will be required in 2007

Dear Dr. Menon:

Your "Application to Use Animals for Research or Teaching" entitled:

"Biophysical Basis of fMRI"
Funding Agency– CIHR - Grant #MOP-64399   NSERC - Grant #261701-03
   NIH - Grant #1RO1EB002739

has been approved by the University Council on Animal Care. This approval expires September 30, 2004, but the protocol number will remain the same until a full protocol submission is required. The number for this project is 2003-058-09 .

1. This number must be indicated when ordering animals for this project.
2. Animals for other projects may not be ordered under this number.
3. If no number appears please contact this office when grant approval is received.
   If the application for funding is not successful and you wish to proceed with the project, request that an internal scientific peer review be performed by the Animal Use Subcommittee office.
4. Purchases of animals other than through this system must be cleared through the Vivarium Services office. Health certificates will be required.

ANIMALS APPROVED			FOR 1 YR.	PAIN LEVEL
Primates ·	Macaca mulatta 2-8 yrs/4-12 kg	F/M ·	4	D

STANDARD OPERATING PROCEDURES
Procedures in this protocol should be carried out according to the following SOPs. Please contact the Animal Use Subcommittee office (661-2111 ext. 86770) in case of difficulties or if you require copies. SOP's are also available at http://www.uwo.ca/animal

310-02:	Holding Period Post-Admission
320-02:	Euthanasia
322-02:	Criteria for Early Euthanasia/Mammals/Non Rodents
334-03:	Post-operative/Post-Anaesthetic Care - Level Four
360-03:	Blood Collection/Volumes/Multiple Species

REQUIREMENTS/COMMENTS
Please ensure that individual(s) performing procedures on live animals, as described in this protocol, are familiar with the contents of this document.

c.c. Approved Protocol   -   R. Menon, S. Hughes, W. Lagerwerf
     Approval Letter   ┌ S. Hughes, W. Lagerwerf

University of Council on Animal Care • The University of Western Ontario
Animal Use Subcommittee • Health Sciences Centre • London Ontario • N6A 5C1 • Canada

(B.2) Ethnic Approval for Experiments Conducted Within Chapter 3

Western

November 28, 2003

This is the Original Approval of this protocol
*A Full Protocol submission will be required in
2007*

Dear Dr. Bartha:

Your "Application to Use Animals for Research or Teaching" entitled:

"New Metabolic Imaging Approaches to Assess Brain Tissue Viability"
Funding Agency-- Robarts Research Institute

has been approved by the University Council on Animal Care. This approval is valid until November 30, 2004.
The number for this project remains as 2003-103-11.

1. This number must be indicated when ordering animals for this project.
2. Animals for other projects may not be ordered under this number.
3. If no number appears please contact this office when grant approval is received.
   If the application for funding is not successful and you wish to proceed with the project, request that an internal scientific peer review be performed by the Animal Use Subcommittee office.
4. Purchases of animals other than through this system must be cleared through the ACVS office. Health certificates will be required.

ANIMALS APPROVED   **FOR 1 YR.   PAIN LEVEL - B**

Rats   -   Sprague Dawley 250 gm   M -   81

STANDARD OPERATING PROCEDURES
Procedures in this protocol should be carried out according to the following SOPs. Please contact the Animal Use Subcommittee office (661-2111 ext. 6770) in case of difficulties or if you require copies.
SOP's are also available at http://www.uwo.ca/animal/acvs
    # 310 Holding Period Post Admission
    # 320 Euthanasia
    # 321 Early Euthanasia/Rodents

REQUIREMENTS/COMMENTS
Please ensure that individual(s) performing procedures on live animals, as described in this protocol, are familiar with the contents of this document.

c.c. Approved Protocol -   R. Bartha, S. Hughes, W. Lagerwerf
      Approval Letter   -   S. Hughes, W. Lagerwerf